Modelling slow sand filtration and solving interface problems with the Transfer Path Method

Manriquez, Jaime

2026

Document Version:
Publisher's PDF, also known as Version of record

Modelling slow sand filtration and solving interface problems with the Transfer Path Method

Modelling slow sand filtration and solving interface problems with the Transfer Path Method

Jaime Manríquez Rodríguez

LUND
UNIVERSITY

Thesis for the degree of Doctor of Philosophy in Engineering

To be publicly defended, with due permission of the Faculty of Engineering at Lund University, on Friday the 22nd of May 2026 at 09:00 in lecture hall MH:Riesz at the Centre for Mathematical Sciences, Märkesbacken 4, Lund.

Faculty opponent
Associate Prof. Vanja Nikolić

Organization	Document name
LUND UNIVERSITY Centre for Mathematical Sciences Box 118 SE–221 00 LUND Sweden	**DOCTORAL DISSERTATION** Date of disputation 2026-05-22 Sponsoring organization
Author(s) Jaime Manríquez Rodríguez	

Title and subtitle

Modelling slow sand filtration and solving interface problems with the Transfer Path Method

Abstract

Filtration through porous media is the oldest form of drinking water treatment and, to this day, constitutes a focal point of research in water engineering. Mathematical models of filtration are often used in conjunction with supplementary models of concurrent phenomena. For instance, both fluid flow inside and outside the filtering medium are of interest, and models of both flow through porous media and of free fluid flow become necessary for comprehensive modelling. Such supplementary models are often coupled together in some manner, leading to extended systems of equations and possibly complicated geometries. Additionally, at low filtration rates, biochemical reactions taking place during the treatment process gain relevance and need to be taken into account to have a complete description of the filtration process.

In this work, we are concerned with water filtration from two angles: first, we are interested in comprehensive modelling of *Slow Sand Filters* (SSFs), in which the action of the ecological community settled in the biofilm growing in the medium constitutes the main filtration mechanism; and second, we are interested in the coupling of free flow with flow through porous media with mismatching discretizing geometries at the interface utilizing the so-called *Transfer Path Method* (TPM) in the context of interface problems in fluid mechanics.

The doctoral thesis is consequently divided into two parts. The first part contains a new one-dimensional model framework of SSFs which involves the water flow in the entire filter, consisting of the sand bed and the supernatant water sitting atop it, along with the evolution of microorganisms therein. A positivity-preserving numerical method under certain assumptions is presented together with a documentation of the software developed for simulations. A two-dimensional model for the supernatant water region is also included; a derivation is presented as well as an invariant-region-preserving numerical method for the entire convection-reaction-Cahn–Hilliard system.

In the second part, the TPM is applied to coupled problems in fluid mechanics in the context of dissimilar meshes, that is, geometrical discretizations of two independent domains separated by an interface in which the resulting triangulations may present mismatches in the form of gaps or overlaps. The hybridizable discontinuous Galerkin method is used to discretize the corresponding systems of partial differential equations and present results for Stokes flow, Stokes/Darcy coupling and fluid-structure interaction.

Key words

Biofilm growth, Hybridizable Discontinuous Galerkin, Modelling, Multi-phase flow, Nonlinear convection-diffusion-reaction PDEs, Slow sand filtration, Transfer Path Method, Unfitted methods

Classification system and/or index terms (if any)

Supplementary bibliographical information	Language
	English
ISSN and key title 1404-0034 Doctoral Theses in Mathematical Sciences 2026:5	ISBN 978-91-8104-913-8 (print) 978-91-8104-914-5 (pdf)
Recipient's notes / Number of pages xviii+288	Price
Security classification	

Modelling slow sand filtration and solving interface problems with the Transfer Path Method

Jaime Manríquez Rodríguez

LUND
UNIVERSITY

Main supervisor
Associate Prof. Stefan Diehl

Co-supervisors
Prof. Manuel Solano, Prof. Eskil Hansen

Funding information: The thesis work was mainly funded by the Swedish Research Council (Vetenskapsrådet 2019-04601) and partly funded by the Swedish Research Council for Sustainable Development (FORMAS 2019-00432, 2022-01900). Financial support was also received from the Walter Gyllenberg Foundation from the Royal Physiographic Society of Lund.

Published by:

Centre for Mathematical Sciences
Faculty of Engineering
Lund University
Lund 2026

ISBN: 978-91-8104-913-8 (print)
ISBN: 978-91-8104-914-5 (pdf)

LUTFTM-1003-2026
Doctoral thesis in mathematical sciences 2026:5
ISSN: 1403-0034

Printed in Sweden by Media-Tryck, Lund University, Lund 2026

Dedicated to my parents, Jaime and Doris,
without whom I would have never been born

Contents

List of publications

This thesis is based on the following publications and working manuscripts, referred to by their Roman numerals. Author order is alphabetical in all works save for Paper II.

Part I: Modelling slow sand filtration

I **A convection-diffusion-reaction system with discontinuous flux modelling biofilm growth in slow sand filters**
S. Diehl, **J. Manríquez**, C. J. Paul and T. Rosenqvist
Applied Mathematical Modelling, Volume 137, Part A, 2025, 115675
doi.org/10.1016/j.apm.2024.115675

II **Simulating biofilm growth and pathogen removal in slow sand filters under variable environmental conditions using a multi-phase continuum model**
J. Manríquez, T. Rosenqvist, S. Chan, C. J. Paul and S. Diehl
Submitted

III **An invariant-region-preserving scheme for a convection-reaction-Cahn–Hilliard multiphase model of biofilm growth in slow sand filters**
J. Careaga, S. Diehl and **J. Manríquez**
Computers & Mathematics with Applications, Volume 201, 2026, pp. 146–170
doi.org/10.1016/j.camwa.2025.10.012

Part II: Solving interface problems with the Transfer Path Method

IV **A dissimilar non-matching HDG discretization for Stokes flows**
J. Manríquez, N. C. Nguyen and M. Solano
Computer Methods in Applied Mechanics and Engineering, Volume 399, 2022, 115292
doi.org/10.1016/j.cma.2022.115292

V **A hybridizable discontinuous Galerkin method for Stokes/Darcy coupling on dissimilar meshes**
I. Bermúdez, **J. Manríquez** and M. Solano
IMA Journal of Numerical Analysis, Volume 46, Issue 1, 2026, pp. 336–371
doi.org/10.1093/imanum/drae109

Acknowledgements

I want to start these acknowledgements by thanking the most important actor that allowed this thesis to happen, God almighty, whose grace and mercy enlighten my path. As a close second, I would like to thank my advisor, Stefan Diehl. This position completely changed my life and I definitely could not have done this without your help, both in scientific writing and furniture moving. I am forever grateful for all the kindness and patience that you have shown me during these five years. I have learned a lot working with you and hope to someday achieve even a fraction of the hard work and dedication you put into your research and teaching. Gracias por tanto y perdón por lo poco.

I would like to thank Vanja Nikolić for accepting the role of opponent, and to Sara Zahedi, Peter Hansbo and Christian Engström for accepting to act as committee. I also wish to extend my thanks to my co-supervisor Eskil Hansen, as well as my apologies for all the nonsense, both administrative and mathematical, that I have thrown his way throughout the years.

Thank you to my co-authors, Catherine, Sandy and Tage, for their helpful explanations, patience and fruitful interdisciplinary collaboration; Julio, for extending me a helping hand when I most needed it and being an excellent example of what an applied mathematician should be; and finally Isaac, for his dilligence and ever-friendly attitude, which has made working with him an absolute joy.

I want to especially thank my co-supervisor Manuel Solano for all of the support he has given me during the last 10 years. For all of the discussions, programming sessions, help outside of office hours—regardless of whether we are in the same timezone—and nice casual conversations. I think back on my second year of university when, after the last class of Numerical Analaysis I, you introduced me to the concept of Hilbert spaces and the Finite Element Method, and how that single event (along with a gentle push from your then-student, Patrick Vega) changed the trajectory of my life forever, leading me to quit Mechanical Engineering and pursue a degree in Mathematics. In that regard, I also want to use this opportunity to thank my teachers in Chile who contributed to my formation in numerical analysis: Rommel Bustinza, Raimund Bürger, Gabriel Gatica (duly cited), and Rodolfo Rodríguez.

I also want to thank all the Junior Fellows at the *Interfaces and Unfitted Discretization Methods* program at the Mittag-Leffler institute for a number of very interesting mathematical discussions and karaoke sessions. Particular thanks go to Beatrice, Gioana, Max, Nanna, Shivangi and Simon.

The rest of these acknowledgements become difficult to write for me as my studies have bled onto everything else that has happened in my life for the last 5 years. Rather, it would be

more accurate to say that all of my life since has sprouted from the wound of coming here to start this PhD. The memories, both in and out of office, ranging from terrible to amazing, have intertwined themselves so tightly that the resulting braided fabric is as smooth as a silk sheet. Therefore, I will make my best effort to uphold something that resembles thoughtful writing and perhaps even meaning, but to the more Jaime-attuned people it may very well be a fraction of my skull plastered on the page. However, I assure to everyone reading that, one way or another, everyone here has been absolutely essential to the writing of this thesis.

To my colleagues at the Centre of Mathematical Sciences, for all the conversations, trivia and laughs we have shared during *fika*. Thank you to Abolfazl, Alejandro, Alex, Anna, Erik, Erik (the other one), Erik (the other other one), Filip, Frej, Georgios, Ivar, Jennie, Joakim, Jonathan, Jorge, Oskar, Rahul, Sofia, Stefano, Tom and Wilhelm. To my former office mate Donglin and office neighbour Mats. To the soulful performers Mårten and Måns. To my peers in numerical analysis whom I admire, Emil, Jimmy, Marvin and Niklas.

Shout out to all the wonderful staff at Café Ariman (past and present): Adam, Alex, Clara, Emil, Hedvig, Kyle, Malva, Nora, Josie, Julie, Sixten, the *Staropramen* glasses, and Winnie. Without all of you, I would be so much thinner and have so much more money. I guess I will be content with all the warm welcomes and wonderful chats that we had.

To all my friends from outside the world of mathematics (who do, in fact, exist). Thanks to Albert, for all those fridays that became a much needed constant in uncertain times. You have more than made up in calories by forcing me to start running. Thanks to my former neighbour Maria for always being so thoughtful and willing to help. Thanks to Ophelia for all the help with the Swedish language and culture. Thanks to Benjamin, Johan and Max, for introducing me to the wonderful world of Magic: The Gathering and that dudes, very much in fact, rock.

And to those who have become my strongest supports. The people who I always end up running to when I need help. My most sincere thanks to Felix Augustsson, Magnus Fries, Olof Rubin, Valentina Schüller and Teodor Åberg. Without you, none of these words would be here at all. I have learned *so* much from each and every one of you that these margins are ill-fitted bounds to ever contain the breadth your contributions. I think.

I wish want to thank my family for their continuous support and love, particularly my parents, my sister and my little niece, even if the latter decided to steal my thunder by coming to this world right as I made my triumphant exit out of my parents' house.

Lastly, I want to thank Sara (my girlfriend). To you, I dedicate the most honest words that I have ever written: *I always thought that I would never know if all of this was worth it. If anything I did here mattered at all. If all the sadness and nights waking up screaming were for any good. But then I met you, and all my doubts disappeared. Coming here was the single best decision I made and I would do it ten thousand times over if only to be able to meet you again.*

Popular summary in English

In order to conceptualize and describe real-world processes in natural sciences and engineering, we use *models*—substitute representations of these processes. Models can then be used to communicate and conduct research. Examples of models include reconstructions at smaller scales, like model trains, or larger scales, like molecular models. By developing a *mathematical model* of a process, by "translating it into mathematics", we are able to compactly communicate how the process behaves even where it is difficult or impossible to make measurements in reality.

A mathematical model consists of a list of simplifying assumptions together with a set of mathematical objects that describe the physical laws governing the process. In our context, this amounts to a choice of a one-, two- or three-dimensional space, together with a set of equations. Solutions to these equations can then give both qualitative and quantitative predictions of the process.

It is often the case that model equations cannot be solved by pen-and-paper methods, requiring the use of computational approximations, obtained by so-called *numerical methods*. The use of numerical methods, "feeding the equation into the computer" so-to-speak, involves both computational and theoretical aspects. For instance, it is important to implement efficient methods as well as to know in advance if they will produce reliable outputs. An key concept is then that of *convergence*, which roughly measures if (and in what measure) increase in computational effort yields increase in accuracy.

These two practices—"translating into mathematics" (mathematical modelling) and "feeding equations into the computer" (numerical methods)—fall under the larger umbrella of *applied mathematics*. In this thesis, we make contributions to the field of applied mathematics with two main projects. In the first, we develop new mathematical models of slow sand filters for drinking water treatment. In the second, we apply a method to deal with interface problems between domains with non-matching discretizations, that is, domains for which their computational geometries are not properly aligned.

In the first project, we developed a unified framework for a one-dimensional model of slow sand filters along with a corresponding numerical method. The results agree with the existing literature, indicating that the unified framework manages to generalize existing models. A two-dimensional model of a filter subregion is also studied with positive results.

In the second project, we successfully applied the so-called *Transfer Path Method* for remote coupling of misaligned computational geometries with gaps. Optimal convergence was shown at the theoretical level for a fluid-fluid and a fluid-sand problem under certain assumptions on the gaps, and numerical results validate these findings. Additionally, numerical experiments indicate optimal convergence for a fluid-structure problem.

Populärvetenskaplig sammanfattning på svenska

För att konceptualisera och beskriva verkliga processer inom naturvetenskap och teknik, använder vi *modeller*, vilka är representanter för processerna. Modellerna används för att kommunicera och bedriva forskning. Exempel är rekonstruktioner i mindre skala, som *modell*tåg, eller större skala, som molekylmodeller i kemi. Genom att utveckla en *matematisk modell* av en process, ”översätta den till matematik”, kan vi i ett kompakt format beskriva hur processen beter sig även där det i verkligheten är svårt eller omöjligt att göra mätningar.

En matematisk modell består av en lista med förenklande antaganden tillsammans med en uppsättning matematiska objekt som beskriver de viktigaste egenskaperna hos processen. I vårt sammanhang motsvarar detta att välja en, två eller tre rumsdimensioner tillsammans med en uppsättning ekvationer. Lösningar till ekvationerna kan ge både kvalitativa och kvantitativa förutsägelser av processens beteende.

Oftast kan ekvationerna i en modell inte lösas med papper och penna, utan kräver beräkningsapproximationer, som fås med så kallade *numeriska metoder*. Användningen av numeriska metoder, så att säga att ”mata in ekvationen i datorn”, involverar både beräkningsmässiga och teoretiska verktyg. Det är till exempel viktigt att både implementera effektiva metoder och att i förväg veta om de kommer att producera tillförlitliga resultat. En särskild egenskap av intresse är *konvergens*, som ungefärligt anger om (och på vilket sätt) mer resurskrävande beräkningar leder till en ökad noggrannhet av resultaten.

Dessa två metoder — att ”översätta till matematik” (matematisk modellering) och att ”mata in ekvationer i datorn” (numeriska metoder) — faller under det större paraplyet *tillämpad matematik*. I denna avhandling bidrar vi till området tillämpad matematik med två huvudprojekt. I det första utvecklar vi nya matematiska modeller av långsamfilter för dricksvattenrening. I det andra tillämpar vi en metod för att hantera gränssnittsproblem mellan olika domäner med icke-matchande diskretiseringar, det vill säga beräkningsgeometrier för närliggande domäner som inte passar ihop.

I det första projektet utvecklade vi ett enhetligt ramverk för en endimensionell modell av långsamfilter tillsammans med en motsvarande numerisk metod. Resultaten överensstämmer med den befintliga litteraturen, vilket indikerar att det enhetliga ramverket lyckas generalisera befintliga modeller. En tvådimensionell modell av ett specifikt område i filtret studeras också med positiva resultat.

I det andra projektet tillämpade vi framgångsrikt den så kallade *Transfer Path-metoden* för fjärrkoppling mellan två olika beräkningsgeometrier som inte passar ihop. Optimal konvergens visades på teoretisk nivå för ett vätske-vätske- och ett vätske-sandproblem under vissa antaganden, och numeriska resultat validerar dessa fynd. Dessutom indikerar numeriska experiment optimal konvergens för ett vätske-strukturproblem.

Resumen de divulgación científica en español

Para conceptualizar y describir procesos relevantes para las ciencias naturales y la ingeniería, utilizamos *modelos* como representaciones sustitutas, facilitando a su vez la comunicación y la investigación. Ejemplos de modelos incluyen maquetas a pequeña escala, como un tren modelo, o a mayor escala, como un modelo molecular. Al diseñar un modelo matemático de un proceso, al "traducirlo a las matemáticas", podemos comunicar de forma concisa cómo se comporta el proceso incluso donde es difícil o incluso imposible tomar mediciones.

Un modelo matemático consta de una lista de supuestos y objetos matemáticos que describen las leyes de la física que gobernan el proceso. En nuestro contexto, esto implica escoger un espacio en una, dos o tres dimensionas, además de un conjunto de ecuaciones apropiadas. Resolver estas ecuaciones puede entonces entregar predicciones tanto cualitativas como cuantitativas del proceso de interés.

Por lo general, las ecuaciones de un modelo no pueden resolverse a lápiz y papel, requiriendo el uso de aproximaciones computacionales, obtenidas mediante *métodos numéricos*. El uso de métodos numéricos, el "ingresar una ecuación a la computadora", involucra aspectos computacionales y teóricos. Por ejemplo, es importante implementar métodos eficientes desde un punto de vista computacional, así como también determinar de antemano si estos producirán resultados fiables, lo cual requiere el uso de herramientas teóricas. Una concepto clave entonces es la *convergencia*, la cual indica, grosso modo, si un aumento en recursos computacionales resultará efectivamente en un aumento de la precisión y en qué medida.

Estas dos prácticas—la de "traducir a las matemáticas" (modelamiento matemático) y la de "introducir ecuaciones en la computadora" (métodos numéricos)—caen dentro del campo de las matemáticas aplicadas. En esta tesis, contribuimos a las matemáticas aplicadas con dos proyectos. En el primero, desarrollamos nuevos modelos matemáticos de filtros de arena lentos para el tratamiento de agua potable. En el segundo, aplicamos un método para abordar problemas de interfaz entre dominios con discretizaciones no coincidentes, es decir, dominios cuyas geometrías computacionales no están correctamente alineadas.

En el primer proyecto, desarrollamos un marco unificado para un modelo unidimensional de filtros de arena lentos junto con un método numérico. Los resultados concuerdan con la literatura existente, indicando que el marco unificado generaliza modelos existentes. También se estudió un modelo parcial en dos dimensiones, obteniendo resultados positivos.

En el segundo proyecto, aplicamos con éxito el *método de los caminos de transferencia* para el acoplamiento remoto de geometrías desalineadas. Se demostró convergencia óptima a nivel teórico para un problema fluido-fluido y uno fluido-arena bajo suposiciones de la geometría, con resultados numéricos validando estos hallazgos. Además, experimentos numéricos indican convergencia óptima para un problema de interacción fluido-estructura.

Terminology

Term	Explanation	Reference
SSF	Slow Sand Filter	Chapter 3
TPM	Transfer Path Method	Chapter 6
PDE	Partial Differential Equation	
HDG	Hybridizable Discontinuous Galerkin	Section 5.3.4
1D, 2D, 3D	One, two and three spatial dimensions	
Cahn–Hilliard equation	Fourth-order non-linear PDE which models phase separation	Section 2.4
CFL condition	Courant–Friedrichs–Lewy condition, describing the limitations on time steps that produce stable numerical simulations	Chapter 6
Coupled problem	Multi-physics problem where two or more domains or governing equations are to be solved together	Chapter 3
Hybridization	The introduction of an additional variable in a numerical method, usually a trace multiplier, that weakly enforces continuities	Chapter 5
Monolithic coupling	Solving the equations of a coupled problem simultaneously in contrast to non-monolithic coupling in which the equations are solved in a serial or iterative manner.	Chapter 6
Schmutzdecke	The top layer of biomass in a slow sand filter	Chapter 3
Unfitted method	A numerical method in which the non-conformity of the geometry is taken into account and remediated by bespoke means. In contrast, a fitted method is such that the discrete geometry is constructed to approximate with the exact one	Chapter 6

Chapter 1

Introduction

Motivation

The development of mathematical models using partial differential equations (PDEs) and of numerical methods to approximate their solutions are cornerstones of applied mathematics. Research questions often arise from the interest in answering problems coming from natural sciences. This includes the development of new models and methods for studying phenomena of interest. Questions can also come from the need to further develop existing methods, answering technical questions concerning implementation or mathematical aspects. We say, then, that approaches to research questions in applied mathematics can be *problem-* or *method-oriented*, by which we mean to distinguish whether the focus is on a concrete physical process or on some mathematical aspect. The latter is of great importance as the development of robust numerical methods helps scientists from all fields. Moreover, the importance of dissemination of models and numerical methods back to the natural sciences community must not be underestimated, as interdisciplinary work constantly proves to be a main driving force in technological development. For that reason, we can argue that the role of an applied mathematician is to solve problems, develop theory and methods, as well as to communicate these findings.

In water science, more specifically in drinking water treatment, there exist a variety of problems which require closer mathematical treatment. For example, in the development of new technologies, it is important to develop mathematical models along with fast and reliable algorithms for simulations, but this is also true for existing treatment methods which may not be completely understood because of the multi-physics complexity involved. Such is the case for slow sand filtration, a process that is at least two centuries old, but for which there exist few comprehensive mathematical models that include the entire filter

modelling biomass growth and pathogen removal. Another complexity involved in water treatment problems, although not unique to this field, is curved geometries, which poses a challenge as most traditional numerical methods utilize piecewise straight geometries. Since many of these problems involve multiple physical, chemical or biological components, the geometries may involve interactions along a curved surface, as is the case in fluid-structure problems or multiphase flows. It is then of interest to develop robust algorithms that can deal with curved geometries at low computational cost.

In this thesis, we take both a *problem-oriented* approach, deriving a model of slow sand filtration for drinking water treatment, and and a *method-oriented* approach, extending the current analysis of an unfitted finite element method to interface problems in fluid mechanics. In the first, we are concered with answering research questions posed by microbiologists and water scientists, such as how to correctly model *slow sand filters* (SSFs) in the times of climate change, deriving a method from first principles and developing an appropriate numerical method for simulations. In the second, we study a coupling method for numerically solving coupled PDEs where the geometrical discretizations are not conforming to the coupling interface, the so-called *Transfer Path Method* (TPM) [Cockburn and Solano, 2012, Sánchez-Vizuet et al., 2020], and extend its analysis to applications in coupled problems in fluid mechanics. Ultimately, our goal is to extend the mathematical theory and computational methods in both of these fronts and to effectively communicate them to the broader community, microbiologists and mathematicians.

Research questions

The work in this thesis is based on the following questions:

(i) How does one derive a mathematical model of SSFs from first principles with the least amount of heuristic assumptions baked in?

(ii) How does one obtain a reliable simulation algorithm from the mathematical model of SSFs?

(iii) What is a coherent model for pathogen removal in an SSF?

(iv) How do we apply the TPM to transmission problems involving pressure?

(v) How do we apply the TPM to coupled problems involving a physical interface?

(vi) What are the requirements on the unfitted meshes and the gaps between them in order to maintain optimal convergence of the HDG method when using the TPM?

Outline of the thesis

This thesis work is based on two main projects: partly the development of a mathematical model and numerical method for biofilm growth and pathogen removal in slow sand filters, and partly the development and implementation of a numerical method for coupled problems with smooth interfaces. Consequently, the thesis is divided into two parts corresponding to each project. Chapter 2 contains prerequisite concepts relevant to both parts.

In each part, an introduction to the topic is given (Chapters 3 and 5), followed by an overview of the contributions made in this thesis (Chapters 4 and 6). Conclusions are presented including a summary of the results of each paper and how they relate to the research questions as well as an outlook with future research directions. Additionally, repositories for the software developed in both projects are indicated in the appendix.

Chapter 2

Preliminaries

2.1 Continuum mechanics

In this thesis, we will model material bodies assuming that they are continua, that is, infinitely divisible objects such that the space they occupy can be identified with subsets of the Euclidean space $\mathbb{R}^n$ ($n = 1, 2, 3$) and for which physical properties can be described by real functions with this Euclidean subset as domain. The actual physical objects are properly represented by subsets in $\mathbb{R}^3$, but by taking transversal and cross-sectional averages, we will work with bodies in $\mathbb{R}^2$ and $\mathbb{R}^1$, respectively. For instance, in Papers I and II, we work with a flowing mixture as a one-dimensional body, representing its change in the flwo direction by taking its average in the perpendicular plane, whereas in Paper III, we treat the mixture as a 2D body. In Papers IV and V, although not explicitly stated, we can assume that the 2D representations correspond to either transversal averages or constrained flows to a plane, and the corresponding bodies are, for example, a solid structure $\Omega_S \subset \mathbb{R}^2$ and a surrounding fluid $\Omega_F \subset \mathbb{R}^2$.

In this section, we present a very brief overview of the relevant concepts that will be used in the rest of the thesis, and for a more in-depth presentation, we refer the reader to [Gonzalez and Stuart, 2008]. To fix notation, we say that a quantity is a *scalar* if it belongs to $\mathbb{R}$, a *vector* if it belongs to $\mathbb{R}^n$ and a *tensor* if it belongs to $\mathbb{R}^n \otimes (\mathbb{R}^n)^*$, which we will always interpret as an element of $\mathbb{R}^{n\times n}$.

Assuming a fixed reference frame with *spatial* coordinates $\boldsymbol{x} \in \mathbb{R}^n$ and time $t \in \mathbb{R}$, we consider an arbitrary body $\mathcal{M} := \mathcal{M}(t) \subset \mathbb{R}^n$ with initial reference configuration $\mathcal{M}(0)$; see Figure 2.1. Material properties of this body can be expressed by volumetric density fields, which can be scalar-, vector- or tensor-valued. Unless otherwise specified, when we refer to a *field*, we mean any scalar-, vector- or tensor-valued function with the units of

physical quantity per volume.

The initial configuration defines a reference frame with coordinates $\boldsymbol{X}$, which are known as the *material coordinates*. Fields described in terms of these coordinates are said to be in *Lagrangian* (or material) description and can be thought of as fields that "follow" the particle $\boldsymbol{X}$ in its trajectory through time and space. This is in contrast to *Eulerian* (or spatial) descriptions which state a field in terms of a fixed reference frame (in our case, the $\boldsymbol{x}$-coordinates).

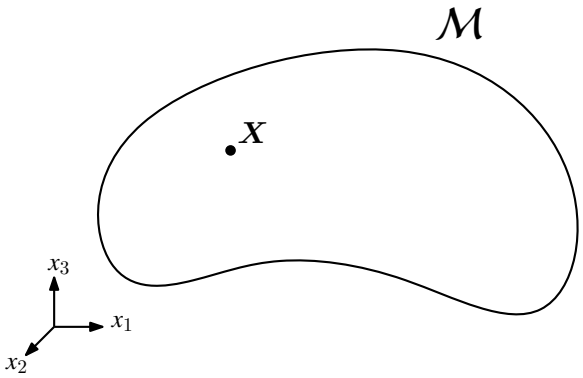

Figure 2.1: Potato-shaped body $\mathcal{M}$, possibly the most famous body in all of continuum mechanics.

We say that a fixed particle $\boldsymbol{X}_0 \in \mathcal{M}(0)$ with position $\boldsymbol{x}_0 = \boldsymbol{x}_0(t)$ moves in space at time t with velocity vector $\boldsymbol{V}_0 = \dot{\boldsymbol{x}}_0(t) \in \mathbb{R}^n$. By collecting all velocity vectors for all particles in the initial configuration of $\mathcal{M}$, we can construct the velocity field $\boldsymbol{V} = \boldsymbol{V}(\boldsymbol{X}, t)$. We assume that it is possible to describe the fixed-frame position $\boldsymbol{x} = \boldsymbol{\varphi}(\boldsymbol{X}, t)$ of all particles $\boldsymbol{X} \in \mathcal{M}(0)$ in terms of our reference frame and that this map $\boldsymbol{\varphi}(\cdot, t)$ is invertible for all times t so we may write $\boldsymbol{X} = \boldsymbol{X}(\boldsymbol{x}, t) = \boldsymbol{\varphi}^{-1}(\boldsymbol{x}, t)$. This lets us restate our *Lagrangian* velocity field $\boldsymbol{V}$ as an *Eulerian* velocity field $\boldsymbol{v} = \boldsymbol{v}(\boldsymbol{x}, t) = \boldsymbol{V}(\boldsymbol{X}(\boldsymbol{x}, t), t)$; see Example 2.1.1.

Example 2.1.1. *Consider a body with initial configuration $\mathcal{M} = [0, L] \subset \mathbb{R}$ for which its Lagrangian velocity field is given by*

$$V(X, t) = -V_0 \frac{X}{L}, \qquad X \in \mathcal{M},$$

see Figure 2.2. If we follow any single particle X, we can find its spatial position at x time $t \in \left[0, \frac{L}{V_0}\right)$ by

$$x = X - V_0 \frac{X}{L} t \quad \Longleftrightarrow \quad X = \frac{L}{L - V_0 t} x$$

from which it follows that

$$v(x, t) = -V_0 \frac{x}{L - V_0 t}.$$

If we were to "hitch a ride" atop a fixed particle X, then we will see that we are travelling at constant speed for all $t \in \left[0, \frac{L}{V_0}\right)$*; if we decide to stand a fixed point x, we will perceive things passing us by faster and faster as time goes on.*

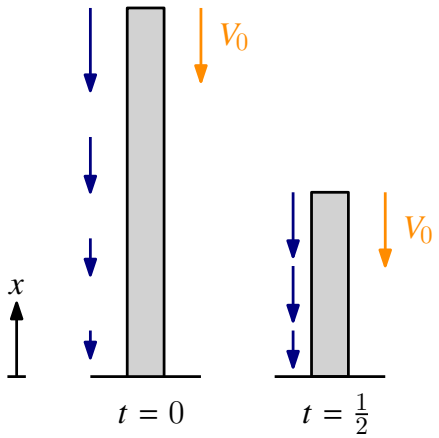

Figure 2.2: A body with initial configuration $\mathcal{M}(0) = [0, L]$ compresses into $\mathcal{M}(\frac{L}{2V_0}) = [0, \frac{L}{2}]$.

Henceforth, all fields will be given in Eulerian description, but we remark that physical laws are sometimes stated from a Lagrangian point-of-view, which motivates the introduction of the *material derivative*.

For a volumetric density $\vartheta = \vartheta(\boldsymbol{x}, t)$ of material property of a body moving with velocity field $\boldsymbol{v} = \boldsymbol{v}(\boldsymbol{x}, t)$, its material derivative (or total time derivative) $\mathrm{D}_t^{\boldsymbol{v}}\vartheta$ is given by

$$\mathrm{D}_t^{\boldsymbol{v}}\vartheta(\boldsymbol{x}, t) := \frac{\partial}{\partial t}\vartheta + \boldsymbol{v} \cdot \nabla\vartheta. \tag{2.1}$$

If $\Theta = \Theta(\boldsymbol{X}, t)$ is the material description of ϑ, then it holds that

$$\dot{\Theta}(\boldsymbol{X}(\boldsymbol{x}, t), t) = \mathrm{D}_t^{\boldsymbol{v}}\vartheta(\boldsymbol{x}, t).$$

For a density ϑ, we define the total amount in $\Omega \subset \mathcal{M}$ at time t as

$$\mathcal{Q}(\vartheta, t) := \int_{\Omega(t)} \vartheta(\cdot, t)\mathrm{d}V_{\boldsymbol{x}}, \tag{2.2}$$

where we note that $\Omega = \Omega(t) \subset \mathcal{M}(t)$ also moves in space with the same velocity field $\boldsymbol{v}$ as $\mathcal{M}$. We can relate the change in time of this total amount with the material derivative

using the Reynolds transport theorem as follows:

$$\frac{\mathrm{d}}{\mathrm{d}t}\mathcal{Q}_\Omega(\vartheta, t) = \int_\Omega \mathrm{D}_t^{\boldsymbol{v}}\vartheta + \vartheta(\nabla \cdot \boldsymbol{v})\mathrm{d}V_{\boldsymbol{x}}. \tag{2.3}$$

Note that if one has the following integral form of a balance law

$$\frac{\mathrm{d}}{\mathrm{d}t}\mathcal{Q}_\Omega(\vartheta, t) = \int_\Omega \varpi(\cdot, t)\mathrm{d}V_{\boldsymbol{x}} \tag{2.4}$$

for some spatial field ϖ and any $\Omega \subset \mathcal{M}$, then one can pass it to differential form using Equation (2.3) and, using a localization theorem, write

$$\mathrm{D}_t^{\boldsymbol{v}}\vartheta = \varpi - \vartheta(\nabla \cdot \boldsymbol{v}). \tag{2.5}$$

Noting that

$$\mathrm{D}_t^{\boldsymbol{v}}\vartheta + \vartheta(\nabla \cdot \boldsymbol{v}) = \frac{\partial}{\partial t}\vartheta + \nabla \cdot (\vartheta \boldsymbol{v}), \tag{2.6}$$

we obtain the balance form of Equation (2.5):

$$\frac{\partial}{\partial t}\vartheta + \nabla \cdot (\vartheta \boldsymbol{v}) = \varpi. \tag{2.7}$$

Conservation of mass and balance equation

Let $\rho = \rho(\boldsymbol{x}, t)$ be the mass density field. The law of conservation of mass states that

$$\frac{\mathrm{d}}{\mathrm{d}t}\mathcal{Q}_\Omega(\rho; t) = 0 \tag{2.8}$$

which, using Equation (2.7), can be restated as

$$\frac{\partial}{\partial t}\rho + \nabla \cdot (\rho \boldsymbol{v}) = 0, \tag{2.9}$$

which is often referred to as the *continuity equation*.

Remark. By Equations (2.5) and (2.8) together, we have

$$\mathrm{D}_t^{\boldsymbol{v}}\rho = -\rho\nabla \cdot \boldsymbol{v}.$$

If we take the velocity field of Example 2.1.1, we see that

$$\nabla \cdot \boldsymbol{v} = -\frac{1}{1-t} < 0,$$

and so $\mathrm{D}_t^{\boldsymbol{v}}\rho > 0$. In other words, as we follow a particle, the volumetric density increases and a hitchhiker riding with the particle would feel as if things were "getting crowded". Therefore, in the absence of mass-changing reactions, we say that the body will be *compressing* if $\nabla \cdot \boldsymbol{v} < 0$ or *expanding* if $\nabla \cdot \boldsymbol{v} > 0$.

If, however, there exist mass-changing reactions involving $\mathcal{M}$, we will have

$$\frac{\mathrm{d}}{\mathrm{d}t}\mathcal{Q}_\Omega(\rho, t) = \int_\Omega r(\cdot, t)\mathrm{d}V_{\boldsymbol{x}}. \tag{2.10}$$

where r is the reaction rate per unit volume which depends on ρ and usually more variables (e.g. the concentration of a nutrient), which leaves us with the balance equation

$$\frac{\partial}{\partial t}\rho + \nabla \cdot (\rho \boldsymbol{v}) = r. \tag{2.11}$$

We note that, if one considers a closed system with N components each with their densities ρ_i and reaction rates r_i, then the conservation of mass states that

$$\sum_{i=1}^{N} r_i = 0$$

and we recover Equation (2.9) for $\rho = \sum_{i=1}^{N} \rho_i$.

Conservation of linear momentum

By Newton's second law, we have that the change of momentum of a body is equal to the sum of external forces acting on it, that is,

$$\frac{\mathrm{d}}{\mathrm{d}t}\mathcal{Q}_\Omega(\rho v_i, t) = \int_{\partial\Omega} t_i \mathrm{d}S_{\boldsymbol{x}} + \int_\Omega b_i \mathrm{d}V_{\boldsymbol{x}}, \qquad i = 1, 2, 3, \tag{2.12}$$

where v_i is the i-th component of $\boldsymbol{v}$, t_i is the surface density of external tractions in the direction of $\boldsymbol{x}_i$, and b_i is the density of a body force (e.g. weight) in the same direction.

Using the Cauchy stress tensor $\mathbb{S}$, which represents the internal state of forces of $\mathcal{M}$, we have that the traction field t_i is given by

$$t_i = (\mathbb{S}\boldsymbol{\nu}_{\partial\Omega})_i,$$

where $\boldsymbol{\nu}_{\partial\Omega}$ is the exterior facing normal of Ω. Therefore, using the divergence theorem, we obtain

$$\frac{\mathrm{d}}{\mathrm{d}t}\mathcal{Q}_\Omega(\rho v_i, t) = \int_\Omega (\nabla \cdot \mathbb{S})_i \mathrm{d}V_{\boldsymbol{x}} + \int_\Omega b_i \mathrm{d}V_{\boldsymbol{x}}, \qquad i = 1, 2, 3, \tag{2.13}$$

and passing to differential form, collecting all i components into their respective vectors (in boldface), we apply Equation (2.3) to obtain

$$\frac{\partial}{\partial t}(\rho \boldsymbol{v}) + \nabla \cdot (\rho \boldsymbol{v} \otimes \boldsymbol{v}) = \nabla \cdot \mathbb{S} + \boldsymbol{b}. \tag{2.14}$$

2.2 Single-phase flow

Conservation of mass

A material is said to undergo *incompressible flow* if the velocity field satisfies

$$\nabla \cdot \boldsymbol{v} = 0. \tag{2.15}$$

The name comes from the fact that, in absence of mass-changing reactions, by Equations (2.6) and (2.9), this is equivalent to $\mathrm{D}_t^{\boldsymbol{v}} \rho \equiv 0$ and so the amount of mass of a small moving volume of fluid remains constant at all times t, i.e. it neither compresses nor expands. On the other hand, if a material were incompressible, that is, if its volume is a constant in its equation of state, then its density is also constant and Equation (2.15) follows from the continuity equation. Therefore, whenever we are talking about incompressible flows or incompressible fluids, we will identify Equation (2.15) with mass conservation.

Conservation of linear momentum

In order to find the linear momentum balance equation of a material flow, a constitutive equation for the $\mathbb{S}$ must be imposed. For fluids, in a most general sense, we can decompose the stress into spherical and deviatoric (shear) parts:

$$\mathbb{S} = \underbrace{-p\mathbb{I}}_{\text{spherical stress}} + \underbrace{\mathbb{T}_\mu}_{\text{shear stress}}, \tag{2.16}$$

where $p = p(\boldsymbol{x}, t)$ is the pressure of the fluid, $\mathbb{I}$ is the identity tensor, and $\mathbb{T}_\mu = \mathbb{T}_\mu(\boldsymbol{v}, \nabla \boldsymbol{v})$ is the viscous stress tensor. The corresponding momentum balance is then given by

$$\frac{\partial}{\partial t}(\rho \boldsymbol{v}) + \underbrace{\nabla \cdot (\rho \boldsymbol{v} \otimes \boldsymbol{v})}_{\text{inertial forces}} - \nabla \cdot \left(-p\mathbb{I} + \underbrace{\mathbb{T}_\mu(\boldsymbol{v}, \nabla \boldsymbol{v})}_{\text{viscous term}} \right) = \boldsymbol{b}. \tag{2.17}$$

Newton's law of viscosity gives the viscous stress tensor as

$$\mathbb{T}_\mu := 2\mu \mathbb{E}, \tag{2.18}$$

where μ is the viscosity, $\mathbb{E} = \mathbb{E}(\boldsymbol{v})$ is the infinitesimal rate-of-strain tensor given by

$$\mathbb{E}(\boldsymbol{v}) := \frac{1}{2}(\nabla \boldsymbol{v} + \nabla \boldsymbol{v}^{\mathsf{t}}).$$

Governing equations of single-phase fluid flow

Putting everything together, we obtain the incompressible Navier–Stokes equations

$$\nabla \cdot \boldsymbol{v} = 0 \tag{2.19a}$$

$$\frac{\partial}{\partial t}(\rho \boldsymbol{v}) + \nabla \cdot (\rho \boldsymbol{v} \otimes \boldsymbol{v}) - \nabla \cdot \left(-p\mathbb{I} + \mu(\nabla \boldsymbol{v} + \nabla \boldsymbol{v}^{\mathsf{t}})\right) = \boldsymbol{b}. \tag{2.19b}$$

In this thesis we will consider the following variations of Equation (2.19):

† Stationary flow
We consider the time evolution negligible either by assuming steady-state conditions, that is, no further evolution occurs, or by differing time frames by which we mean the existence of some secondary process that is much slower and thus it can be assumed that fluid flow is at equilibrium when looked at the larger time scale of the secondary process. In this case, we set

$$\frac{\partial}{\partial t}(\rho \boldsymbol{v}) \equiv 0.$$

All of the following formulations in the rest of the section and in Papers III–V are of this type.

† Stokes flow

Inertial forces are considered negligible either because of slow flows or high viscosity leading to the magnitude of the viscous forces to dominate the momentum balance. In this case, we set

$$\nabla \cdot (\rho \boldsymbol{v} \otimes \boldsymbol{v}) \equiv 0.$$

An advantage of this kind of flow is that the momentum balance is now linear in $\boldsymbol{v}$ (if $\boldsymbol{b}$ does not depend non-linearly on the velocity). The resulting equations are

$$-\nabla \cdot (-p\mathbb{I} + 2\mu\mathbb{E}(\boldsymbol{v})) = \boldsymbol{b} \tag{2.20}$$

This is the formulation used in Paper III.

† Stokes flow with pseudo-stress
If we take $\mathbb{S}$ defined by Equations (2.16) and (2.18) and define the pseudo-stress $\widetilde{\mathbb{S}} = \widetilde{\mathbb{S}}(\boldsymbol{v})$ by

$$\widetilde{\mathbb{S}}(\boldsymbol{v}) \coloneqq -p\mathbb{I} + \mu\nabla \boldsymbol{v}, \tag{2.21}$$

we can use the fact that $\nabla \cdot (\nabla \boldsymbol{v})^{\mathsf{t}} = \nabla(\nabla \cdot \boldsymbol{v})$ to see that incompressibility gives

$$\nabla \cdot \mathbb{S} = \nabla \cdot \widetilde{\mathbb{S}},$$

which lets us write the stationary Stokes flow equations as

$$-\nabla \cdot (-p\mathbb{I} + \mu \nabla \boldsymbol{v}) = \boldsymbol{b}, \tag{2.22}$$

or, using the vector Laplacian $\Delta \boldsymbol{u} \coloneqq \nabla \cdot (\nabla \boldsymbol{u})$,

$$-\mu \Delta_{\boldsymbol{x}} \boldsymbol{v} + \nabla p = \boldsymbol{b}. \tag{2.23}$$

This is the formulation used in Papers IV and V.

† Darcy flow
In this case, we consider stationary flow viscous forces are taken as a linear function of the fluid velocity $\boldsymbol{v}$, so that the momentum balance of Equation (2.23) is replaced by

$$-\mu \left(-\overline{\mathbb{K}}^{-1} \boldsymbol{u} \right) + \nabla p = \boldsymbol{b}$$

which can be rewritten using the constitutive equation, widely known as *Darcy's law* [Jackisch and Kröner, 2023],

$$\boldsymbol{u} = -\mathbb{K} \nabla p + \frac{1}{\mu} \boldsymbol{b}, \tag{2.24}$$

where $\mathbb{K} = \frac{1}{\mu} \overline{\mathbb{K}}$ is known as the hydraulic conductivity tensor.

Replacing Equation (2.24) in the mass balance Equation (2.15), we see that the pressure satisfies the following Poisson problem:

$$-\nabla \cdot (\mathbb{K} \nabla p) = \boldsymbol{f}, \tag{2.25}$$

where $\boldsymbol{f} = -\frac{1}{\mu} \nabla \cdot \boldsymbol{b}$.

This is the formulation used in Paper V.

2.3 Multi-phase flow

In this section, we will go over the concepts relevant to multi-phase flow, that is, a flow that is comprised of multiple components with different material properties; see [Drew and Passman, 1999]. The term multi-phase flow can refer to both flows where there exists multiple thermodynamic phases (liquid–gas mixtures), as well as mixtures with multiple components (sometimes referred to as *multi-component* flow). In this thesis we will always mean the latter when referring to multi-phase flow.

Consider a mixture made of n components with densities $\rho^{(1)}, \ldots, \rho^{(n)}$ and velocities $\boldsymbol{v}^{(1)}, \ldots, \boldsymbol{v}^{(n)}$; see Figure 2.3. In order to properly define balances of each component and

properties of the entire mixture, we introduce volume fractions $\phi^{(1)}, \ldots, \phi^{(n)}$ (all dependent on $\boldsymbol{x}$ and t) for each component such that, given a control region of volume V, the volume $V^{(i)}$ of component i is $V^{(i)} = \phi^{(i)} V$. It follows that the volume fractions satisfy

$$\sum_{i=1}^{n} \phi^{(i)} = 1. \tag{2.26}$$

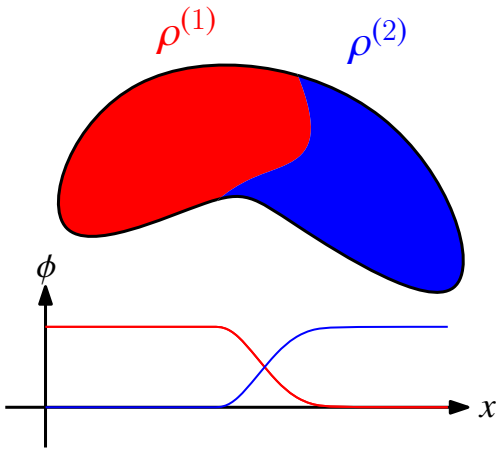

Figure 2.3: A mixture composed of two components and their cross-sectional volume fractions $\phi^{(i)}$.

The concentration $c^{(i)}$ is related to the volume fraction $\phi^{(i)}$ by

$$c^{(i)} := \frac{[\text{Mass of } i]}{[\text{Total vol.}]} = \frac{[\text{Vol. of } i]}{[\text{Total vol.}]} \frac{[\text{Mass of } i]}{[\text{Vol. of } i]} = \phi^{(i)} \rho^{(i)}. \tag{2.27}$$

The mass and momentum balances for each component are

$$\frac{\partial}{\partial t} c^{(i)} + \nabla \cdot (\boldsymbol{v}^{(i)} c^{(i)}) = r^{(i)} \tag{2.28a}$$

$$\frac{\partial}{\partial t} (c^{(i)} \boldsymbol{v}^{(i)}) + \nabla \cdot (c^{(i)} \boldsymbol{v}^{(i)} \otimes \boldsymbol{v}^{(i)}) = \nabla \cdot \mathbb{S}^{(i)} + \boldsymbol{b}^{(i)} \tag{2.28b}$$

where $r^{(i)}$ is the net rate of production of component i, in the context of this work given by ecological reactions between components (e.g. consumption, predation and inactivation); $\mathbb{S}^{(i)}$, $\boldsymbol{b}^{(i)}$ are the stress tensor and external forces per unit volume acting on component i, respectively. For the overall conservation of mass to hold, we require $\sum_{i=1}^{n} r_i = 0$.

Remark. In general, we will not solve Equation (2.28b), but instead provide *constitutive* equations for the individual velocities $\boldsymbol{v}^{(i)}$ in terms of the individual concentrations $c^{(i)}$ and the velocity of the entire mixture.

Remark. Throughout the rest of this thesis, we will assume that individual densities $\rho^{(i)}$ are constant and as such, the mass balances Equation (2.28a) become the volume-fraction balances

$$\frac{\partial}{\partial t}\phi^{(i)} + \nabla \cdot (\boldsymbol{v}^{(i)}\phi^{(i)}) = \frac{1}{\rho^{(i)}} r^{(i)}. \tag{2.29}$$

The mass of the entire mixture is given by the sum of the individual masses of each component, and so its density ρ is given by

$$\rho := \sum_{i=1}^{n} c^{(i)} = \sum_{i=1}^{n} \phi^{(i)}\rho^{(i)}. \tag{2.30}$$

On the other hand, the velocity of the mixture is *not* the sum of each individual velocity, but a weighted average of them which we refer to as the mass-averaged velocity

$$\boldsymbol{v}_{\mathrm{m}} := \frac{1}{\rho} \sum_{i=1}^{n} \phi^{(i)}\rho^{(i)}\boldsymbol{v}^{(i)}. \tag{2.31}$$

We note that Equation (2.31) is the correct velocity field for Equation (2.9) to hold, but it is not, in general, divergence free. This restricts it to a smaller theoretical framework as there is a vast amount of work on incompressible flow that we would like to leverage. On the other hand, by summing Equation (2.28a) and using Equation (2.26), we arrive at the following time-independent equation

$$\sum_{i=1}^{n} \frac{r^{(i)}}{\rho^{(i)}} = \sum_{i=1}^{n} \left(\frac{\partial}{\partial t}\phi^{(i)} + \nabla \cdot (\boldsymbol{v}^{(i)}\phi^{(i)}) \right) \tag{2.32}$$

$$= \frac{\partial}{\partial t} \underbrace{\left(\sum_{i=1}^{n} \phi^{(i)} \right)}_{=1} + \nabla \cdot \left(\sum_{i=1}^{n} \boldsymbol{v}^{(i)}\phi^{(i)} \right) \tag{2.33}$$

$$= \nabla \cdot \left(\sum_{i=1}^{n} \boldsymbol{v}^{(i)}\phi^{(i)} \right) \tag{2.34}$$

which motivates the introduction of the following quantity

$$\boldsymbol{q} := \sum_{i=1}^{n} \boldsymbol{v}^{(i)}\phi^{(i)}, \tag{2.35}$$

which we can interpret as the *volume-averaged* velocity of the mixture.

The term in the left-hand side of Equation (2.32) is usually found to be negligible after dimensional analysis, and so this newfound velocity $\boldsymbol{q}$ corresponds to an incompressible flow. By restating the mass and linear momentum balances in terms of $\boldsymbol{q}$ instead of $\boldsymbol{v}_{\mathrm{m}}$, we can find new flow equations which are more convenient to work with.

Example 2.3.1. *Consider a closed vertical container with a mixture of suspended particles in a solvent with densities $\rho_p > \rho_s$; see Figure 2.4. Since the particles have a higher density than the solvent, they will settle to the bottom of the container. Adopting a standard model of sedimentation [Bürger et al., 2011], the relative velocity at which the particles fall can be modelled as*

$$v_{rel} = \frac{v_{hs}(\phi)}{1-\phi},$$

where v_{hs} is the so-called hindered settling velocity [Torfs et al., 2017], which in this example will be taken as

$$v_{hs}(\phi) := \exp(-\phi),$$

where $\phi = \phi(t,z)$ is the volume fraction of the suspended solids. Since the container is closed, there is no volumetric in- or outflow, and so the volume-averaged velocity is

$$q = 0. \tag{2.36}$$

With q and v_{rel}, we can deduce the individual velocities of each phase from Equation (2.35)

$$v_p(\phi) = v_{hs}(\phi), \qquad v_s(\phi) = -\frac{v_{hs}(\phi)\phi}{1-\phi}, \tag{2.37}$$

and it follows by Equation (2.31) that the mass-averaged velocity is

$$v_m = \frac{(\rho_p - \rho_s)}{\rho_s + \phi(\rho_p - \rho_s)} v_{hs}(\phi)\phi.$$

With this, we see that, even if we consider a closed container such that the volume of the mixture remains stationary, the subphases can be constantly moving. However, if we look at the velocity following the mass *of the mixture, it stands to reason that this one is not stationary. Since the particles are denser and falling, the mixture* must *get denser at the bottom as settling happens.*

In general, the relationship between $\boldsymbol{v}_m$ and $\boldsymbol{q}$ is given by

$$\boldsymbol{v}_m - \boldsymbol{q} = \sum_{i=1}^{n} \frac{\rho^{(i)} - \rho}{\rho} \phi^{(i)} \boldsymbol{v}^{(i)} \tag{2.38}$$

where the right-hand side is quite complicated to work with for mixtures with $n > 2$ components. However, for $n = 2$ it is possible to find an explicit expression in terms of the slip velocity between components.

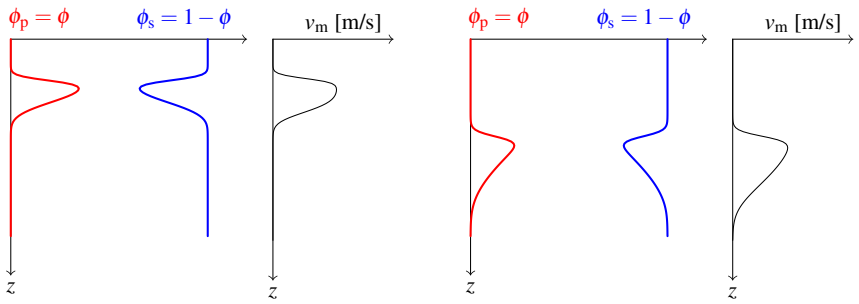

(a) $T = 0.1$ (b) $T = 0.5$

Figure 2.4: Volume fractions ϕ and mass-averaged velocity v_m of a mixture of settling particles in a vertical solution. The volume-averaged velocity q is zero everywhere at all times $T > 0$.

Two-phase flow

If we take $n = 2$, the situation simplifies greatly. In such case, we can set $\phi := \phi^{(1)}$ from which it follows that $\phi^{(2)} = 1 - \phi$, and so $c^{(2)} = (1 - \phi)\rho^{(2)}$ is completely determined by the volume fraction ϕ of component 1. Furthermore,

$$\boldsymbol{v}_m - \boldsymbol{q} = \frac{1}{\rho}(1 - \phi)\phi(\rho^{(1)} - \rho^{(2)})(\boldsymbol{v}^{(1)} - \boldsymbol{v}^{(2)})$$

which suggests we introduce the density difference and relative velocity:

$$\Delta\rho := \rho^{(1)} - \rho^{(2)}, \qquad \boldsymbol{v}_{rel} := \boldsymbol{v}^{(1)} - \boldsymbol{v}^{(2)}.$$

We have that the relationship between mass-averaged and volume-averaged velocities is given by

$$\boldsymbol{v}_m = \boldsymbol{q} + \frac{\Delta\rho}{\rho}(1 - \phi)\phi\boldsymbol{v}_{rel}$$

Given $\boldsymbol{q}$ and $\boldsymbol{v}_{rel}$, it is possible to determine the individual velocities $\boldsymbol{v}^{(i)}$ (and vice versa). Since the concentration of component 2 is completely determined by that of component 1, we find that it suffices to solve

$$\frac{\partial}{\partial t}\phi + \nabla \cdot (\phi\boldsymbol{q} + (1 - \phi)\phi\boldsymbol{v}_{rel}) = \frac{r^{(1)}}{\rho^{(1)}}, \tag{2.39a}$$

$$-\nabla \cdot \mathbb{T}_\mu(\boldsymbol{q}) + \nabla p = \boldsymbol{f}, \tag{2.39b}$$

$$\nabla \cdot \boldsymbol{q} = 0, \tag{2.39c}$$

where we have omitted the inertial terms and write $\boldsymbol{f}$ grouping all forces acting on the mixture.

The choice of $\boldsymbol{v}_{\text{rel}}$ and $\boldsymbol{f}$ determines the kind of mixture we will be working with. For example, in the case of sedimentation [Kynch, 1952, Bürger et al., 2000], the relative velocity is given by the batch flux density and $\boldsymbol{f}$ accounts for extra solid stressed amounting to compression effects.

2.4 Cahn–Hilliard models for phase separation

In a series of articles [Cahn and Hilliard, 1958, 1959, Cahn, 1959], Cahn and Hilliard introduced a model for the energy associated to the phase separation of a binary mixture. For a general review of the Cahn–Hilliard equation, we refer the reader to [Miranville, 2019]. This model has found many different applications in engineering [Kim et al., 2016] and, in particular, biology [Cohen and Murray, 1981, Ebenbeck and Garcke, 2019]. We highlight the works of Klapper and Dockery [2006, 2010] and Zhang et al. [2008], who used the Cahn–Hilliard equation to model the cohesion of biofilms, which becomes the basis for the models in Papers I–III. Analysis of the continuous solutions for Cahn–Hilliard-type systems modelling biofilms can be found in [Helmer and Jüngel, 2023].

For a mixture of components 1 and 2 with order parameter ϕ, which we place in $[0, 1]$ and interpret as the volume fraction of Component 1 in the mixture. Under assumption of constant temperature, no mass-changing reactions, no convective flow and no external forces acting on the mixture, the following holds

$$\frac{\partial}{\partial t}\phi + \nabla \cdot (\lambda(\phi)\nabla(-\kappa\Delta\phi + \Psi'(\phi))) = 0, \tag{2.40}$$

where $\lambda(\phi)$ is the mobility function, $\Psi = \Psi(\phi)$ is the homogeneous cohesion energy density, and $\kappa > 0$ is a coefficient related to the boundary layer thickness.

Introducing the additional unknown μ, sometimes called the chemical potential or osmotic pressure [Cogan, 2004], we can restate Equation (2.40) as a system:

$$\frac{\partial}{\partial t}\phi + \nabla \cdot (\lambda(\phi)\nabla\mu) = 0, \tag{2.41a}$$

$$\mu + \kappa\Delta\phi - \Psi'(\phi) = 0 \tag{2.41b}$$

Modifications of Equation (2.41) include the addition of convection-driven movement and

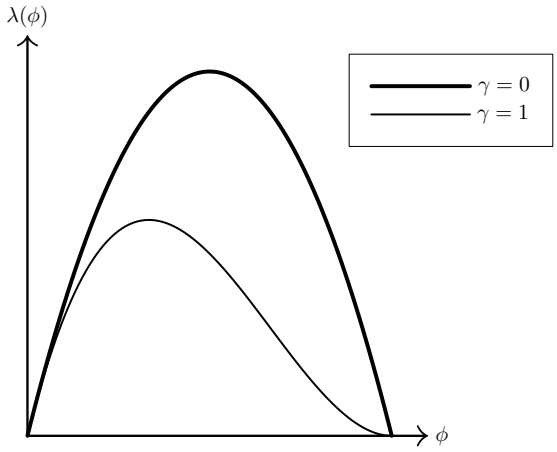

Figure 2.5: Volume-fraction-dependent mobility function $\lambda(\phi) = \phi(1-\phi)^\gamma$. The mobility degenerates when $\phi \in \{0, 1\}$, as there is no separation flux in pure-phase regions. For most applications, $\gamma = 0$, but other values can be used to model cell squeezing, for instance [Wang and Hillen, 2007].

the addition of source term. In such case, the resulting system is

$$\frac{\partial}{\partial t}\phi + \nabla \cdot (\phi \boldsymbol{q} + \lambda(\phi)\nabla\mu) = g, \tag{2.42a}$$

$$\mu + \kappa\Delta\phi - \Psi'(\phi) = 0 \tag{2.42b}$$

which we compare with Equation (2.39) to see that both coincide if we set

$$\lambda(\phi) = \phi(1-\phi), \tag{2.43}$$

$$\boldsymbol{v}_{\text{rel}} = -\lambda_0 \nabla\mu, \tag{2.44}$$

with $\lambda(\phi)$ (see Figure 2.5) coinciding exactly with the usual degenerate mobility used in various works [Elliott and Garcke, 1996, Barrett et al., 1999, Dziwnik, 2019, Guillén-González and Tierra, 2024]. The degenerate mobility poses some difficulties in the analysis and development of numerical methods. For example, even if the Cahn–Hilliard equation is always non-linear due to the potential term $\Psi'(\phi)$, it is possible to derive linear methods by means of implicit-explicit schemes utilizing an Eyre splitting [Eyre, 1998]. However, a volume-fraction-dependent mobility makes linearization difficult. The form of $\boldsymbol{v}_{\text{rel}}$ is consistent with the kinetic theory of biofilms presented by Wang and Zhang [2012], taking the role of what they call excessive polymer velocity.

Remark. The induced velocity function of Equation (2.42a) with Equations (2.43) and (2.44) is

$$\boldsymbol{v}_{\text{CH}}(\phi; \nabla\mu) := \boldsymbol{q} - \lambda_0(1-\phi)\nabla\mu \tag{2.45}$$

and we can see that it degenerates to a convective velocity when $\phi = 1$. This limits, independently of the form of μ, the phase-separation flux only to interfacial regions, that is, regions where $0 < \phi < 1$.

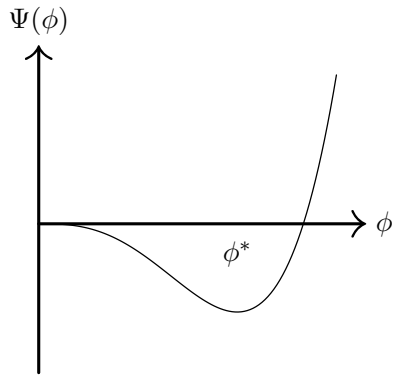

Figure 2.6: Single-well potential suggests that the mixture has a single preferred equilibrium state $\phi = \phi^*$.

Regarding the choice of Ψ, the most commonly used potentials are the logarithmic Flory-Huggins potential [Flory, 1953] and its approximation by a polynomial double well [Garcke et al., 2023] with two minima at $\phi = \pm 1$. However, the choice of non-symmetric potentials has been covered from a theoretical perspective [Benci et al., 2020] and are of particular interest in biological applications [Klapper and Dockery, 2006, Cogan, 2004, Chatelain et al., 2011, Grasselli et al., 2026] due to the nature of cell adhesion. In particular, for the models developed in this work, we focus on the single-well potential given by [Klapper and Dockery, 2006]; see Figure 2.6.

Part I

Modelling slow sand filtration

Chapter 3

Introduction

3.1 Historical overview

The need for drinking water for the survival of an individual is evident, and as such it follows that a community would strive to procure steady access to pure, drinkable water for prolonged sustainment. As sources of clean water in nature are scarce and dependent on the seasons, and as human settlements have grown in size and complexity, finding a constantly accessible source of drinkable water poses a near-impossible challenge. For that reason, efforts have been put towards engineering reliable methods for drinking water treatment from raw sources, for which we can mention sedimentation, chlorination and filtration, for example.

Filtration is a water treatment method in which raw water flows through porous material (the *medium*, often sand), removing impurities by straining and, as we will see later, multiple other mechanisms. It constitutes the mechanism of the first large-scale deployments of raw water treatment in human history and has been a subject of study for centuries at this point. Evidence of its impact on societal development can be seen in Tables 3.1 and 3.2, where a sharp decrease in deaths by Cholera can be atrributed to the Metropolis Water Act of 1852, preventing domestic use of water from the River Thames in favor of the filtered water provided by water companies. Special consideration should be taken when looking at Paisley, whose water supply to the whole city had long been filtered by 1849.

While evidence of household filters in England date back to 1790 and the work of Johanna Hempsel, the first city-wide supply of filtered water takes place in 1804 in Paisley by the hand of John Gibb, who had a sand filter installed for providing clean water to his bleachery and sold the surplus to the townspeople [Baker, 1949]. Subsequent filters were built in Glasgow by different water companies to varying degree of success due to constant sur-

Table 3.1: Cholera deaths in London, England. Rivers Pollution Commission Report, 1874

LONDON			
Year	Character of water	Number of deaths	Per 10 000
1832	Polluted	5275	31.4
1849	Very much polluted	14137	61.8
1854	Less polluted	10738	42.9
1866	Much less polluted	5596	18.4

Table 3.2: Cholera deaths in Paisley and Charleston, Scotland. Rivers Pollution Commission Report, 1874

PAISLEY AND CHARLESTON		
Year	Character of water	Number of deaths
1832	Polluted water	182
1854	Polluted water	173
1866	Pure water	7

face clogging. Then, in 1829, James Simpson completes his experimental sand filter while working for the Chelsea Water Company in London and a permanent filter is ordered for construction by the Royal Commission. Simpson's filter built upon the previous iterations of sand filters and, in a similar manner to another sand filter from 1827 in Glasgow by Robert Thom, placed the sand bed in ascending porosity, with the finer medium at the top and a coarse layer of gravel at the bottom, improving filtration rate; see Figure 3.1.

A key difference between the designs of Thom and Simpson, is that the former deals with clogging by a process of backwashing, in which the sand bed is cleaned by essentially running the filter in reverse, whereas the latter opts for a draining of the filter followed by scraping the top layer of sand before restarting function. It would be Simpson's design that stands the test of time mostly unmodified, but features of Thom's sand filter such as the backwash and a false bottom on which the medium is supported, would be utilized in the sand filters built in North America during the 1880s, with the biggest difference being that the American filters would be run at 50 times the volumetric flow of the European ones, answering to the lack of land space in the cities where they were deployed. These smaller, faster filters would later be classified as *rapid sand filters*, whereas sand filters that follow Simpson's design would, in contrast, be labelled *slow sand filters* (SSF).

Compared to other water treatment mechanisms, slow sand filtration offers a sustainable option as it does not require electricity and the simplicity of its design makes it suitable for deployment in rural areas. However, it does require a large surface area to account for

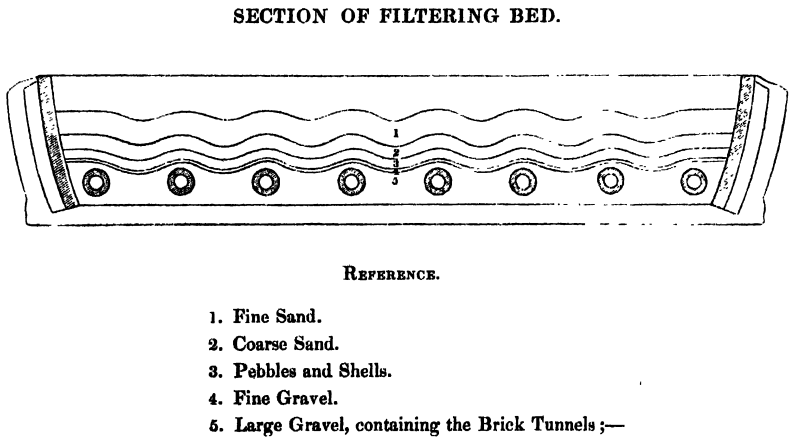

Figure 3.1: Drawing of the filter in use by the Chelsea Water Works to filter water from the River Thames, communicated in a letter from James Simpson to Thomas Telford, published in the latter's autobiography *The Life of Thomas Telford, Civil Engineer (1838)*, edited by John Rickman and published in London by Payne and Foss.

the low volumetric flow required for its operation (somewhere between 0.2 and 0.4 m^3 per hour) and regular maintenance to avoid clogging. As water engineering progresses, it stands to question whether slow sand filtration is but a relic of the past, overshadowed and objectively surpassed by its successors in chemical-based disinfection, UV light treatments and rapid sand filters themselves, perhaps only to be used in the most simplest of situations. However, a main feature present in slow sand filtration that is not in the other mentioned treatment processes, is that the organic matter that attached to the medium and develops and leads to clogging, as recognized by Thom and Simpson, is actually a powerful filtration enhancer, a *biofilter* that allows us to leverage the existing ecology of water sources into effective producers of potable water. In the words of Samuel Rideal [1902]:

> Sand filters were first regarded simply as strainers; and the fineness and cleanness of the sand was the most important point. Analyses later proving that the soluble constitutents were considerabl affected, an explanation was sought in surface action. [...] It was proved, therefore, that for the proper mechanical and chemical effects the action of organisms is essential. It must be remembred that some organisms have long flagella, while a large number, such as diatoms and bacteria, are normally surrounded by a gelatinous envelope which greatly increases their size, and enables them to adhere to surfaces, so that in a short time the sand of a new filter becomes covered with a living slimy layer which entangles suspended matters and effects the main part of the purification. This is called *Schmutzdecke*.

It is, in fact, this dirt layer (Schmutzdecke), and more precisely the entire biofilm network formed in a filter and how it is formed by the settlement of microorganisms immersed in and interacting with a complex surrounding ecological system that constitutes the primary interest of the model presented in the first part of this thesis. This biofilm network is highly porous [Melo, 2005] and these pores act as nutrient storage [Quan et al., 2022], a feature which is not usually accounted for in the existing models of slow sand filtration.

3.2 The mechanisms of slow sand filtration

Modern SSFs are gravity-driven filters where, as water flows down through the medium, contaminants are removed by both physical and biological processes [Maiyo et al., 2023]. SSFs are in continuous operation, with a raw water feed usually connected to a larger network of treatment processes, such as flocculation basins and sedimentation plants, only stopping operation to clean the filter by, for instance, scraping off the top layer to prevent clogging. Batch-type filters also exist in smaller scales, and are usually referred to as biosand filters [Maiyo et al., 2023], and filters in which scraping is replaced by backwashing similar to Thom's original design also exist [De Souza et al., 2016].

An SSF is, generally speaking, comprised of two discrete layers (see Figure 3.2): the saturated medium or *sandbed* (roughly 0.6 m to 1.2 m), and the volume of water that sits on top of it (to a depth of 1 m to 1.5 m), the *supernatant water* [Huisman and Wood, 1974]. Additionally, the medium is further divided into a larger sand layer followed by layers of fine and coarse gravel at the bottom. Contaminants present in the water influx are strained by the medium and removed from the outflow, with the biomass enhancing turbidity-removal functions by acting as a biofilter.

Contaminants in the water supply are treated in an SSF through two classes of filtration mechanisms: physico-chemical mechanisms and biological mechanisms [Guchi, 2017].

3.2.1 Physico-chemical removal mechanisms

Denser-than-water particles in the filter, such as large micro-organisms like protozoa, sediment in the supernatant water due to gravity and density differences. On the other hand, overall downward direction of the water flow advects dissolved components, which are additionally dispersed in the liquid suspension.

Out of the particulate material, those with larger diameter are strained by the upper layers of the sand and prevented from continuing down. Smaller-sized material may then attach to the sand grains through adsorption, which is the process by which molecules attach to surfaces due to van der Waals forces. These form the basis for the attachment mechanism

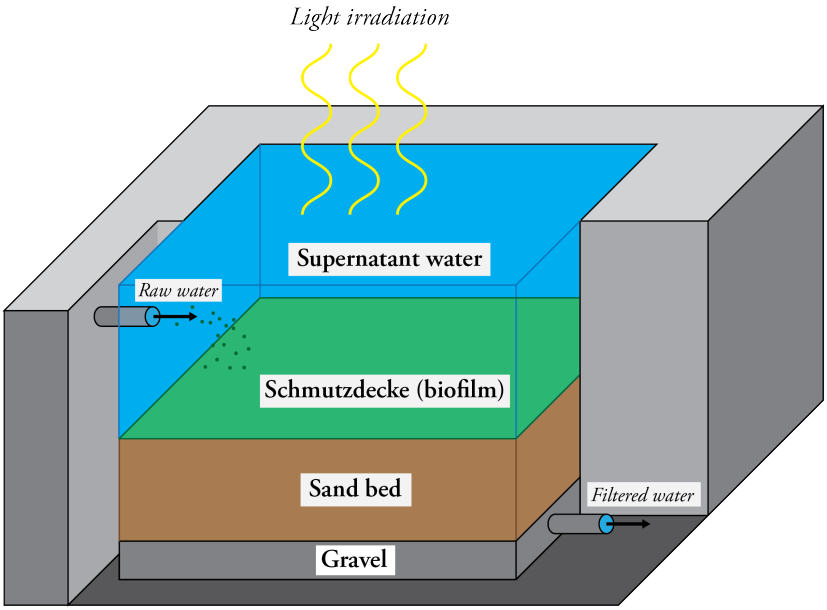

Figure 3.2: An uncovered SSF. Usual large-scale installations consist of several side-by-side filters with rectangular cross-sections. Circular cross-sections can are more common in singular small-scale operations.

in an SSF, with an emphasis on the Schmutzdecke which is later removed during scraping, effectively eliminated from the filter over time. It is of note that these attachment mechanisms are enhanced over time due to the accumulation of organic matter and the subsequent development of biofilm in the medium, reducing the pore size and increasing the catch-rate of the filter. This, in turn, causes an increase in hydrodynamic shear forces, causing detachment of particles into the flowing suspension.

3.2.2 Biological removal mechanisms

The ecological community of an SSF is incredibly rich [Rosenqvist et al., 2025]. Harmful microorganisms are filtered by the biofilm in two major ways: predatory activity by existing microorganisms in the filter, and increased inactivation rates by bioantagonism. In fact, while consumption of a microorganism by another is the primary way of biological removal in an SSF, the successive colonization of the filter creates an environment where well-settled species have an ecological advantage over the incoming ones. In a sense, the biofilm members out-compete [Guchi, 2017] incoming pathogenic bacteria by, for instance, reducing the available biomatter for growth and, the former being already adapted to the low-nutrient environment of the filter, outlive and hinder the development of the

latter.

3.3 Mathematical models of slow sand filtration

In contrast with the widespread and longstanding use of slow sand filtration in water treatment, the literature on mathematical models of it is rather sparse. While models of filtration are numerous—flow in porous media is one of the most studied effects in hydraulics—models including the biofiltration aspect are not.

In this section, we explore four models for slow sand filtration present their mathematical framework and compare them in order to motivate our model. Earlier simulations of slow sand filtration exist, but they focused only on the calibration of parameters for the estimation of headloss (*pressure drop*) at the output, without taking into account variations within the filter; see [Woodward and Ta, 1988, Jabur et al., 1994].

3.3.1 The model by Ojha and Graham (1994)

This model was presented in [Ojha and Graham, 1994]. It is one-dimensional in space and time-dependent. However, the governing equations are simplified so that the spatial terms are first solved exactly by another linear time-independent equation, resulting in a time-dependent ODE. A summary schematic of the model can be found in Figure 3.3.

The model aims to estimate the headloss h as a function of the volume of deposited solids σ and the porosity of the filter. The headloss is in turn wanted for estimating the clogging of the filter, as a higher pressure drop results in lower filtration rate.

Geometry

Only the sand is considered in this model, omitting both the supernatant water and the Schmutzdecke, in this work defined as the surface skin above the sand bed. The medium is considered to have depth L and an initial porosity ϵ_0.

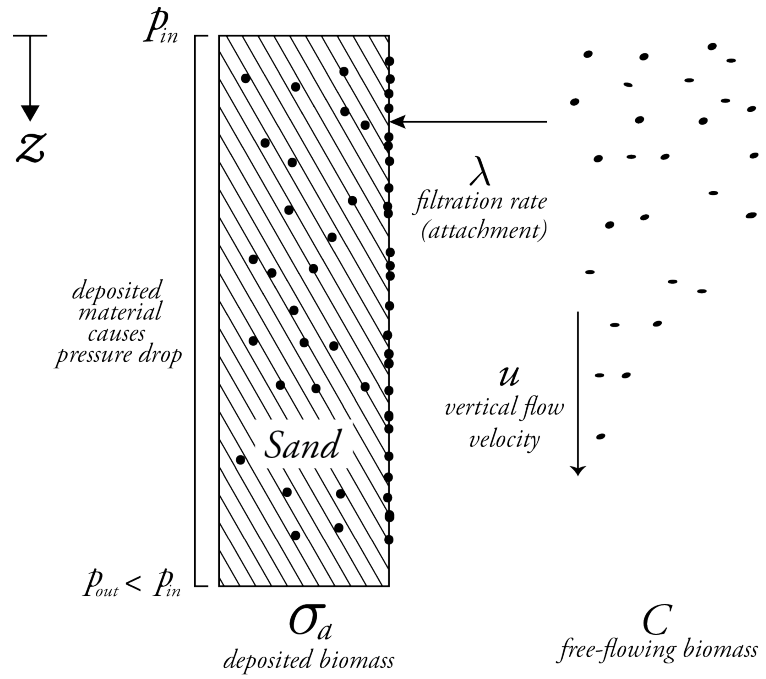

Figure 3.3: Schematic summary of the model by Ojha and Graham [1994]. While the vertical flow velocity u is taken into account, it does not translate to advective transport in the flowing biomass and only affects the biomass deposit rate.

Governing equations

The governing equations are based on the model of deep bed filtration by Iwasaki [1937] in which the following hold:

$$u\frac{\partial C}{\partial z} + \frac{\partial \sigma_{\mathrm{a}}}{\partial t} = 0, \tag{3.1a}$$

$$\frac{\partial C}{\partial z} = -\lambda C, \tag{3.1b}$$

where z is the depth, C is the concentration of a particle [mass/volume], σ_{a} is absolute specific deposit [mass/volume], u is the flow velocity and λ is the filtration coefficient.

Remark. Note that Equation (3.1a) is referred to as the *continuity equation* in the cited work. However, comparing with Equation (2.28a) and eq. (2.31), we conclude that the velocity for the absolute deposit is assumed to be zero and the time derivative for C has been omitted. In [White and Kavanaugh, 1970], the missing term is shown to be proportional to a difference between two parameters. We assume that the authors assumed this difference to be negligible.

By defining a bulk factor b [volume/mass], the bulk specific deposit σ [volume/volume] is defined as $\sigma := b\sigma_a$ and Equation (3.1a) can be written as

$$\frac{\partial \sigma}{\partial t} = -ub\frac{\partial C}{\partial z}. \tag{3.2}$$

In the setting of ordinary filtration, the bulk factor is $b = (1 - \epsilon_d)^{-1}$, where ϵ_d is the porosity of deposited soliuds. In order to incorporate the effect of microbiological activity, the bulk factor b is replaced in Equation (3.2) by the biological bulk factor

$$\theta = \frac{x}{1 - \epsilon_d} + k\frac{1 - x}{1 - \epsilon_d},$$

where x is the fraction of influent concentration available for biomass development and k is a positive coefficient.

By assuming λ constant and an influx concentration C_0, Equation (3.1b) is solved exactly to obtain $C = C_0 e^{-\lambda z}$, after which Equation (3.2) is integrated from 0 to z, holding σ constant in space, resulting in

$$\frac{\partial \sigma}{\partial t} = u\theta C_0 \frac{1 - e^{-\lambda z}}{z}, \qquad z > 0. \tag{3.3}$$

Although the filtration coefficient is assumed constant in the derivation of Equation (3.3), the model considers two options for its functional dependence on σ:

$$\lambda = \lambda_0 \left(1 - \frac{\sigma}{\sigma_u}\right) \quad \text{or} \quad \lambda = \lambda_0 + a_1\sigma - a_2\frac{\sigma^2}{\epsilon_0 - \sigma},$$

where λ_0 is the initial filtration rate, σ_u is the ultimate volume of deposited solids before filtration fails, and a_1, a_2 are empirical constants.

Finally, given a choice of λ, one can numerically solve for σ and then compute the headloss h from either of two choices:

$$h = h_0 \left(\frac{\sigma_u}{\sigma_u - \sigma}\right) \quad \text{or} \quad h = h_0 \left(1 + \frac{\sigma}{1 - \epsilon_0}\right)^{c_1} \left(\frac{\epsilon_0}{\epsilon_0 - \sigma}\right)^{c_2},$$

where h_0 is the headloss across the filter containing no deposited solids and c_1, c_2 are empirical constants.

Numerical method

A finite-difference scheme [LeVeque, 2007] is used to solve the time-dependent equations. No further details are given in the original work.

3.3.2 The model by Campos et al. (2006)

This model was presented in [Campos et al., 2006] and improves upon the SSF-O model both by extending the geometry to include the supernatant water, as well as by including the microbial dynamics. In essence, one can see the model as a 0D-1D coupled system between a completely-mixed compartment and two vertically stacked regions of porous media. A summary schematic of this model is found in Figure 3.4.

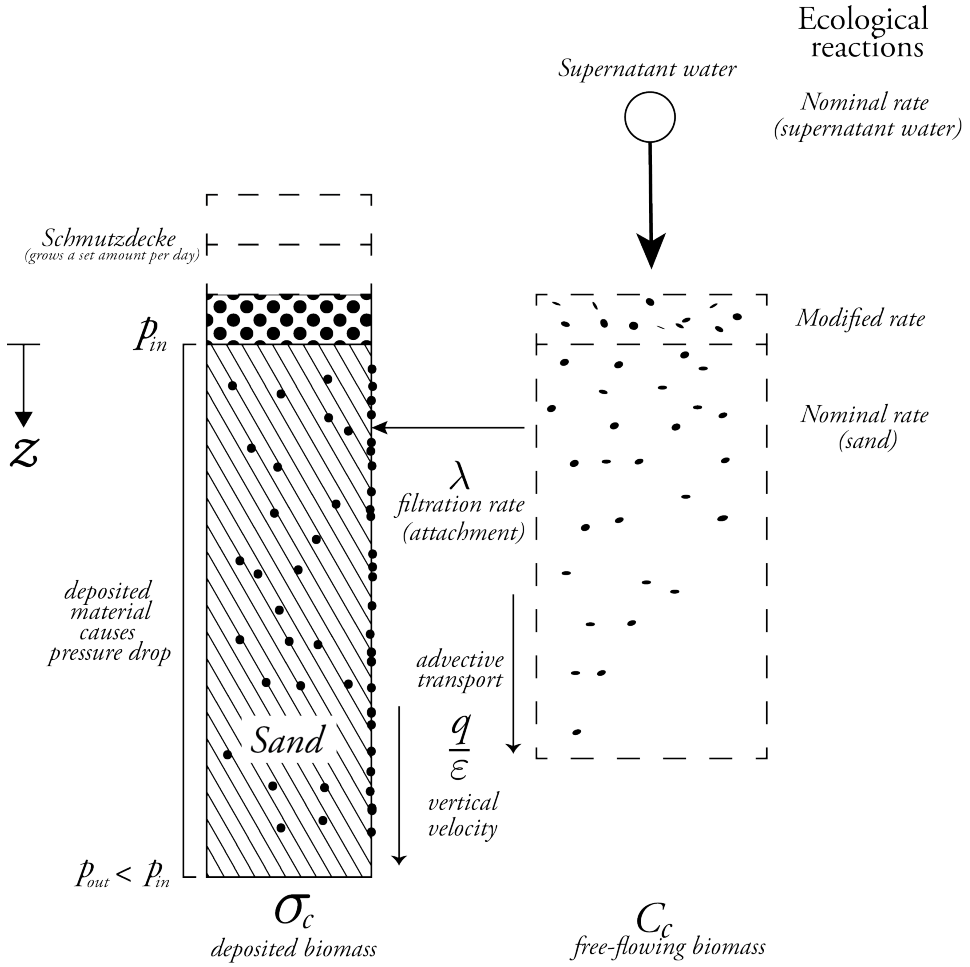

Figure 3.4: Summary schematic of the model by Campos et al. [2006] model. The Schmutzdecke consists of layers of uniform height which are "activated" at a fixed times, modelling the upwards growth of the biofilm.

Geometry

The filter is divided into three regions: the supernatant water (SW), the sand bed at the bottom (SB) and the Schmutzdecke (SD), in this case defined as the layer of biomass between the water and the medium. The SW region is completely homogeneous, whereas the SB is a one-dimensional domain discretized with a regular equidistant grid of length ΔL_{SB}. The SD region is discretized by a variable number $N_{\mathrm{SD}}(t)$ of cells (layers) of fixed length ΔL_{SD} where

$$N_{\mathrm{SD}}(t) = \left\lceil \frac{t - t_{\mathrm{lag}}}{t_{\mathrm{grow}}} \right\rceil + t_{\mathrm{grow}},$$

where t is the simulation time and $t_{\mathrm{lag}}, t_{\mathrm{grow}}$ are positive integer constants.

Governing equations

While it is not explicitly stated in the work of Campos et al. [2006], it must be assumed that the influent concentration enters the supernatant water compartment through advective flux, the same which is then fed to the Schmutzdecke compartment.

For an arbitrary component with concentration $C_c = C_c(t)$ in the supernatant water, the following holds:

$$\frac{\mathrm{d}C_c}{\mathrm{d}t} = R_C + qC_{\mathrm{in}} - qC \tag{3.5}$$

where R_C is a component-dependent reaction term, q is the volumetric flow at the influent and C_{in} is the influent concentration, with C the concentration of either algae a, dissolved phosphorus p_{s}, ammonium nitrogen n_{a} or nitrate nitrogen n_{i}. For the sake of brevity, only the full equation of algae a is given below:

$$R_a := k_{\mathrm{g,max}}\theta^{T-293} \min\left(\frac{n_{\mathrm{a}} + n_{\mathrm{i}}}{k_{\mathrm{sn}} + n_{\mathrm{a}} + n_{\mathrm{i}}}, \frac{p_{\mathrm{s}}}{k_{\mathrm{sp}} + p_{\mathrm{s}}}\right) f_{\mathrm{light}}(I, H)a - k_{\mathrm{ra}}a,$$

where θ, $k_{\mathrm{g,max}}$, k_{sn}, k_{sp} and k_{ra} are positive constants, T is the temperature, and f_{light} is a function of the light irradiation $I = I(t)$ available to the filter and its water depth $H = H(t)$ which is given by

$$H(t) := H(0) - \Delta L_{\mathrm{SD}} N_{\mathrm{SD}}(t).$$

In both the SD and SB regions, components are assumed to follow the Iwasaki filtration equations, so that a generic component with concentration $C_c = C_c(t, z)$ and bulk specific

deposit $\sigma_c = \sigma_c(t, z)$ satisfies

$$\frac{\partial C_c}{\partial t} + \frac{q}{\epsilon}\frac{\partial C_c}{\partial z} + \frac{1}{b}\frac{\partial \sigma_c}{\partial t} = R_c, \tag{3.6}$$

$$\frac{\partial C_c}{\partial z} + \left(\lambda_0 + a_1\sigma_c - a_2\frac{\sigma_c^2}{\epsilon}\right) C_c = 0, \tag{3.7}$$

where $\epsilon := \epsilon_0 - \sigma$ is the porosity of the filter, ϵ_0 is the initial porosity, $\sigma := \sum_{c \text{ not dissolved}} \sigma_c$ is the total bulk specific deposit, λ_0 is a positive constant and R_c is a component-specific reaction term. The components considered are algae a, bacteria x, protozoa p, inert particulate carbon c_{p}, dissolved organic carbon c_{d} and dissolved phosphorus p_{s}.

Additionally, the biomass B_{S} in the SD region is assumed to grow linearly according to

$$B_{\mathrm{S}}(t) = B_{\mathrm{S}}(0) + A_{\mathrm{in}}t$$

and its effect on the microbial growth in the filter bed are modelled by modifying the reaction terms on the first 2 centimetres of the sandbed. For example, the bacterial reaction terms are given by

$$R_x = k_{\mathrm{gb}}x - k_{\mathrm{d}}x - k_{\mathrm{r}}x - \frac{k_{\mathrm{gmaxp}}}{Y_{\mathrm{p}}}\left(\frac{x}{k_{\mathrm{sb}} + x}\right)p$$

where k_{d}, k_{r}, k_{gmaxp}, Y_{p}, k_{sb} are positive constants and k_{gb} is a function of the concentration of dissolved carbon, 30% of the Schmutzdecke biomass (assumed to be the available carbon to the rest of the filter) and dissolved phosphorus given by

$$k_{\mathrm{gb}} := \frac{k_{\mathrm{gmaxb}}}{41}\left[(40 - 38\chi_{\mathcal{S}})\left(\frac{c_{\mathrm{d}}}{k_{\mathrm{scd}} + c_{\mathrm{d}}}\right) + 38\chi_{\mathrm{S}}\left(\frac{0.3B(t)}{k_{\mathrm{scd}} + 0.3B(t)}\right) + \frac{p_{\mathrm{s}}}{k_{\mathrm{sp}} + p_{\mathrm{s}}}\right]$$

where k_{gmaxb}, k_{scd} and k_{sp} are positive constants, and $\chi_{\mathcal{S}}$ is the indicator function of the set $\mathcal{S} := [T_{\mathrm{lag}}, +\infty) \times [0, 0.02]$, modelling the effect of the Schmutzdecke over the sandbed only in the first 2 centimetres of sand and after the first layer grows.

Headloss is obtained as in the second choice of headloss function in SSF-O.

Numerical method

A finite-difference scheme, written in Visual Basic, in both time and space is used to solve the governing equations.

3.3.3 The model by Langenbach et al. (2010)

This model was presented in [Langenbach et al., 2010]. A summary schematic of this model can be found in Figure 3.5.

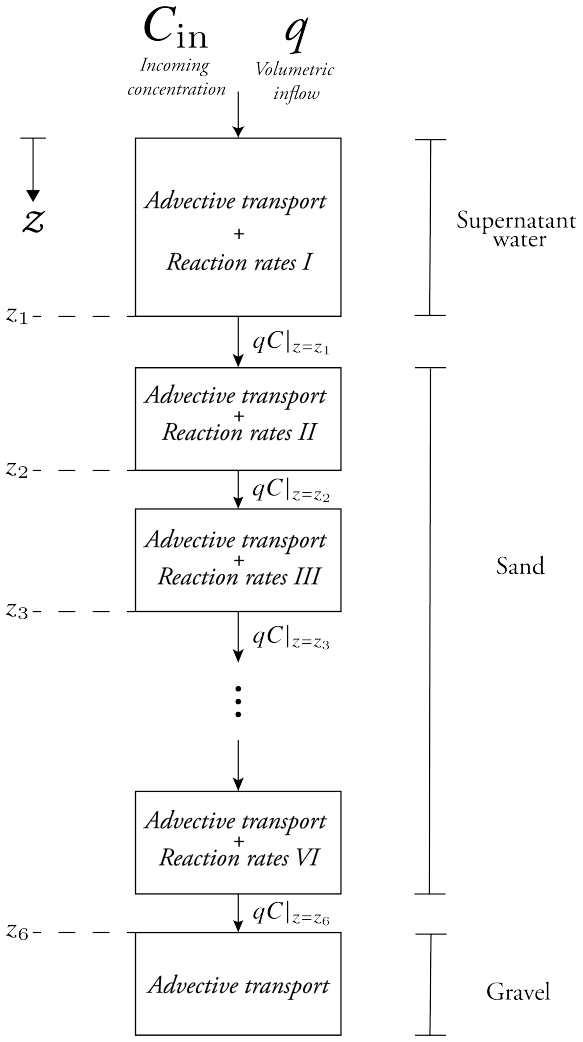

Figure 3.5: Summary schematic of the model by Langenbach et al. [2010]. Each compartment corresponds to a spatial region in which a constant removal factor is prescribed and they are later subdivided into subintervals with uniform mesh size in order to apply a finite differences scheme.

Geometry

The filter is divided into four compartments: supernatant water (1), Schmutzdecke (2), sand bend, further divided into four more compartments $(3, \ldots, 6)$ and gravel (7). Each corresponds to a one-dimensional domain coupled to contiguous compartments by continuity of an advective flux.

Governing equations

The model considers only one state variable, the concentration C_{EC} of *Escherichia Coli* in the bulk. For each compartment, a removal factor f_i is defined as:

$$\begin{aligned} f_1 &= 1, \\ f_2 &= 1 + f^{\mathrm{SD}}, \\ f_j &= 1 + A_{\mathrm{s}} f_j^{\mathrm{SB}}, \qquad j = 3, \ldots, 6 \\ f_7 &= 0, \end{aligned}$$

where f^{SD},f_j^{SB}, are positive constants representing the retention rate to the medium and A_{s} is the specific sand surface area. Putting everything together, one can obtain a space-dependent removal factor $F = F(z)$ given by

$$F(z) := \sum_{i=1}^{7} \chi_i(z) f_i,$$

where χ_i is the indicator function for compartment i.

Finally, the governing equation for the concentration of *E. coli* is

$$\frac{\partial C_{\mathrm{EC}}}{\partial t} + q \frac{\partial C_{\mathrm{EC}}}{\partial z} = -k_{\mathrm{EC}} F(z) C_{\mathrm{EC}},$$

where q is the vertical advection velocity, k_{EC} is a positive constant representing the reaction rate of *E. coli* inactivation, grouping together all removal mechanisms.

Numerical method

The equations are solved using AQUASIM [Reichert, 1998], a software written in C++ implementing conservative finite differences with flux limiters [LeVeque, 2002] for the space discretization and an Euler step in time.

3.3.4 The model by Schijven et al. (2013)

This model was presented in [Schijven et al., 2013] and utilized in several subsequent papers of that group. It is an application of the two-site adsorption model [Mansell and Selim, 1981, Selim et al., 1987, Van Genuchten and Wagenet, 1989]. A summary schematic of this model can be found in Figure 3.6.

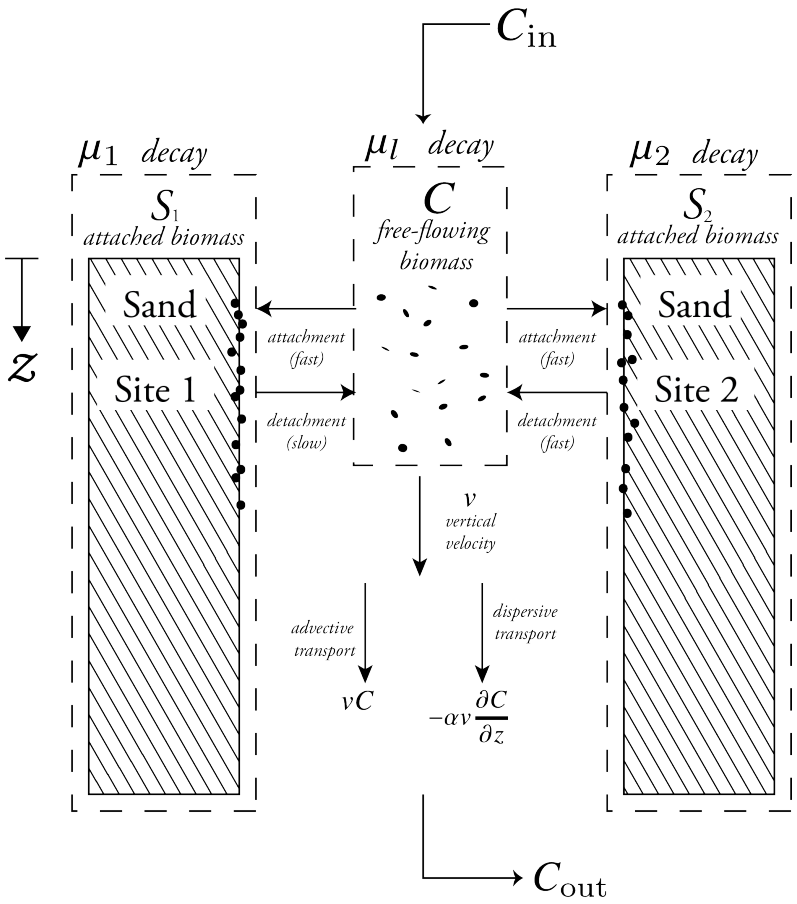

Figure 3.6: Summary schematic of the model by Schijven et al. [2013]. The spatial domain corresponds to a one-dimensional interval with length equal to the sand column height.

Geometry

In this model, only the sand bed is considered in the model.

Governing equations

The concentration of microorganisms in the filter is divided into three phases: free microorganisms with concentration $C = C(t,z)$ and attached microorganisms to kinetic sites 1 and 2 with concentrations $S_1 = S_1(t,z)$ and $S_2 = S_2(t,z)$, respectively.

The linear governing balance equations are

$$\begin{aligned}
\frac{\partial C}{\partial t} + q\frac{\partial C}{\partial x} - \alpha_{\mathrm{L}} q \frac{\partial^2 C}{\partial x^2} &= -\mu_1 C - k_{\mathrm{att},1} C - k_{\mathrm{att},2} C + k_{\mathrm{det},1} S_1 + k_{\mathrm{det},2} S_2 \\
\frac{\partial S_1}{\partial t} &= k_{\mathrm{att},1} C - k_{\mathrm{det},1} S_1 - \mu_{\mathrm{s},1} S_1 \\
\frac{\partial S_2}{\partial t} &= k_{\mathrm{att},2} C - k_{\mathrm{det},2} S_2 - \mu_{\mathrm{s},2} S_2
\end{aligned}$$

After having calibrated $k_{\mathrm{att},i}, k_{\mathrm{det},i}, \mu_1, \mu_{\mathrm{s},i}$ to laboratory experiments, the stationary so-called log removal is of interest. To account for the age of the Schmutzdecke, define fitting parameters f_0, f_1 and suggest the following expression:

$$\log \frac{C_L}{C_0} = -\frac{3}{2}\frac{1-n}{d_{\mathrm{c}}}\left(\alpha\eta L + f_0 T(1 - e^{-\alpha f_1 a})\right),$$

where $n, d_{\mathrm{c}}, \eta, \alpha$ are positive parameters related to the removal efficiency of the sand grains, C_0, C_L are the influent and steady-state effluent concentrations, and a is the age of the Schmutzdecke.

Numerical method

Simulations are carried out using Hydrus-1D [Šimůnek et al., 2008], a software package written in Fortran implementing linear finite elements [Ciarlet, 2002].

3.3.5 Summary of the previous models in literature

A comparison of all the models previously reviewed can be found in Table 3.3, where we have labelled each model SSF-O, SSF-C, SSF-L and SSF-S, after the initial of the first author of each article. We observe that most models for slow sand filtration lack the modelling of detachment mechanisms and the possibility of microbial dynamics happening in the deposited (attached) biological material with the exception of the SSF-S model. However, this model only considers the sandbed and does not take into account biofilm formation, as well as only including inactivation in the reaction terms.

Table 3.3: Comparison table

Model	SSF-O	SSF-C	SSF-L	SSF-S
Supernatant water	✓	✓	✓	✗
Biofilm filtration	✗	As media	As media	Logistic function
Biofilm growth	✗	Fixed growth	✗	✗
Dispersion	✗	✗	✗	✓
Attachment	✓	✓	✗	✓
Detachment	✗	✗	✗	✓
Free microbial dynamics	✗	✓	✓	✓
Attached microbial dynamics	✗	✗	✗	✓
Biofilm pores	✗	✗	✗	✗

It is for these reasons we conclude that there exists no comprehensive model for slow sand filtration that incorporates explicit modelling of detachment mechanisms, microbial dynamics in the whole of the filter and, most importantly, growth of the biofilm as an output of the model (e.g. as accumulation of attached material and growth therein) instead of a fixed functional form. This motivates the introduction of the multi-phase continuum model in one- and two-dimensional form which will be reviewed in Chapter 4.

Chapter 4

A multi-phase continuum model for slow sand filtration

For a short review of the concepts of continuum mechanics utilized in this section, we refer the reader to Section 2.1 of Chapter 2.

4.1 Derivation of the model equations in the general setting

We consider a mixture in the filter of N_P particulate components with concentrations $\boldsymbol{c} = (c^{(1)}, \dots, c^{(N_P)})$ and $N_L + 1$ liquid components (e.g. dissolved chemicals) with concentrations $\boldsymbol{s} = (s^{(1)}, \dots, s^{(N_L)}, s^{(N_L+1)})$ with the last component representing water. We can define the total density of the mixture as (cf. Equation (2.30))

$$\rho = \sum_{i=1}^{N_P} c^{(i)} + \sum_{j=1}^{N_L} s^{(j)}. \tag{4.1}$$

The conservation of mass for each component reads

$$\frac{\partial}{\partial t} c^{(i)} + \nabla \cdot (\boldsymbol{v}_c^{(i)} c^{(i)}) = R_c^{(i)}(\boldsymbol{c}, \boldsymbol{s}), \tag{4.2a}$$

$$\frac{\partial}{\partial t} s^{(j)} + \nabla \cdot (\boldsymbol{v}_s^{(j)} s^{(j)}) = R_s^{(j)}(\boldsymbol{c}, \boldsymbol{s}). \tag{4.2b}$$

We make the following simplifying assumptions:

(A1) The components in the mixture form a closed system for mass-changing reactions. In other words, every material consumed and produced in the change of mass of one component corresponds explicitly to either a particulate or liquid component of the system. Therefore, it holds that

$$\sum_{i=1}^{N_\mathrm{P}} R_c^{(i)}(\boldsymbol{c}, \boldsymbol{s}) + \sum_{j=1}^{N_\mathrm{L}} R_s^{(j)}(\boldsymbol{c}, \boldsymbol{s}) = 0.$$

(A2) All components of the same type have the same density, and it is equal to a constant value, i.e. $\rho_\mathrm{P}^{(i)} = \rho_\mathrm{P}$, $\rho_\mathrm{L}^{(j)} = \rho_\mathrm{L}$.

(A3) Each particulate component corresponds to a single species (biological or chemical) which can be located in either of the three following volumes:

- the biofilm matrix itself,
- the enclosed suspension in the pores of the biofilm matrix,
- the flowing suspension outside the biofilm matrix.

A liquid component, on the other hand, can only be present in one of the two latter volumes.

Assumption (A3) motivates the introduction of the five *main phases* of the model (see Figure 4.1):

- M: particles forming the biofilm matrix,
- Pe: particles in the enclosed suspension of the biofilm pores,
- Pf: particles in the flowing suspension across sand grain pores and biofilm channels,
- Le: liquids in the enclosed suspension of the biofilm pores,
- Lf: liquids in the flowing suspension across sand grain pores and biofilm channels,

after which we relabel our variables in terms of k_P unique particulate species and k_L liquids as

$$C_\gamma^{(i)} \qquad \text{for } i = 1, \dots, k_\gamma,\ \gamma \in \Gamma := \{\mathrm{M}, \mathrm{Pe}, \mathrm{Le}, \mathrm{Pf}, \mathrm{Lf}\},$$

where $k_\gamma = k_\mathrm{P}$ for $\gamma \in \{\mathrm{M}, \mathrm{Pe}, \mathrm{Pf}\}$ and $k_\gamma = k_\mathrm{L}$ for $\gamma \in \{\mathrm{Le}, \mathrm{Lf}\}$. The same is done for individual velocitites $\boldsymbol{v}_\gamma^{(i)}$ and mass-changing reaction terms $R_\gamma^{(i)}$.

Remark. The total number of particulate and liquid components is therefore given by

$$N_\mathrm{P} = 3k_\mathrm{P}, \qquad N_\mathrm{L} = 2k_\mathrm{L}.$$

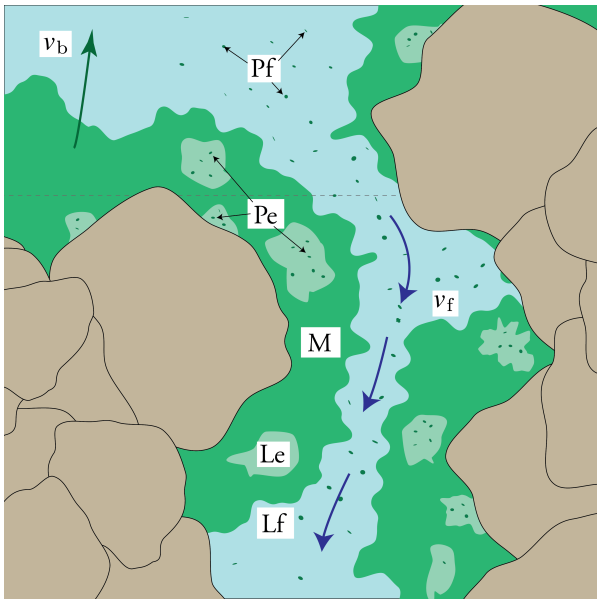

Figure 4.1: Main phases of the multi-phase model and super-phase velocities $\boldsymbol{v}_b$ and $\boldsymbol{v}_f$. Particles and liquids are free to *flow* around the biofilm through the so-called biofilm channels, whereas the *pores* of the biofilm form an *enclosed suspension* that is stationary relative to the movement of the biofilm.

Each main phase is a mixture in itself, defining, for $\gamma \in \Gamma$, densities ρ_γ, volume fractions ϕ_γ and mass-(or volume-)averaged velocities $\boldsymbol{v}_\gamma$ and mass-changing reaction terms R_γ; see Section 2.3 of Chapter 2.

We can group further the main phases into two *super-phases*: the entire biofilm (b), consisting of all components belonging to $\gamma \in \{\mathrm{M}, \mathrm{Pe}, \mathrm{Le}\}$ and the flowing suspension (f), comprised of the remaining components in $\gamma \in \{\mathrm{Pf}, \mathrm{Lf}\}$, and make the following postulates

(A4) The velocities of components in the biofilm matrix and enclosed by the biofilm pores are functions of the volume-averaged velocity $\boldsymbol{q}$ of the entire mixture and of the volume-averaged velocity $\boldsymbol{v}_b$ of the biofilm

(A5) The velocities of components in the flowing suspension are subject to dispersion effects, so that

$$\boldsymbol{v}_\gamma^{(i)} - \boldsymbol{v}_f = \mathcal{D}_\gamma^{(i)}$$

where $\boldsymbol{v}_f$ is the volume-averaged velocity of the flowing suspension and $\mathcal{D}_\gamma^{(i)} = \mathcal{D}_\gamma^{(i)}(\boldsymbol{C}, \nabla \boldsymbol{C})$ is a dispersion term to be defined later.

The balance laws for all components yield:

$$\frac{\partial}{\partial t} C_\gamma^{(i)} + \nabla \cdot (\boldsymbol{v}_\gamma^{(i)} C_\gamma^{(i)}) = R_\gamma^{(i)}(\boldsymbol{C}) \tag{4.3a}$$

$$\frac{\partial}{\partial t} \phi_\mathrm{b}^{(i)} + \nabla \cdot (\boldsymbol{v}_\mathrm{b} \phi_\mathrm{b}) = \sum_{\gamma \in \{\mathrm{M},\mathrm{Pe},\mathrm{Le}\}} \frac{R_\gamma^{(i)}(\boldsymbol{C})}{\rho_\gamma^{(i)}} =: \mathcal{R}_\mathrm{b}(\boldsymbol{C}) \tag{4.3b}$$

where $\boldsymbol{v}_\mathrm{b}$ will be given by constitutive assumptions and is closely related to the induced Cahn–Hilliard velocity $\boldsymbol{v}_\mathrm{CH}$ (see Equation (2.45)) and μ is the corresponding chemical potential associated to ϕ_b and the free energy of mixing Ψ given by Klapper and Dockery [2006].

In this manner, we realize the filter (excluding the medium) as a binary mixture of which one component is a biofilm, so using the biofilm volume fraction ϕ_b as the order parameter, we can use Equation (2.42) as the governing system for ϕ_b.

For the volume-averaged velocity $\boldsymbol{q}$, since the volumetric flow in a slow sand filter is quite low, we assume that it satisfies some form of Stokes flow in the supernatant water:

$$-\nabla \cdot \mathbb{S}(\boldsymbol{q}, p) = \boldsymbol{F}_\mathrm{b}(\phi_\mathrm{b}, \mu), \tag{4.4a}$$

$$\nabla \cdot \boldsymbol{q} = 0, \tag{4.4b}$$

where $\boldsymbol{F}_\mathrm{b}(\phi_\mathrm{b}, \mu)$ is a term related to the forces associated to the biofilm, such as gravitational forces due to density differences and viscoelastic stresses. Equations for the behaviour of $\boldsymbol{q}$ in the medium are, however, dependent on the dimension of the model and will be discussed later.

We make the following assumptions regarding the reaction terms $R_\gamma^{(i)}$:

(A6) Each mass-changing reaction term can be decomposed as

$$R_\gamma^{(i)} = R_{\mathrm{att},\gamma}^{(i)} + R_{\mathrm{det},\gamma}^{(i)}(\boldsymbol{v}_\mathrm{f}) + R_{\mathrm{tr},\gamma}^{(i)} + R_{\mathrm{eco},\gamma}^{(i)}, \quad \gamma \in \Gamma, \tag{4.5}$$

where

- $R_{\mathrm{att},\gamma}^{(i)}$ is a term corresponding to the mass influx due to attachment of material from a different phase ($\mathrm{Pe} \to \mathrm{M}$ or $\mathrm{Pf} \to \mathrm{M}$),
- $R_{\mathrm{det},\gamma}^{(i)}(\boldsymbol{v}_\mathrm{f})$ is the mass exchange due to detachment of material from the biofilm matrix ($\mathrm{M} \to \mathrm{Pf}$),
- $R_{\mathrm{tr},\gamma}^{(i)}$ is the inter-membrane transport of dissolved material across the biofilm due to concentration gradients ($\mathrm{Pe} \leftrightarrow \mathrm{Pf}$ or $\mathrm{Le} \leftrightarrow \mathrm{Lf}$),

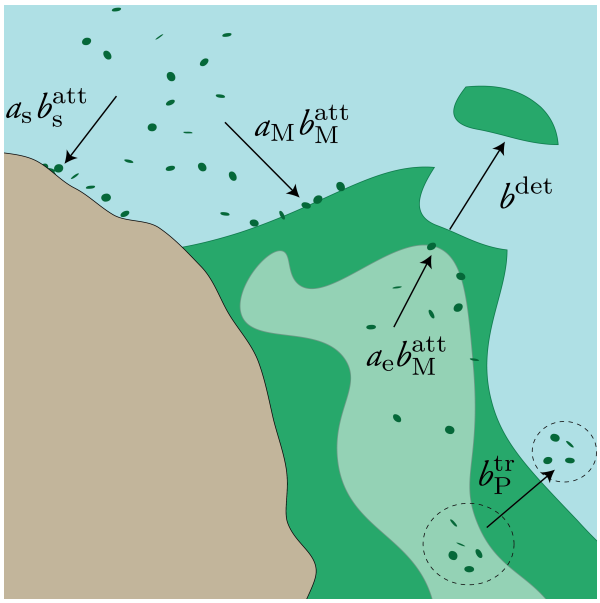

Figure 4.2: Diagram of physical mass-changing interactions in the multi-phase model: attachment (att) both from the flowing (f) and enclosed (e) suspensions, inter-membrane transport (tr) and detachment (det).

- and $R_{\mathrm{eco},\gamma}^{(i)}$ is the term corresponding to microbial dynamics such as growth, inactivation, hydrolysis, etc.

The precise form of each of these terms is dependent on the spatial dimension of the model and so they will be discussed further in Sections 4.2 and 4.3. A diagram of these reactions and how they exchange mass between phases is given in Figure 4.2

4.2 One-dimensional model

This corresponds to the model presented in Papers I and II. The interested reader is referred to these works for a more in-depth discussion and derivation of the model, as only a brief summary of it will be presented in this section.

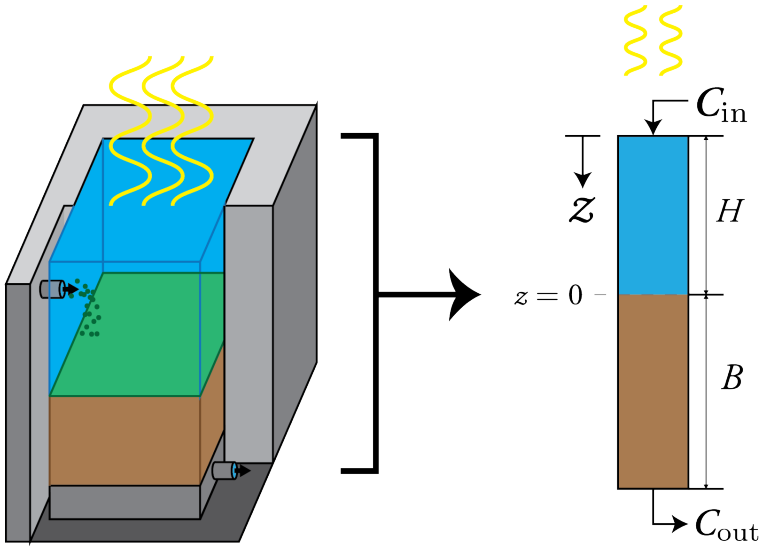

Figure 4.3: One-dimensional representation of an SSF including both supernatant water and sand bed, omitting the gravel and drainage.

4.2.1 Geometry of the filter

We consider a 1D domain with spatial coordinate z representing the depth in the medium. As such, $z < 0$ corresponds to the supernatant water region and $z \geq 0$ corresponds to the sand bed. The supernatant water has constant height H and the sand has depth B; see Figure 4.3.

Physical quantities will correspond to cross-sectional averages over entire sections of the filter, and we note that the mixture occupies the space outside the sand grains. Consequently, we define the effective cross-sectional area $\mathcal{A} = \mathcal{A}(z)$ given by

$$\mathcal{A}(z) = A\tilde{\varepsilon}(z),$$

where A is the (constant) cross-sectional area in the filter and the effective porosity $\tilde{\varepsilon} = \tilde{\varepsilon}(z)$ given by the continuous function

$$\tilde{\varepsilon}(z) = \begin{cases} 1, & \text{if } z < -\delta, \\ \varepsilon_\delta(z), & \text{if } -\delta \leq z \leq 0, \\ 0, & \text{if } z > 0, \end{cases}$$

where $\varepsilon > 0$ is the porosity in the sand and $\epsilon_\delta(z)$ is a decreasing function. The depth δ is a measure of the roughness of the sand surface. This latter intermediate porosity represents

the region of the medium where both attachment to the sand grains and biofilm movement is permitted, in contrast to the packed sand region ($z > 0$) where the biofilm velocity is prescribed to be equal to zero. For simplicity, ε_δ is taken as a linear function of z.

Given an incoming velocity $q_{\text{in}} = q_{\text{in}}(t)$ at the inflow of the filter, as volume-changing effects are neglected and the mixture undergoes incompressible flow by Equation (4.4b), we have at any point z

$$\mathcal{A}(z)q(t,z) - Aq_{\text{in}}(t) = \int_{-H}^{z} \mathcal{A}(z)\frac{\partial}{\partial s}q(t,s)\mathrm{d}s = 0$$

and the bulk velocity in the filter $q = q(z,t)$ is thus defined as

$$q(t,z) = \frac{q_{\text{in}}(t)}{\tilde{\varepsilon}(z)}. \tag{4.6}$$

4.2.2 Governing equations

If we take the cross-sectional average of Equation (4.3), we arrive at the following set of equations only dependent on the depth z and time t:

$$\frac{\partial}{\partial t}C_\gamma^{(i)} + \frac{\partial}{\partial z}(v_\gamma^{(i)}C_\gamma^{(i)}) = R_\gamma^{(i)}(\boldsymbol{C}) \tag{4.7a}$$

$$\frac{\partial}{\partial t}\phi_{\text{b}} + \frac{\partial}{\partial z}(v_{\text{b}}\phi_{\text{b}}) = \mathcal{R}_{\text{b}}(\boldsymbol{C}). \tag{4.7b}$$

Constitutive assumptions on the velocities

We assume that the vertical velocities of all phases $\gamma \in \{\text{M}, \text{Pe}, \text{Le}\}$ are equal to the biofilm velocity v_{b} and this is, in turn, given by the Cahn–Hilliard velocity in the supernatant water and zero in the sand, i.e.

$$v_\gamma^{(i)} = v_{\text{b}} = \begin{cases} q - (1-\phi_{\text{b}})\frac{\partial}{\partial z}\left(-\kappa\frac{\partial^2}{\partial z^2}\phi_{\text{b}} + \Psi'(\phi_{\text{b}})\right), & \text{if } z < 0, \\ 0, & \text{if } z > 0, \end{cases} \qquad i = 1, \dots, k_\gamma \tag{4.8}$$

for all $\gamma \in \{\text{M}, \text{Pe}, \text{Le}\}$.

Remark. Note that v_{b} presents a discontinuity at $z = 0$, which poses the mass conservation of the biofilm phase as a conservation law with spatially discontinuous flux [Diehl, 1995]. In order to avoid dealing with the ill-defined flux at this point, the numerical method will incorporate a cell that contains this discontinuity in its interior as in [Bürger et al., 2017]

The volume-averaged velocities v_b and v_f are related by

$$q = \phi_\mathrm{b} v_\mathrm{b} + \phi_\mathrm{f} v_\mathrm{f},$$

which can be rewritten as

$$v_\mathrm{f} = \frac{q - \phi_\mathrm{b} v_\mathrm{b}}{1 - \phi_\mathrm{b}}, \tag{4.9}$$

using the fact that $\phi_\mathrm{b} + \phi_\mathrm{f} = 1$.

For the flowing suspension, we assume that flowing components undergo hydrodynamic dispersion such that

$$\left(v_\gamma^{(i)} - v_\mathrm{f}\right) \frac{C_\gamma^{(i)}}{\phi_\mathrm{f}} = -\alpha_\gamma^{(i)} |v_\mathrm{f}| \frac{\partial}{\partial z} \left(\frac{C_\gamma^{(i)}}{\phi_\mathrm{f}} \right), \quad C_\gamma^{(i)} \neq 0, \quad \gamma \in \{\mathrm{Pf}, \mathrm{Lf}\}, \tag{4.10}$$

where $\alpha_\gamma^{(i)}$ is the dispersion coefficient of each component. The ratio $\phi_\mathrm{f}^{-1} C_\gamma^{(i)}$ is interpreted as the *local* concentration of each component in the flowing suspension.

In conclusion, all velocities can be determined as functions of

- the concentrations $C_\gamma^{(i)}$,
- the biofilm volume fraction $\phi_\mathrm{b} = \phi_\mathrm{b}(z, t)$
- and the bulk velocity $q = q(t, z)$.

Since the bulk velocity is a function of the velocity at the influx and the filter porosity, it can be counted as a known datum and we can conclude that Equations (4.7a) and (4.7b) form a closed system.

Constitutive assumptions on the reaction terms

We have split the mass-changing reaction terms into three categories:

- attachment/detachment, for which we introduce $a_\mathrm{s} = a_\mathrm{s}(\tilde{\varepsilon})$, $a_\mathrm{f} = a_\mathrm{f}(\phi_\mathrm{b}, \tilde{\varepsilon})$, $a_\mathrm{e} = a_\mathrm{e}(\phi_\mathrm{b}, \phi_\mathrm{M})$ and $b_\mathrm{det}(v_\mathrm{f})$ such that
  - the likelihood of attachment from flowing suspension factor to sand grain a_s is

$$a_\mathrm{s}(\phi_\mathrm{b}, \tilde{\varepsilon}) = 1 - \tilde{\varepsilon}$$

– the likelihood of attachment from flowing suspension to biofilm matrix factor a_{M} is

$$a_{\mathrm{M}}(\phi_{\mathrm{b}}, \tilde{\varepsilon}) = \tilde{\varepsilon}\phi_{\mathrm{b}}$$

– the likelihood of attachment from enclosed suspension factor a_{e} is

$$a_{\mathrm{e}}(\phi_{\mathrm{b}}, \phi_{\mathrm{M}}) = \frac{\phi_{\mathrm{M}}}{\phi_{\mathrm{b}}}$$

– the detachment rate $b_{\mathrm{det}}(v_{\mathrm{f}})$ is a non-decreasing function of the flowing suspension velocity magnitude; for example,

$$b_{\mathrm{det}}(v_{\mathrm{f}}) = b_{\mathrm{det,nom}}\sqrt{\frac{|v_{\mathrm{f}}|}{q_{\mathrm{nom}}}}$$

satisfies this assumption, with q_{nom} a nominal velocity for which a nominal detachment rate $b_{\mathrm{det,nom}}$ was measured.

With these, we define

$$R^{(i)}_{\mathrm{att},\gamma} = 0, \qquad \gamma \in \{\mathrm{M}, \mathrm{Le}, \mathrm{Lf}\}, \tag{4.11a}$$

$$R^{(i)}_{\mathrm{att,Pe}} = (b^{(i)}_{\mathrm{att,s}} a_{\mathrm{s}} + b^{(i)}_{\mathrm{att,M}} a_{\mathrm{M}}) C^{(i)}_{\mathrm{Pe}}, \tag{4.11b}$$

$$R^{(i)}_{\mathrm{att,Pf}} = b^{(i)}_{\mathrm{att,M}} a_{\mathrm{e}} C^{(i)}_{\mathrm{Pf}}, \tag{4.11c}$$

$$R^{(i)}_{\mathrm{det},\gamma} = 0, \qquad \gamma \in \{\mathrm{Pe}, \mathrm{Le}, \mathrm{Pf}, \mathrm{Lf}\}, \tag{4.11d}$$

$$R^{(i)}_{\mathrm{det,M}} = b_{\mathrm{det}}(v_{\mathrm{f}}) C^{(i)}_{\mathrm{M}}, \tag{4.11e}$$

where we note that a_{f} and a_{e} are likelihood of attachment *factors* and not rates since each material component is assumed to attach at its own respective rates $b^{(i)}_{\mathrm{att,s}}$ and $b^{(i)}_{\mathrm{att,M}}$. This is not true for biomass detachment as detachment of multicellular clumps has been experimentally found to be more significant than erosion of single cells [Wang and Zhang, 2010, Fux et al., 2004], and so we postulate that the biomass detachment happens as homogeneous clumps.

- inter-membrane transport, modelled with a discrete diffusion term in terms of *local concentration* differences, is given by

$$R^{(i)}_{\mathrm{M}} = 0, \tag{4.12a}$$

$$R^{(i)}_{\mathrm{tr,Pe}} = -R^{(i)}_{\mathrm{tr,Pf}} = b^{(i)}_{\mathrm{tr,P}} \beta^{-1} \phi_{\mathrm{e}} (\phi_{\mathrm{e}}^{-1} C^{(i)}_{\mathrm{Pe}} - \phi_{\mathrm{f}}^{-1} C^{(i)}_{\mathrm{Pf}}), \tag{4.12b}$$

$$R^{(i)}_{\mathrm{tr,Le}} = -R^{(i)}_{\mathrm{tr,Lf}} = b^{(i)}_{\mathrm{tr,L}} \beta^{-1} \phi_{\mathrm{e}} (\phi_{\mathrm{e}}^{-1} C^{(i)}_{\mathrm{Le}} - \phi_{\mathrm{f}}^{-1} C^{(i)}_{\mathrm{Lf}}). \tag{4.12c}$$

where β is the steady-state porosity of the biofilm, estimated by measuring dry and wet weights of samples. In this case, $\beta^{-1}\phi_{\mathrm{e}}$ acts as an approximation of the entire biofilm volume ϕ_{b} that is independent of ϕ_{M}.

- ecological, for which we consider a collection of processes $r_1, \ldots, r_p$ dependent on particle and liquid concentrations, temperature and possibly light irradiation, along with stoichiometric matrices $\sigma_{\mathrm{P}} \in \mathbb{R}^{k_{\mathrm{P}} \times p}, \sigma_{\mathrm{L}} \in \mathbb{R}^{k_{\mathrm{L}} \times p}$ such that $(\sigma_{\mathrm{P}})_{kj}$ (resp. $(\sigma_{\mathrm{L}})_{kj}$) corresponds to the stoichiometrically balanced amount of particulate (resp. liquid) component k in reaction j.

  Remark. We have that the matrix $\sigma = \begin{pmatrix} \sigma_{\mathrm{P}} \\ \sigma_{\mathrm{L}} \end{pmatrix}$ is a stoichiometric matrix in the sense that $(\mathbf{1}_{k_{\mathrm{P}}+k_{\mathrm{L}}})^{\intercal} \sigma = 0$, ensuring mass conservation.

  Before defining the ecological reaction terms, we make one additional assumption:

  (A7) Reactions can happen in three ecological loci within the filter, roughly corresponding to the three volumes of Assumption (A3), in which a particulate phase interacts (containing, for example, a microbe) with a corresponding liquid phase (containing a nutrient). Moreover, reactions are dependent on the *local* concentration of particles and liquids, i.e. the concentration of components with respect to the volume of the respective locus. The ecological loci with their respective local concentrations are:

  – the *biofilm locus* (b), in which the particles in the matrix (M) interact with stored nutrients in the pores (Le), with

  $$X_{\mathrm{b}}^{(i)} = \phi_{\mathrm{b}}^{-1} C_{\mathrm{M}}^{(i)},$$
  $$S_{\mathrm{b}}^{(i)} = \phi_{\mathrm{b}}^{-1} C_{\mathrm{Le}}^{(i)}.$$

  – the *enclosed locus* (e), in which the enclosed particles (Pe) interact with surrounding liquids (Le), with

  $$X_{\mathrm{e}}^{(i)} = \phi_{\mathrm{e}}^{-1} C_{\mathrm{Pe}}^{(i)},$$
  $$S_{\mathrm{e}}^{(i)} = \phi_{\mathrm{e}}^{-1} C_{\mathrm{Le}}^{(i)}.$$

  – the *flowing locus* (f), in which the flowing particles in (Pf) interact with surrounding liquids (Lf), with

  $$X_{\mathrm{f}}^{(i)} = \phi_{\mathrm{f}}^{-1} C_{\mathrm{Pf}}^{(i)},$$
  $$S_{\mathrm{f}}^{(i)} = \phi_{\mathrm{f}}^{-1} C_{\mathrm{Lf}}^{(i)}.$$

  Remark. In terms of the local concentrations $\boldsymbol{X}$ and $\boldsymbol{S}$, we can rewrite Equation (4.10)

and Equations (4.12b) and (4.12c) as

$$
\begin{aligned}
v_{\mathrm{Pf}}^{(i)} - v_{\mathrm{f}} &= -\alpha_{\mathrm{P}}^{(i)} |v_{\mathrm{f}}| \frac{\partial}{\partial z} \log X_{\mathrm{f}}^{(i)} \\
v_{\mathrm{Lf}}^{(i)} - v_{\mathrm{f}} &= -\alpha_{\mathrm{L}}^{(i)} |v_{\mathrm{f}}| \frac{\partial}{\partial z} \log S_{\mathrm{f}}^{(i)} \\
R_{\mathrm{tr,Pe}}^{(i)} = -R_{\mathrm{tr,Pf}}^{(i)} &= b_{\mathrm{tr,P}}^{(i)} \beta^{-1} \phi_{\mathrm{e}} (X_{\mathrm{e}}^{(i)} - X_{\mathrm{f}}^{(i)}), \\
R_{\mathrm{tr,Le}}^{(i)} = -R_{\mathrm{tr,Lf}}^{(i)} &= b_{\mathrm{tr,L}}^{(i)} \beta^{-1} \phi_{\mathrm{e}} (S_{\mathrm{e}}^{(i)} - S_{\mathrm{f}}^{(i)}).
\end{aligned}
$$

As such, we define reaction vectors

$$
\boldsymbol{r}_\star = \mu_\star \boldsymbol{r}(\boldsymbol{X}_\star, \boldsymbol{S}_\star, T, I), \qquad \star \in \{\mathrm{b}, \mathrm{e}, \mathrm{f}\},
$$

where T is the temperature in the filter and $I = I(t, z)$ is the light irradiation (see Paper I for its definition), μ_{b}, μ_{e} and μ_{f} are dimensionless efficiency parameters, modelling how some ecological interactions might happen at a lower or higher rate depending on the interaction locus (e.g. predation might be more efficient in the biofilm matrix than in the flowing suspension), and define

$$
\begin{aligned}
R_{\mathrm{M}}^{(i)} &= [\sigma_{\mathrm{P}} \phi_{\mathrm{b}} \boldsymbol{r}_{\mathrm{b}}]_i, \\
R_{\mathrm{Pe}}^{(i)} &= [\sigma_{\mathrm{P}} \phi_{\mathrm{e}} \boldsymbol{r}_{\mathrm{e}}]_i, & R_{\mathrm{Le}}^{(i)} &= [\sigma_{\mathrm{L}} (\phi_{\mathrm{b}} \boldsymbol{r}_{\mathrm{b}} + \phi_{\mathrm{e}} \boldsymbol{r}_{\mathrm{e}})]_i, \\
R_{\mathrm{Pf}}^{(i)} &= [\sigma_{\mathrm{P}} \phi_{\mathrm{f}} \boldsymbol{r}_{\mathrm{f}}]_i, & R_{\mathrm{Lf}}^{(i)} &= [\sigma_{\mathrm{L}} \phi_{\mathrm{f}} \boldsymbol{r}_{\mathrm{f}}]_i.
\end{aligned}
$$

The set of processes considered for these reactions is referred to as *the ecological submodel* and there exists freedom in choosing such a submodel. In Paper I a simplified ecological model is introduced with $\mu_{\mathrm{b}} = \mu_{\mathrm{e}} = \mu_{\mathrm{f}} = 1$ and later expanded in Paper II, incorporating an indicator species for measuring water quality. A diagram of this submodel is given in Figure 4.4.

4.2.3 Numerical method

The inputs of the simulation software are the volumetric flow and concentrations at the inlet, as well as incoming light irradiation and temperature. For the numerical simulation, we developed an implicit-explicit finite differences scheme to solve Equation (4.7b) and compute v_{b} according to Equation (4.8). Then, we solve Equation (4.7a) using upwind finite differences and choose a time step such that the positivity-preserving CFL condition is fulfilled. Further details can be found in Paper I.

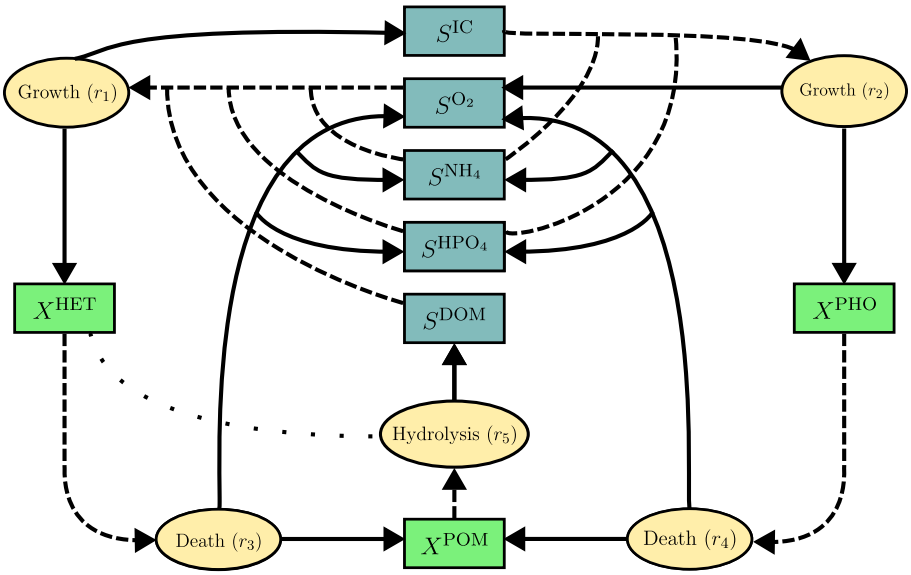

Figure 4.4: The simplified ecological model of slow sand filtration in Paper I.

Results of a simulation can be seen in Figure 4.5. As expected, the highest concentration of pathogen is located at the very top of the biofilm and it drops significantly after the first few centimeters. This is the filtering behaviour of the Schmutzdecke.

In Paper II, the numerical method was modified by replacing the Dirichlet boundary condition on ϕ_{b} used in the computation of v_{b}, for a null Neumann boundary condition. This lead to a biofilm profile with a discontinuity at $z = 0$, but increased the stability of the scheme and relaxed the restriction on the time-step sizes, from the order of 10^{-9} to 10^{-7}.

While the details are not present in Paper II, this change amounts to replacing the matrix $\mathbb{D}$ in Paper I, p. 19

$$\begin{pmatrix} 2 & -1 & & & \\ -1 & 2 & -1 & & \\ & -1 & \ddots & \ddots & \\ & & \ddots & \ddots & -1 \\ & & & -1 & 2 \end{pmatrix} \quad \text{for} \quad \begin{pmatrix} 1 & -1 & & & \\ -1 & 2 & -1 & & \\ & -1 & \ddots & \ddots & \\ & & \ddots & \ddots & -1 \\ & & & -1 & 1 \end{pmatrix},$$

and the second term in the right-hand side of Paper I, p. 18

$$\underline{(\Psi')^n} + \begin{pmatrix} \underline{0} \\ -\kappa \frac{u_1^{n+1}}{\Delta z} \end{pmatrix} \quad \text{for} \quad \underline{(\Psi')^n}.$$

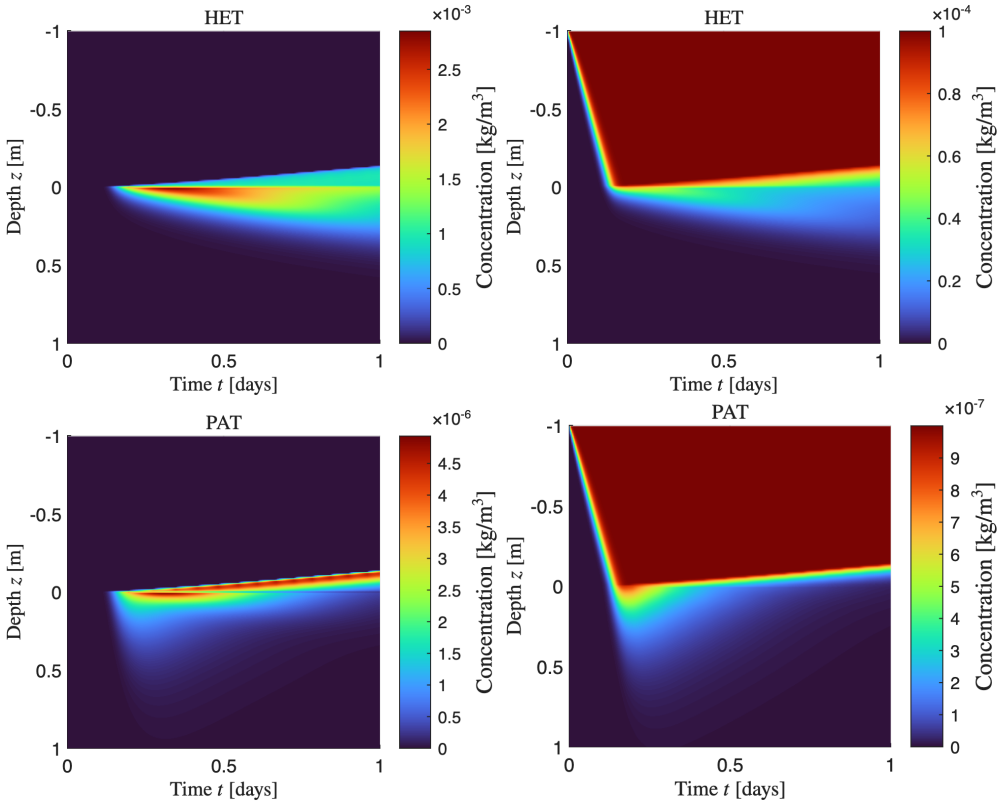

Figure 4.5: Concentration of various components (HET for heterotrophs, PAT for pathogen) in the biofilm matrix (left) and the flowing suspension (right). The biofilm matrix, composed of particulate components, grows upwards over time. In the bottom left figure, one can observe that the top layer absorbs the most amount of pathogen.

4.3 Two-dimensional model

This is the model presented in Paper III.

4.3.1 Geometry of the filter

We consider a 2D representation of the supernatant water in the filter by considering a longitudinal slice with depth coordinate z and transversal coordinate x; see Figure 4.6. We ignore the medium and set $z = 0$ at the inlet.

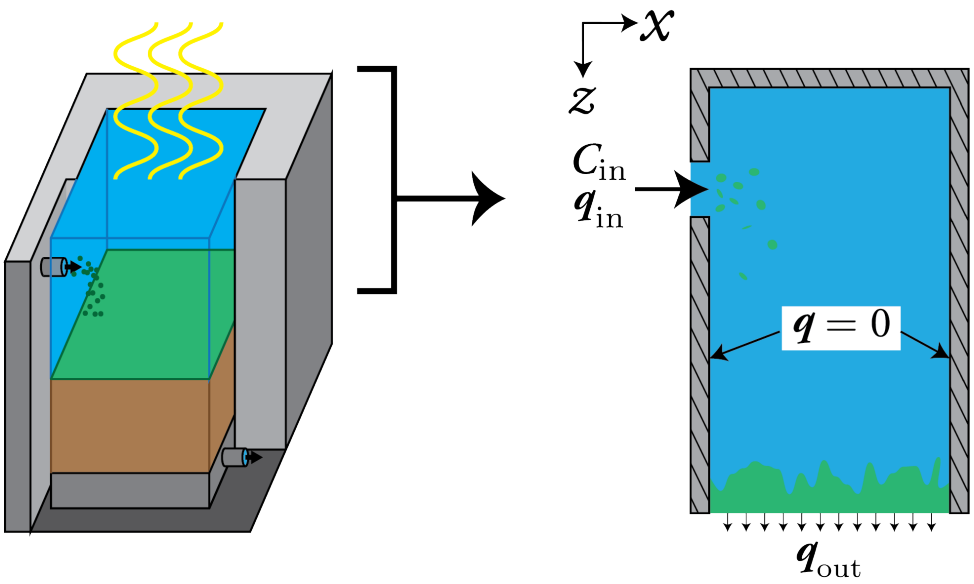

Figure 4.6: Schematic of the supernatant water region in 2D.

4.3.2 Governing equations

By taking the average across the perpendicular direction to the xz-plane in Equations (2.9) and (2.20), we arrive at a 2D re-formulation of Equation (4.7) for the supernatant water, where u is the scalar biofilm concentration (instead of the volume fraction ϕ_b):

$$
\begin{aligned}
-\nabla \cdot (-p\mathbb{I} + \nu(u)\mathbb{E}(\boldsymbol{q})) &= -\hat{g}u\hat{\boldsymbol{z}} + \eta\mu\nabla u \\
\nabla \cdot \boldsymbol{q} &= 0 \\
\frac{\partial}{\partial t}u + \nabla \cdot \left(\left(\boldsymbol{q} - \lambda_0 u(1-\rho_{\mathrm{b}}^{-1}u)\right)u\right) &= R_u(\boldsymbol{c},\boldsymbol{s}) \\
\mu + \rho_{\mathrm{b}}^{-1}\kappa\Delta u - \Psi'(u) &= 0 \\
\frac{\partial}{\partial t}c^{(i)} + \nabla \cdot \left(\left(\boldsymbol{q} - \lambda_0(1-\rho_{\mathrm{b}}^{-1}u)\nabla\mu\right)c^{(i)}\right) &= R_c^{(i)}(\boldsymbol{c},\boldsymbol{s}) \\
\frac{\partial}{\partial t}s^{(i)} + \nabla \cdot \left(\left(\boldsymbol{q} + \lambda_0 u\right)s^{(i)}\right) &= R_s^{(i)}(\boldsymbol{c},\boldsymbol{s})
\end{aligned}
$$

where $\hat{g} \coloneqq g(1-\rho_{\mathrm{b}}^{-1}\rho_{\mathrm{f}})$ with g the acceleration of gravity, $\hat{\boldsymbol{z}}$ is a unit vector in the direction of z and η is a surface tension constant. Here we note that the viscosity ν depends on the biomass concentration.

Note that in this model, we are using the biofilm concentration u instead of the biofilm volume fraction ϕ_{b}, leading to some re-scaling, e.g. the appearance of $\rho_{\mathrm{b}}^{-1}\kappa$ in place of κ.

Remark. In this 2D model, we have omitted dispersion effects and the subdivision of the biomass into the five phases of the 1D model, effectively working with two main phases (particles $\boldsymbol{c}$ and liquids $\boldsymbol{s}$), each still composed of multiple components, omitting the phase-exchange terms of attachment and intermembrane transport. This is, however, just an assumption for simplicity and the development of a toy model.

4.3.3 Numerical method

A finite element method based on the work of Acosta-Soba et al. [2023] is developed to solve the Cahn–Hilliard equation in order to define the fluxes of the convection-reaction system of individual concentrations. The method consists of an upwind DG scheme with a splitting of the numerical flux based on the increasing and decreasing parts of the degenerate mobility in order to preserve positivity. Conforming finite elements are used for the Stokes problem. See further details in Paper III.

A snapshot of a simulation can be seen in Figure 4.7.

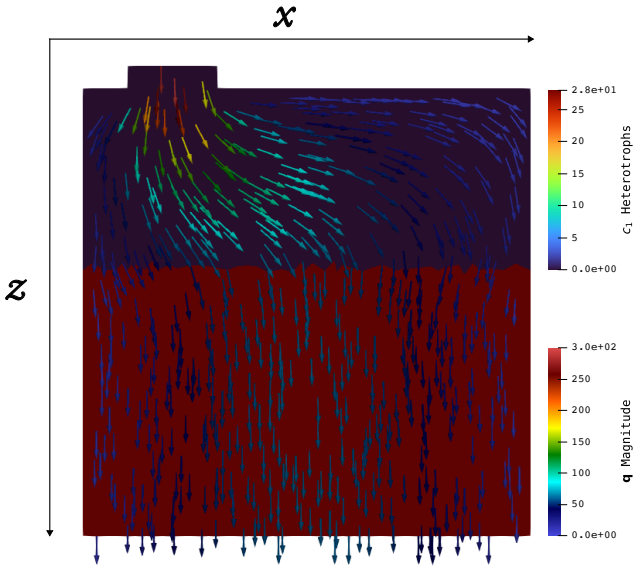

Figure 4.7: Numerical result for the 2D model. The coloring of the domain corresponds to the heterotroph concentration (c_1) and the arrows correspond to the velocity field $\boldsymbol{q}$.

Conclusions

Summary of results

I. A 1D system of non-linear PDEs with spatial discontinuous flux is used to model the evolution of concentrations of microorganisms and nutrients in an SSF, which we call a *unified continuum multiphase framework*. A reduced model of the ecology of the filter is utilized, focusing on biomass evolution inside the filter. This partially answers Research question (i), as the model is derived entirely from mass balances, albeit with some assumptions on the biofilm velocity in the sandbed. A finite-difference scheme, based on a splitting of the biofilm velocity/volume-fraction and the individual global concentrations, is used for simulations. The scheme is positivity-preserving for the individual global concentrations under an explicit CFL condition that depends on the magnitude of the biofilm velocity. This is a partial answer to Research question (ii).

II. The unified continuum multiphase framework is updated and simulations of operational scenarios are presented. In order to answer Research question (iii), the model in Paper I is extended to include an indicator species (a waterborne pathogen, for example) that reflects the water quality and measures the effectivity of the filter.

III. The 1D model is used as a base to develop a 2D model for biomass growth in the supernatant water region. A positivity-preserving DG method is developed for the simulations, posing an improvement on the numerical method for the 1D model as both the biofilm volume fraction and the individual concentrations are positive for all time steps without splitting. This is a step further in the direction of Resarch question (ii). The DG method, previously used for a convective Cahn–Hilliard equation, is modified to be used for the convection-reaction-Cahn–Hilliard model and mass conservation is proven.

Outlook

In this section we present possible directions of future research based on the thesis work.

1. **Measurements and calibration of the model**
   The parameters used in Papers I, II and III are taken from a variety of sources in the literature. It remains to determine methodology for obtaining biomass concentration measurements in an operating filter, as evidence shows that laboratory measurements do not coincide with the microbiological community that exists in large scale filters. Furthermore, this could lead to some reformulation of the model to accommodate the measurements, such as working with surrogate quantities such as bulk densities or ranges of estimated reaction rates.

2. **Estimation of headloss**
   Currently, clogging in the 1D model is assumed to happen at a certain threshold volume fraction of biofilm. However, for measuring and control purposes, it would be useful to consider headloss to estimate the clogging of the filter.

   Headloss is an estimation of the energy loss in fluid flows between two points, measured as the difference in height of two water columns for which their surface pressure is equal to the pressure at each respective point. Darcy's law can be stated in terms of the hydraulic head as $h = h(t, z)$ as

   $$\hat{q} = -K\partial_z h, \tag{4.14}$$

   where $\hat{q} = \hat{q}(t)$ is the volumetric flow in the sand bed and K is the hydraulic conductivity. By integrating Equation (4.14) from 0 to z, we can express the total headloss h_{loss} as

   $$h_{\text{loss}} = \int_z^0 K^{-1}\hat{q}\,\mathrm{d}\xi.$$

   Under the assumptions of our model, by mass conservation we have that $\hat{q}$ is constant in depth. However, experiments show that filters suffer a headloss greater than the height drop between the top of the sandbed and the bottom outlet. This suggests that the hydraulic conductivity depends on the state of the filter, and we theorize that it depends on the biofilm volume fraction ϕ_{b}.

   For example, following a similar approach to Shi et al. [2021], it could be possible to consider a biofilm-dependent porosity $\varepsilon_{\text{b}} := \varepsilon(1 - \phi_{\text{b}})$ and utilize a heuristic estimation of the hydraulic conductivity K such as a Kozeny–Carman-type formula.

3. **Alternative positivity-preserving methods**
   In Papers I and II, the numerical method relies on an assumption of boundedness

on the gradient of the chemical potential $\partial_z \mu$. One then wonders if it is possible to obtain an explicit bound on this gradient, or whether a different method can be devised such that it is positivity-preserving independent of this velocity. In the direction of the latter, one direct option is to adapt the method for the 2D simplified model or another method for (Navier–)Stokes–Cahn–Hilliard equations to the full 1D model. For a survey and comparison of structure-preserving methods for the latter, we refer the reader to [Gunnarsson and Klöfkorn, 2026].

4. **Full extension of the multiphase 1D model to 2D**
   In Paper III, we presented a toy model of a 2D extension of the multiphase model. It remains to fully extend the comprehensive 1D model, together with attachment and intermembrane transport, to 2D.

5. **Stokes/Darcy/Cahn–Hilliard coupling**
   A possible extension of the model to the 2D case is to consider the sand as saturated porous media, for which we know the Darcy equation is a good model for fluid flow. Therefore, we would be looking at a Stokes/Darcy coupling for fluid flow as in Paper V, in which we need to consider friction terms arising from the Cahn–Hilliard equation as in Paper III.

6. **Study of quasi-periodic solutions**
   The numerical results of the 1D model suggest that, except for the growth of biofilm until clogging occurs, the in- and out-flowing concentrations tend to an almost periodic solution because of the light irradiation. It is of interest to obtain mathematical properties of such quasi-periodic solutions (for example, the net increase or decrease of mean oxygen outflow in a filter) to define control strategies for the operation of slow sand filters.

Part II

Solving interface problems with the Transfer Path Method

Chapter 5

Introduction

In other words we want to find out whether or not crime pays; fortunately for the finite element method, it often does.
— Gilbert Strang,
Variational crimes in the finite element method (1972)

In a variety of contexts, problems can be found in which the domain of interest is split into two or more subdomains, leading to corresponding "subproblems" which are then required to be coupled with one another in some capacity. This division can be an actual physical object, such as an ellastic membrane separating two aqueous solutions, or the outline of a region across which material properties are discontinuous. The subproblems are then coupled by appropriate compatibility conditions between subdomains, such as continuity requirements across subdomain divisions or physical balance laws. For a pair of two contiguous but not overlapping subdomains, we use the term *interface* to refer to the shared boundary in which they are in contact, and the term *interface problem* to any such problem where an interface is involved and corresponding compatibility conditions are prescribed on it. The applications of interface problems arising to engineering problems are vast and therefore they constitute a major point of interest for scientific computing. Interface problems are also associated with numerical methods which introduce fictitious subdivisions of a domain for computational purposes, as is the case in non-overlapping domain decomposition methods [Gosselet and Rey, 2006, Engström and Hansen, 2022] and, in a certain way, the hybridizable discontinuous Galerkin method [Cockburn et al., 2009].

In the case that an interface is curved, traditional finite element methods are at risk of commiting a *variational crime* [Strang, 1972] by directly applying them, since common geometrical discretizations consist of straight shapes (polygons in 2D and polyhedra in 3D).

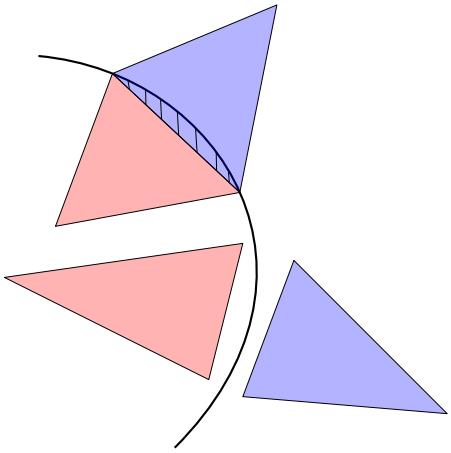

Figure 5.1: Using straight elements to approximate the curved interface (black solid line), we either have an overlap between the computational domain of one subdomain with the exact domain of another (dashed region) or leave gaps between the meshes.

This leads to a mismatch between the discrete and exact subdomains, which means we are solving a surrogate problem on a different geometry. For a close reference of solving surrogate problems, we can look at boundary value problems with *curved boundaries*. In that case, the crime of solving elliptic boundary value problems with curved boundaries via approximate polygonal domains has long been measured [Strang and Berger, 1973] and turns out to be controlled by a factor of h^2, where h is the mesh size. For low order methods with errors of the same order in h, like linear Lagrange finite elements or lowest-order Raviart–Thomas elements with errors of the same order, this poses no complication. However, in the case of high order methods, it becomes necessary to adopt new strategies to preserve the original accuracy of the method. Additionally, we note that, since a curved interface involves more than one discretization simultaneously, a variety of new challenges arise, which are not present in the curved boundary case. For instance, matching straight discretizations approximating a curved interface will have one discrete subdomain always escaping its exact counterpart, and if we try to mend this by modifying the discretizations to reside inside their respective exact domains, we then separate the subdomains and leave unmeshed gaps; see Figure 5.1.

Finite element methods concerned with non-conforming geometries, either for curved boundaries or curved interfaces, can broadly be divided into two categories: *fitted* methods, which attempt to fit the discretization to the exact geometry, and *unfitted* methods, where the polygonal mesh is left as is and the boundary/interface conditions are included in a non-standard manner. By approximating the exact geometry, for example by utilizing curved elements as is the case of isoparametric [Ciarlet and Raviart, 1972, Ciarlet, 1973,

Beer, 1985] and isogeometric [Beer and Bordas, 2015, Hughes et al., 2005] finite elements, fitted methods allow boundary conditions to be imposed in strong form (i.e. incorporating them into the discrete subspaces), leading to formulations close to standard. However, the non-linear mappings associated with these curved elements and the possible re-meshing processes when moving geometries are involved can turn out to be quite expensive. For this reason, unfitted methods become quite attractive by avoiding remeshing and allowing greater flexibility in mesh choice. Nonetheless, these upsides do not come for free and the tradeoff is that unfitted methods work with non-standard formulations.

Unfitted methods largely enforce boundary and interface conditions *weakly*, that is to say, they are included in the equations of the method and are not satisfied exactly by the solution. This is contrast to enforcing them *strongly*, usually translating to imposing them in the definition of the trial space, which requires the space to be defined on a domain that fits the exact geometry. Among unfitted methods, we highlight the fictitiuos domain (FD) method [Glowinski et al., 1994], the cut finite element method (CutFEM) [Hansbo, 2005, Burman et al., 2025], and the shifted boundary method (SBM) [Main and Scovazzi, 2018, Atallah et al., 2022]. In particular, for interface problems, we mention mortar methods [Belgacem, 1999, Flemisch et al., 2005] which treat non-matching grids on interfaces. A brief summary of these methods is given in Section 5.2. Also of note is ϕ-FEM [Duprez and Lozinski, 2020] which, instead of weakly imposing the boundary conditions as other unfitted methods, incorporates the geometry by the explicit addition of a level-set function (denoted by ϕ) as a prefactor in the ansatz of the solution. And last, but absolutely not least, we bring up the Transfer Path Method (TPM), originally developed as an unfitted method for boundary value problems using HDG, and which corresponds to the main topic of this part of the thesis.

5.1 Notation and preliminaries

In this section, for the sake of clarity, we give a brief overview of the notation used in the rest of the chapter and introduce some function spaces. We will not, however, go into any details and refer the interested reader to [Brenner and Scott, 2008] and [Ern and Guermond, 2004, 2021] for the general theory of finite elements, and to [Boffi et al., 2013] and [Gatica, 2014] for a closer look at the theory of saddle point problems.

Function spaces

For a bounded open set $\Omega \subset \mathbb{R}^n$ and $\mathrm{d}\boldsymbol{x}$ the Lebesgue measure in $\mathbb{R}^n$, we define:

- the space $L^2(\Omega)$ of square-integrable scalar-valued functions,

$$L^2(\Omega) \coloneqq \left\{ u \text{ is measurable} : \int_\Omega |u|^2 \,\mathrm{d}\boldsymbol{x} < \infty \right\},$$

  provided with the inner product

$$(u, v)_{0,\Omega} \coloneqq \int_\Omega uv \,\mathrm{d}\boldsymbol{x},$$

  and the vector- and tensor-valued equivalents $\boldsymbol{L}^2(\Omega)$ and $\mathbb{L}^2(\Omega)$.

- the space $H^1(\Omega)$ of scalar-valued functions with square-integrable gradient

$$H^1(\Omega) \coloneqq \{u \in L^2(\Omega) : \nabla u \in \boldsymbol{L}^2(\Omega)\},$$

  provided with the inner product

$$(u, v)_{1,\Omega} \coloneqq \int_\Omega uv \,\mathrm{d}\boldsymbol{x} + \int_\Omega \nabla u \cdot \nabla v \,\mathrm{d}\boldsymbol{x},$$

  and a vector-valued equivalent $\boldsymbol{H}^1(\Omega)$, where ∇ is understood as the corresponding Jacobian matrix.

- the space $\boldsymbol{H}(\mathrm{div}; \Omega)$ of vector-valued functions with square-integrable divergence

$$\boldsymbol{H}(\mathrm{div}; \Omega) \coloneqq \{\boldsymbol{u} \in \boldsymbol{L}^2(\Omega) : \nabla \cdot \boldsymbol{u} \in L^2(\Omega)\},$$

  provided with the inner product

$$(\boldsymbol{u}, \boldsymbol{v})_{\mathrm{div},\Omega} \coloneqq \int_\Omega \boldsymbol{u} \cdot \boldsymbol{v} \,\mathrm{d}\boldsymbol{x} + \int_\Omega (\nabla \cdot \boldsymbol{u})(\nabla \cdot \boldsymbol{v}) \,\mathrm{d}\boldsymbol{x},$$

  and its tensor-valued equivalent $\mathbb{H}(\mathrm{div}; \Omega)$ with $\nabla \cdot$ taken row-wise.

For a co-dimension 1 hypersurface $\Gamma \subset \mathbb{R}^{n-1}$ we define

$$L^2(\Gamma) \coloneqq \{\mu \text{ is measurable} : \int_\Gamma |\mu|^2 \,\mathrm{d}s < \infty\},$$

where $\mathrm{d}s$ is the Lebesgue measure in $\mathbb{R}^{n-1}$. The inner product $(\cdot, \cdot)_{0,\Gamma}$ and vector- and tensor-valued spaces, $\boldsymbol{L}^2(\Gamma)$ and $\mathbb{L}^2(\Gamma)$, are defined analogously as in the n-dimensional case. In particular, we will make use of these spaces for boundaries $\Gamma = \partial\Omega$ and interfaces $\Gamma = \overline{\Omega_1} \cap \overline{\Omega_2}$.

The restriction $\varphi|_\Gamma$ of a smooth function φ defined on $\mathbb{R}^n$ to a lower dimensional hypersurface Γ is well-defined. The following theorem assures us that this can also be done for measurable functions with enough regularity.

Theorem 5.1.1 (Trace theorem). *There exist linear bounded operators $\gamma_0 : H^1(\Omega) \to L^2(\partial\Omega)$ and $\gamma_{\boldsymbol{\nu}} : \boldsymbol{H}(\mathrm{div};\Omega) \to L^2(\partial\Omega)$ such that the following integration-by-parts identity holds:*

$$\int_\Omega \nabla u \cdot \boldsymbol{v}\,\mathrm{d}\boldsymbol{x} = -\int_\Omega u(\nabla\cdot\boldsymbol{v}) + \int_{\partial\Omega} \gamma_0(u)\gamma_{\boldsymbol{\nu}}(\boldsymbol{v})\,\mathrm{d}s, \quad \forall (u,\boldsymbol{v}) \in H^1(\Omega)\times\boldsymbol{H}(\mathrm{div};\Omega)$$

and, for all $\varphi \in \mathcal{C}^\infty(\Omega)$, $\boldsymbol{\varphi} \in [\mathcal{C}^\infty(\Omega)]^n$,

$$\gamma_0(\varphi) = \varphi|_{\partial\Omega}, \qquad \gamma_{\boldsymbol{\nu}}(\boldsymbol{\varphi}) = (\boldsymbol{\varphi}\cdot\boldsymbol{\nu})|_{\partial\Omega},$$

where $\boldsymbol{\nu}$ is the exterior unit normal vector to $\partial\Omega$.

Furthermore, the spaces $H^{\frac{1}{2}}(\partial\Omega) := \gamma_0(H^1(\Omega))$ and $H^{-\frac{1}{2}}(\partial\Omega) := \gamma_{\boldsymbol{\nu}}(\boldsymbol{H}(\mathrm{div};\Omega))$ are closed.

Remark. There exist multiple ways to define the spaces $H^{\frac{1}{2}}$ and $H^{-\frac{1}{2}}$, and admittedly this is a very strange way of doing it, but in this context we are only interested in them as spaces that will contain the traces of the functions we are interested in. However, we must note that the second integral in Theorem 5.1.1 must be understood in the sense of duality pairings and so we stress the fact that $H^{-\frac{1}{2}}$ corresponds to the *dual* of $H^{\frac{1}{2}}$.

We will also use the spaces $H^1_0(\Omega) := \gamma_0^{-1}(0)$ and $\boldsymbol{H}_0(\mathrm{div};\Omega) = \gamma_{\boldsymbol{\nu}}^{-1}(0)$.

Solvability

The two following theorems form the basis of the solvability analysis of weak problems. In the statement of both theorems, all spaces are Hilbert spaces and all bilinear forms considered are real-valued and bounded (hence continuous), that is, for $\phi : X\times Y \to \mathbb{R}$ bilinear, there exists $C > 0$ such that

$$|\phi(x,y)| \le C||x||_X||y||_Y \qquad \forall x\in X, y\in Y.$$

Theorem 5.1.2 (Lax–Milgram). *Given $a : U\times U \to \mathbb{R}$ fixed, it holds that, for all $f \in U^*$, there exists a unique $u \in U$ such that*

$$a(u,v) = f(v), \qquad \forall v \in U \tag{5.2}$$

if a is coercive*, that is, there exists $\alpha > 0$ such that*

$$|a(v,v)|_U \ge \alpha||v||_U^2 \qquad \forall v\in U.$$

Theorem 5.1.3 (Ladyzhenskaya–Babuška–Brezzi). *Given $a : \boldsymbol{Q}\times\boldsymbol{Q} \to \mathbb{R}$, $b : \boldsymbol{Q}\times U \to \mathbb{R}$, it holds that, for $f \in \boldsymbol{Q}^*$ and $g \in U^*$, there exist a unique pair $(\boldsymbol{q}, u)$ such that*

$$\begin{aligned} a(\boldsymbol{q},\boldsymbol{r}) + b(\boldsymbol{r},u) &= f(\boldsymbol{r}) \\ b(\boldsymbol{q},v) &= g(v) \end{aligned}$$

if and only if

- *there exists* $\beta_a > 0$ *such that*

$$\sup_{\boldsymbol{r}\in\boldsymbol{Z}\setminus\{\boldsymbol{0}\}} \frac{a(\boldsymbol{r},\boldsymbol{p})}{||\boldsymbol{r}||_{\boldsymbol{Q}}} \geq \beta_a ||\boldsymbol{p}||_{\boldsymbol{Q}}, \qquad \boldsymbol{p}\in\boldsymbol{Z}, \tag{5.4}$$

$$\sup_{\boldsymbol{p}\in\boldsymbol{Z}} a(\boldsymbol{r},\boldsymbol{p}) > 0, \qquad \boldsymbol{r}\in\boldsymbol{Q}\setminus\{\boldsymbol{0}\}, \tag{5.5}$$

  where $\boldsymbol{Z} = \{\boldsymbol{p}\in\boldsymbol{Q} : b(\boldsymbol{p},v) = 0, \forall v\in U\}$.

- *there exists* $\beta_b > 0$

$$\sup_{\boldsymbol{r}\in\boldsymbol{Q}\setminus\{\boldsymbol{0}\}} \frac{b(\boldsymbol{r},v)}{||\boldsymbol{r}||_{\boldsymbol{Q}}} \geq \beta_b ||v||_U. \tag{5.6}$$

Discrete setting

Given a bounded open set Ω and a parameter $0 < h \leq 1$, we define a *mesh* as a finite collection of bounded open sets $\{K_i\}_{i\in I}$ such that $\operatorname{diam} K_i \leq h$ for all $i\in I$, $K_i\cap K_j = \emptyset$ for $i\neq j$ and $\overline{\Omega}\approx\Omega_h := \bigcup_{i\in I} K_i$. We use $\approx$ in the last condition as we will consider cases where $\Omega\subset\Omega_h$ or $\Omega\supset\Omega_h$, in addition to the usual case $\Omega=\Omega_h$. When considering a family of meshes, we index the discretizations by h and write $\mathcal{T}_h = \{K_i\}_{i\in I}$. We will assume that all families are quasi-uniform; see [Brenner and Scott, 2008].

The space of polynomials on $K\subset\mathbb{R}^n$ of degree *up to* k is denoted by $\mathcal{P}_k(K)$ and the space of polynomials of degree *exactly equal to* k by $\widetilde{\mathcal{P}}_k(K)$

We define a *face* F as the intersection $\overline{K_{\mathrm{L}}}\cap\overline{K_{\mathrm{R}}}$ for $K_{\mathrm{L}}, K_{\mathrm{R}}\in\mathcal{T}_h$. The set of faces of $\mathcal{T}_h$ is called the *skeleton* of the mesh and denoted by $\mathcal{E}_h$.

We define the mesh-dependent inner products

$$(u,v)_{0,\mathcal{K}} := \sum_{K\in\mathcal{K}} (u,v)_{0,K}, \qquad \langle u,v\rangle_{0,\mathcal{F}} := \sum_{F\in\mathcal{F}} \langle u,v\rangle_{0,F},$$

where $\mathcal{K}\subset\mathcal{T}_h$ and $\mathcal{F}\subset\mathcal{E}_h$. Additionally, we define

$$\langle u,v\rangle_{0,\partial\mathcal{K}} := \sum_{K\in\mathcal{K}}\sum_{F\in\partial K} \langle u,v\rangle_{0,F}.$$

For a generic Sobolev space H, we define its broken version as

$$H(\mathcal{T}_h) := \prod_{K\in\mathcal{T}_h} H(K) = \{u\in L^2(\cup_{K\in\mathcal{T}_h}K) : u|_K\in H(K), \qquad \forall K\in\mathcal{T}_h\}.$$

The following result allows us to characterize global conformity through inter-element continuity of the traces:

Theorem 5.1.4 (Inter-element continuity). *Given a partition $\mathcal{T}_h$ with $\Omega = \cup_{K\in\mathcal{T}_h} K$,*

$$\begin{aligned}\boldsymbol{H}(\mathrm{div}; K) &= \{\boldsymbol{u} \in \boldsymbol{H}(\mathrm{div}; \mathcal{T}_h) : \langle \gamma_0(v), \gamma_{\boldsymbol{\nu}}(\boldsymbol{u})\rangle_{0,\partial\mathcal{K}} = 0,\ \forall v \in H_0^1(K)\},\\ H^1(K) &= \{u \in H^1(\mathcal{T}_h) : \langle \gamma_0(u), \gamma_{\boldsymbol{\nu}}(\boldsymbol{q})\rangle_{0,\partial\mathcal{K}} = 0,\ \forall \boldsymbol{q} \in \boldsymbol{H}_0^1(\mathrm{div}; K)\}.\end{aligned}$$

What the previous theorem tells us is that H^1 functions can be glued together into a globally-H^1 function so long as their traces match on the inter-element interfaces, and the same is true for $\boldsymbol{H}(\mathrm{div})$ functions using their normal trace.

5.2 Overview of unfitted finite element methods

5.2.1 Fictitious domain methods

FD methods [Glowinski et al., 1994, 1995] consist of using a background mesh, usually a structured grid, and weakly imposing the Dirichlet boundary conditions on the solution u_0 via the addition of a Lagrange multiplier μ; see Figure 5.2. Boundary conditions on the fictitious domain can be then chosen in a convenient manner, e.g. null Dirichlet, null Neumann or even periodic.

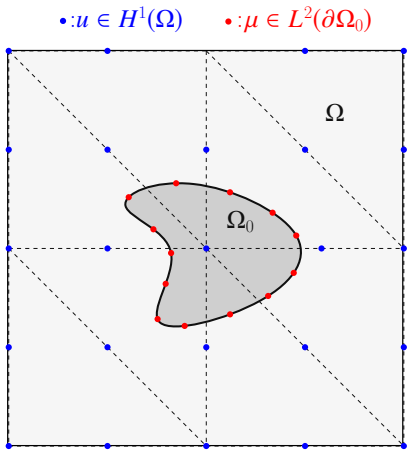

Figure 5.2: Physical domain Ω_0 embedded in the fictitious domain Ω, with $\mathcal{P}_2$ Lagrange degrees of freedom for u and $\mathcal{P}_0$ discontinuous degrees of freedom on μ. The FD method solves for u defined on the larger domain Ω and produces an approximation $u_0 = u|_{\Omega_0}$, utilizing μ as a multiplier enforcing the constraint $u = g$ on $\partial\Omega_0$.

Recently, an FD method for an interface problem was developed by Regazzoni [2024],

extending an exterior subdomain *inwards* and then imposing equality via multipliers on either the entire overlap region ($\mu \in L^2(\Omega_2)$) or only the interface ($\mu \in L^2(\overline{\Omega_1} \cap \overline{\Omega_2})$.

5.2.2 Mortar methods

Mortar methods [Bernardi, 1994] utilize a Lagrange multiplier to weakly impose zero jump of the solution across each interface; see Figure 5.3. This is convenient for Lagrange elements where the degrees of freedom correspond to node evaluations, since the non-conformity of the nodes between contiguous discretizations pose a difficulty for the imposition of continuity.

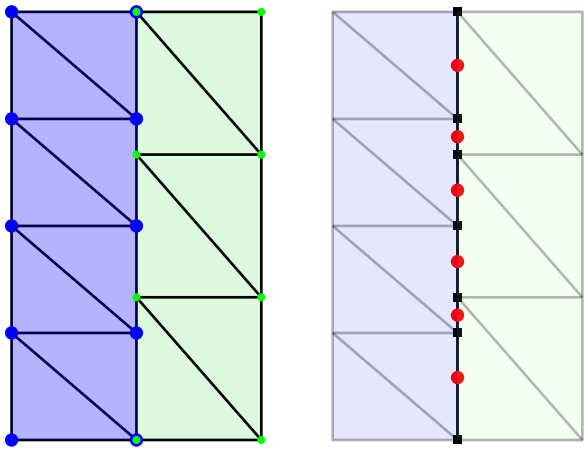

Figure 5.3: Non-matching contiguous grids and $\mathcal{P}_1$ Lagrange degrees of freedom (left) and $\mathcal{P}_0$ discontinuous degrees of freedom for the multiplier (right). Note that the multiplier is not defined on edges of the discretization, but on subsets of the edges corresponding to intersections of contiguous edges.

Remark. By setting a condition across element interfaces, the Lagrange multipliers are consequently defined on the skeleton of the mesh, which is similar to the numerical traces defined on the HDG method. Consequently, one can interpret the HDG method as an element-by-element mortar method.

5.2.3 CutFEM

For a thorough introduction to the CutFEM paradigm, we refer the reader to [Burman et al., 2025].

In CutFEM, the mesh is allowed to be *cut* by the exact geometry; see Figure 5.4. Integration is assumed to be able to be performed using information on the exact geometry, the latter usually handled by a level-set function. Boundary/interface conditions are imposed weakly either by a multiplier, like in FD, or by utilizing Nitsche's method [Nitsche, 1970].

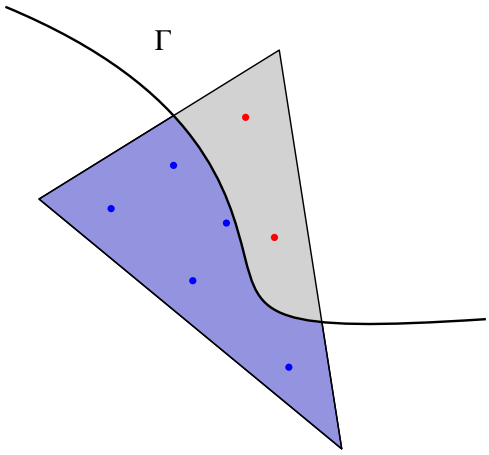

Figure 5.4: An element can be cut by a curve Γ, leaving degrees of freedom on either side of the cut.

The cuts on the elements may be arbitrarily small, leading to unstable formulations. To that end, different stabilization strategies exist, classified as either *weak* stabilizations, in which a stabilization linear form is included in the formulation to enhance coercivity, or *strong* stabilizations, in which the discrete spaces are modified by eliminating unstable degrees of freedom and replacing them by extensions from robust elements.

CutFEM can also handle interface problems and it is done by doubling the degrees of freedom along the interface as seen in Figure 5.5.

5.2.4 Shifted Boundary Methods (SBM)

In the SBM, as opposed to the FD, the PDE is solved on a smaller surrogate domainand the boundary conditions are imposed weakly on the resulting boundary of this smaller subdomain. In order to preserve the order of accuracy, the boundary value g is *shifted* to a surrogate $\tilde{g}$ via a truncated Taylor expansion.

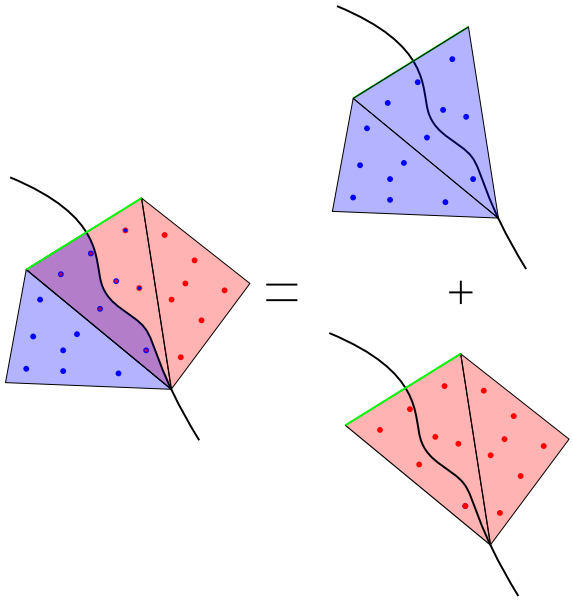

Figure 5.5: The meshes for both subdomains overlap in the cut elements. The yellow edge is where the ghost penalty will be defined.

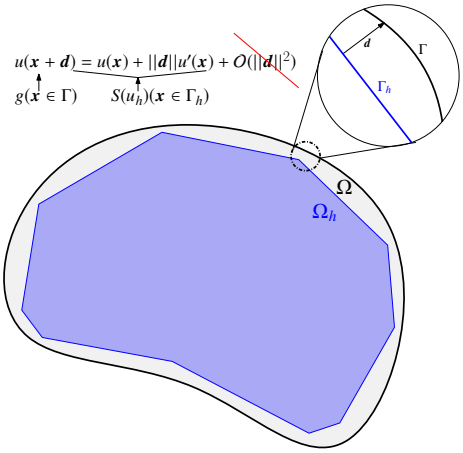

Figure 5.6: A Taylor expansion allows the shifting of boundary conditions.

5.3 A short introduction to the HDG method

The Hybridizable Discontinuous Galerkin (HDG) method was first introduced as such in [Cockburn et al., 2009]. It consists of discretizing of a PDE cast in mixed (flux-potential) form and introducing approximations of inter-element values to solve a Galerkin formulation on broken spaces. For this reason it has also been referred to in the literature as the LDG-H [Cockburn et al., 2008, 2014] method for its close resemblance to the Locally Discontinuous Galerkin (LDG) method [Cockburn and Shu, 1998]. However, in the HDG method, one of these inter-element values is treated as an additional *hybrid* variable, usually the trace of the potential on the skeleton of the domain mesh, and the remaining inter-element value is treated as a proper *numerical flux*, a function of the intra-element unknowns and the hybrid variable. These fluxes are then used to construct a stabilized non-conforming formulation weakly enforcing transmission conditions across inter-element boundaries. This type of formulation is well suited for *static condensation*, separating the solution process into a *global* system depending only on the hybrid variable and subsequently solving a number of *local* problems for the original flux and potential, the latter solved in parallel.

We note that hybrid variable can be interpreted as a lagrange multiplier imposing the continuity of the normal component of the flux across inter-element boundaries, a process in general called *hybridization*, which places the HDG method as a close relative of the Hybridized Mixed (HM) methods [Boffi et al., 2013, Sections 7.1.4–7.1.6]. However, since hybridization does not always lead to a stable method for any choice of local approximation spaces, the HDG method introduces a *stabilization* form that ensures solvability and optimal convergence. However, as noted in [Cockburn, 2023], this makes the HDG a generalization of HM methods as they coincide when the stabilization form vanishes everywhere.

Remark. The term *hybridized* discontinuous Galerkin may refer to a discontinuous Galerkin formulation for which a hybrid variable has been introduced, such as the case of hybrid dG methods used by Lehrenfeld and Schöberl [2016] based on the Interior Penalty method. Closely related are the HDG methods based on primal formulations developed by Rhebergen and Wells [2018], Kirk et al. [2019], Cesmelioglu et al. [2023]. For that reason, we specify that in the rest of this thesis we will use the HDG exclusively for the family based on *mixed* formulations.

In the rest of this section, we largely follow Cockburn [2023] and give a brief overview of the path from M(G) to HM(G) to HDG with a brief visit to LDG.

5.3.1 The mixed formulation

For an introduction to the topic, we refer the reader to [Gatica, 2014] and to [Boffi et al., 2013] for a more in-depth coverage.

The continuous problem

Consider the standard diffusion-reaction problem for a potential u with positive-definite diffusion tensor $\mathbb{K}$ and reaction rate $c_0 > 0$, along with source datum f and boundary datum g_D:

$$-\nabla \cdot (\mathbb{K}\nabla u) = f - c_0 u, \qquad \text{in } \Omega, \tag{5.7a}$$
$$u = g_D, \qquad \text{on } \partial\Omega. \tag{5.7b}$$

By explicitly introducing the flux $\boldsymbol{q} = -\mathbb{K}\nabla u$, we can reduce Equation (5.7a) to the first-order system

$$\mathbb{K}^{-1}\boldsymbol{q} + \nabla u = 0, \qquad \text{in } \Omega, \tag{5.8a}$$
$$\nabla \cdot \boldsymbol{q} + c_0 u = f, \qquad \text{in } \Omega, \tag{5.8b}$$

from which we get the weak form

$$\int_\Omega \mathbb{K}^{-1}\boldsymbol{q} \cdot \boldsymbol{v} \,\mathrm{d}\boldsymbol{x} + \int_\Omega \nabla u \cdot \boldsymbol{v} \,\mathrm{d}\boldsymbol{x} = 0, \tag{5.9a}$$
$$\int_\Omega (\nabla \cdot \boldsymbol{q}) w \,\mathrm{d}\boldsymbol{x} + c_0 \int_\Omega u w \,\mathrm{d}\boldsymbol{x} = \int_\Omega f w \,\mathrm{d}\boldsymbol{x}. \tag{5.9b}$$

Remark. Note that, in some way, Equations (5.8a–b) is a more natural way of stating a balance equation, as Equation (5.8b) is the *balance equation* (e.g heat sources relate directly to the heat flux) and Equation (5.8a) is the corresponding *constitutive equation* (e.g. heat flux is a function of the temperature).

If we integrate by parts the second term of Equation (5.9a), we obtain

$$\int_\Omega \mathbb{K}^{-1}\boldsymbol{q} \cdot \boldsymbol{v} \,\mathrm{d}\boldsymbol{x} - \int_\Omega u(\nabla \cdot \boldsymbol{v}) \,\mathrm{d}\boldsymbol{x} = -\int_{\partial\Omega} \gamma_{\boldsymbol{\nu}}(\boldsymbol{v})\gamma_0(u), \tag{5.10a}$$
$$\int_\Omega (\nabla \cdot \boldsymbol{q}) w \,\mathrm{d}\boldsymbol{x} = \int_\Omega f w \,\mathrm{d}\boldsymbol{x}. \tag{5.10b}$$

for which we see that the left-hand side makes sense if $\nabla \cdot \boldsymbol{q}, \nabla \cdot \boldsymbol{v}, u, w \in L^2(\Omega)$ and $\gamma_0(u)$ is equal to the boundary datum in Equation (5.7b), where we recall that the right-hand side of Equation (5.14a) is a formal way of writing the duality between $H^{-\frac{1}{2}}(\partial\Omega) \ni \gamma_{\boldsymbol{\nu}}(\boldsymbol{v})$ and $H^{\frac{1}{2}}(\partial\Omega)$, the latter being the correct space for g_D.

Problem 5.3.1 (Primal mixed formulation). *Find* $(\boldsymbol{q}, u) \in \boldsymbol{H}(\mathrm{div};\Omega) \times L^2(\Omega)$ *such that*

$$a(\boldsymbol{q}, \boldsymbol{v}) + b(\boldsymbol{v}, u) = G_{\mathrm{D}}(\boldsymbol{v}), \tag{5.11a}$$

$$b(\boldsymbol{q}, w) - c(u, w) = F(w). \tag{5.11b}$$

for all $(\boldsymbol{v}, w) \in \boldsymbol{H}(\mathrm{div};\Omega) \times L^2(\Omega)$*, where*

$$a(\boldsymbol{v}_1, \boldsymbol{v})_2 \coloneqq \left(\mathbb{K}^{-1}\boldsymbol{v}_1, \boldsymbol{v}_2\right)_{\boldsymbol{L}^2(\Omega)}, \quad b(\boldsymbol{v}, w) \coloneqq (\nabla \cdot \boldsymbol{v}, w)_{L^2(\Omega)},$$

$$c(w_1, w_2) \coloneqq c_0(u, w)_{L^2(\Omega)},$$

$$G_{\mathrm{D}}(\boldsymbol{v}) = -\langle g, \gamma_{\boldsymbol{\nu}}(\boldsymbol{v})\rangle_{H^{\frac{1}{2}}(\partial\Omega)\times H^{-\frac{1}{2}}(\partial\Omega)}, \quad F(w) = -(f, w)_{L^2(\Omega)}.$$

While the primal mixed formulation will be the our starting point to derive the HDG method, for the completion's sake we present an alternative formulation, usually considered nonstandard but with some theoretical uses as studied in [Bertrand and Boffi, 2025].

If we replace Equation (5.7b) by

$$-\mathbb{K}\nabla u \cdot \boldsymbol{\nu} = g_{\mathrm{N}} \in H^{-1/2}(\partial\Omega) \qquad \text{on } \partial\Omega$$

and we instead integrate by parts the first term of Equation (5.9b), we will obtain the *dual mixed* formulation.

Problem 5.3.2 (Dual mixed diffusion equation). *Find* $(\boldsymbol{q}, u) \in \boldsymbol{L}^2(\Omega) \times H^1(\Omega)$ *such that*

$$a(\boldsymbol{q}, \boldsymbol{v}) + \tilde{b}(\boldsymbol{v}, u) = 0, \tag{5.12a}$$

$$\tilde{b}(\boldsymbol{q}, w) - c(u, w) = G_{\mathrm{N}}(w) + F(w). \tag{5.12b}$$

for all $(\boldsymbol{v}, w) \in \boldsymbol{L}^2(\Omega) \times H^1(\Omega)$*, where*

$$\tilde{b}(\boldsymbol{v}, w) \coloneqq (\boldsymbol{v}, \nabla w)_{\boldsymbol{L}^2(\Omega)}, \quad G_{\mathrm{N}} \coloneqq \langle \gamma_0(w), g_{\mathrm{N}}\rangle_{H^{\frac{1}{2}}(\partial\Omega)\times H^{-\frac{1}{2}}(\partial\Omega)}.$$

An important aspect of mixed formulations is that what we have done thus far is essentially incorporating a *Lagrange multiplier* into our problem. In effect, taking $c_0 \equiv 0$, if we look at Problem 5.3.1, we see that it corresponds to finding a stationary point through the optimality conditions of the constrained saddle point problem, known as the *complementary energy principle*

$$\min_{\substack{\boldsymbol{q}\in\boldsymbol{H}(\mathrm{div};\Omega)\\ \nabla\cdot\boldsymbol{q}=f}} \frac{1}{2}\int_\Omega \left|\mathbb{K}^{-\frac{1}{2}}\boldsymbol{q}\right| \,\mathrm{d}\boldsymbol{x} \tag{5.13}$$

for which $u \in L^2(\Omega)$ will act as the Lagrange multiplier enforcing the equilibrium equation $\nabla \cdot \boldsymbol{q} = f$.

Remark. Note that Dirichlet boundary conditions are *natural* in Problem 5.3.1 and would be *essential* in Problem 5.3.2, whereas the opposite holds for Neumann boundary conditions. This *naturalizaton* of Dirichlet boundary conditions will later become of great importance in the development of the local solvers by enabling the definition of appropriate liftings.

The Galerkin method

Standard finite element methods for this problem rely on constructing conforming finite-dimensional subspaces that satisfy a discrete version of Theorem 5.1.3. In general, we can write conforming formulations by considering a (simplicial) mesh $\mathcal{T}_h$ of Ω and the spaces $\boldsymbol{V}_h \times W_h \subset \boldsymbol{H}(\mathrm{div};\Omega) \times L^2(\Omega)$ such that our problem is: find $(\boldsymbol{q}_h, u_h) \in \boldsymbol{V}_h \times W_h$ such that

$$a(\boldsymbol{q}_h, \boldsymbol{v}_h) + b(\boldsymbol{v}_h, u_h) = G_{\mathrm{D}}(\boldsymbol{v}_h), \tag{5.14a}$$
$$b(\boldsymbol{q}_h, w_h) - c(u_h, w_h) = F(w_h). \tag{5.14b}$$

for all $(\boldsymbol{v}, w) \in \boldsymbol{V}_h \times W_h$, where

$$\boldsymbol{V}_h = \left[\prod_{K\in\mathcal{T}_h} \boldsymbol{V}(K)\right] \cap \boldsymbol{H}(\mathrm{div};\Omega), \qquad W_h = \prod_{K\in\mathcal{T}_h} W(K)$$

with $\boldsymbol{V}(K)$, $W(K)$ the *local* spaces on the triangle K, and where we see that the global conformity requirement on $\boldsymbol{V}_h$ translates to imposing continuity of the normal components across inter-element boundaries (see Theorem 5.1.4),

$$((\boldsymbol{v}\cdot\boldsymbol{\nu})|_{\partial K_{\mathrm{L}}} + (\boldsymbol{v}\cdot\boldsymbol{\nu})|_{\partial K_{\mathrm{R}}})|_{\partial K_{\mathrm{L}}\cap\partial K_{\mathrm{R}}} = 0, \quad \forall K_{\mathrm{L}}, K_{\mathrm{R}} \in \mathcal{T}_h. \tag{5.15}$$

Remark. We note that, since we are working with finite-dimensional spaces, more precisely polynomial spaces, we can safely drop the trace operators $\gamma_0, \gamma_{\boldsymbol{\nu}}$ and write directly w and $\boldsymbol{v}\cdot\boldsymbol{\nu}$ for the usual and normal traces, respectively.

Suitable choices of local spaces $\boldsymbol{V}(K)$ are the Brezzi–Douglas–Marini space of order k

$$\mathcal{BDM}_k(K) \coloneqq \{p \in [\mathcal{P}_k(K)]^d : p\cdot\boldsymbol{\nu} \in \mathcal{P}_k(e), \forall e \in \partial K\},$$

or the Raviart–Thomas space of order k

$$\mathcal{RT}_k(K) \coloneqq \{p \in [\mathcal{P}_k(K)]^d \oplus \boldsymbol{m}(\boldsymbol{x})\mathcal{P}_k(K) : p\cdot\boldsymbol{\nu} \in \mathcal{P}_k(e), \forall e \in \partial K\},$$

where $\boldsymbol{m}(\boldsymbol{x})\mathcal{P}_k(K) \coloneqq \{p(\boldsymbol{x}) \in [\mathcal{P}_{k+1}(K)]^d : p = \boldsymbol{x}v(\boldsymbol{x}),\ v \in \mathcal{P}_k(K)\}$. Inf-sup stable pairs are obtained when $\mathcal{BDM}_k$ is paired with $W(K) = \mathcal{P}_{k-1}(K)$ and $\mathcal{RT}_k$ is paired with $\mathcal{P}_k(K)$.

Although inf-sup stable formulations for the diffusion equation have been studied for decades (see [Boffi et al., 2013] and references therein), it poses a difficulty in the analysis to construct the correct stable discrete subspaces. Moreover, the saddle-point nature of the mixed problem leads to a linear system with an *indefinite matrix*, which limits the class of solvers applicable.

5.3.2 The hybridized mixed (HM) formulation

The strategy of hybridization was first utilized by Fraeijs de Veubeke [1965] and has proven to be an extremely useful resource for devising computationally effective methods for solving second-order elliptic problems; see [Cockburn and Gopalakrishnan, 2005]. In this section, we give a very brief description of its application to the mixed formulation developed above and give comments on the *static condensation* process.

If we consider Equation (5.15) as a constraint equation, we can rewrite it as

$$\sum_{K\colon e\in\partial K}\int_e (\boldsymbol{v}_h\cdot\boldsymbol{\nu})\mu\,\mathrm{d}s = 0,\quad \mu\in\mathcal{P}_k(e),\quad \forall e\in\mathcal{E}_0(\mathcal{T}_h),$$

where $\mathcal{E}_0(\mathcal{T}_h)$ is the interior skeleton of the mesh. This motivates the introduction of the space

$$M_h \coloneqq \prod_{e\in\mathcal{E}_0(\mathcal{T}_h)} \mathcal{P}_k(e)$$

and a new non-conforming formulation with

$$\boldsymbol{V}_h \coloneqq \prod_{K\in\mathcal{T}_h} \boldsymbol{V}(K) \subsetneq \boldsymbol{H}(\mathrm{div};\Omega)$$

Problem 5.3.3 (Hybridized primal mixed method). *Find* $(\boldsymbol{q}_h, u_h, \lambda_h)\in \boldsymbol{V}_h\times W_h\times M_h$ *such that*

$$\sum_{K\in\mathcal{T}_h}\int_K \mathbb{K}^{-1}\boldsymbol{q}_h\cdot\boldsymbol{v}_h\,\mathrm{d}\boldsymbol{x} - \int_K u_h(\nabla\cdot\boldsymbol{v}_h)\,\mathrm{d}\boldsymbol{x} + \int_{\partial K}(\boldsymbol{v}_h\cdot\boldsymbol{\nu})\lambda_h\,\mathrm{d}s = 0,\quad \forall\boldsymbol{v}_h\in\boldsymbol{V}_h, \tag{5.16a}$$

$$\sum_{K\in\mathcal{T}_h}\int_K (\nabla\cdot\boldsymbol{q}_h)v\,\mathrm{d}\boldsymbol{x} - \int_K fv\,\mathrm{d}\boldsymbol{x} = 0,\quad \forall v\in W_h, \tag{5.16b}$$

$$\sum_{K\in\mathcal{T}_h}\int_{\partial K}(\boldsymbol{q}_h\cdot\boldsymbol{\nu})\mu\,\mathrm{d}s = 0,\quad \forall\mu\in M_h. \tag{5.16c}$$

for all $(\boldsymbol{v}_h, w_h, \mu_h)\in\boldsymbol{V}_h\times W_h\times M_h$.

Remark. It is possible to give meaning to the Lagrange multiplier by noting that, integrating by parts the second term in Equation (5.16a), it follows that $u|_e = \lambda|_e$.

Static condensation

The reduction of systems involving intra-element and boundary degrees degrees of freedom to systems involving only the latter has been utilized by engineers for decades [Guyan, 1965] and is one of the most attractive properties of hybridized methods.

We make the following observation: since the spaces for $\boldsymbol{q}_h$ and u_h have no inter-element dependency, a global basis of $\boldsymbol{V}_h$ can consist of functions that are zero on every element except one, on which one uses the appropriate basis for the corresponding local space associated to that element. Consequently, Equations (5.16a–b) define a local problem on each K for which $\lambda_h|_{\partial K}$ is the Dirichlet boundary datum. This motivates the definition of the liftings $\lambda \mapsto (\boldsymbol{q}_h^\lambda, u_h^\lambda)$ in which $(\boldsymbol{q}^\lambda, u^\lambda)$ is the gluing of solutions to each local problem with $f = 0$. Then, we have the bilinear form $H_h : M_h \times M_h \to \mathbb{R}$ given by

$$H_h(\lambda_h, \mu_h) = \int_\Omega \mathbb{K}^{-1} \boldsymbol{q}^{\lambda_h} \cdot \boldsymbol{v}^{\mu_h} \,\mathrm{d}\boldsymbol{x} + c_0 \int_\Omega u^{\lambda_h} w^{\mu_h} \,\mathrm{d}\boldsymbol{x}$$

and $\lambda_h \in M_h$ is part of a solution triple of Problem 5.3.3 if and only if it solves

$$H_h(\lambda_h, \mu_h) = \int_\Omega f w_h^{\mu_h}, \qquad \forall \mu_h \in M_h, \tag{5.17}$$

with H_h clearly a symmetric positive definite (SPD) bilinear form, and so its associated matrix $\mathbb{H}_h$ will be SPD as well, which makes it well suited for a variety of numerical methods.

5.3.3 The locally discontinuous Galerkin (LDG) formulation

Thus far we have considered formulations within the framework of the inf-sup condition for solvability. Taking a step aside, we look into a discontinuous Galerkin formulation.

One cannot take both $\boldsymbol{q}$ and u in H^1 because the inf-sup condition will not hold (H^1 is too small with respect to $\boldsymbol{H}^1$ for the divergence operator to be surjective, that is, the inf-sup will not hold). Therefore, we cannot simultaneously integrate by parts Equation (5.9a) and Equation (5.9b). However, if we look at a completely discontinuous approach disregarding inf-sup stability, we are allowed to assume such regularity and obtain, locally, for $K \subset \Omega$ and $(\boldsymbol{q}, u) \in \boldsymbol{H}^1(K) \times H^1(K)$

$$\int_K \mathbb{K}^{-1} \boldsymbol{q} \cdot \boldsymbol{v} \,\mathrm{d}\boldsymbol{x} - \int_K u(\nabla \cdot \boldsymbol{v}) \,\mathrm{d}\boldsymbol{x} + \int_{\partial K} \gamma_{\boldsymbol{\nu}}(\boldsymbol{v}) \gamma_0(u) = 0, \tag{5.18a}$$

$$- \int_K \boldsymbol{q} \cdot \nabla w \,\mathrm{d}\boldsymbol{x} + \int_{\partial K} \gamma_{\boldsymbol{\nu}}(\boldsymbol{q}) \gamma_0(w) \,\mathrm{d}s = \int_K f w \,\mathrm{d}\boldsymbol{x}. \tag{5.18b}$$

In order to extend Equations (5.18a–b) to a global context, we will seek discrete solutions

$$\boldsymbol{q} \approx \boldsymbol{q}_h \in \prod_{K \in \mathcal{T}_h} \boldsymbol{V}(K) =: \boldsymbol{V}_h^{\mathrm{DG}}, \qquad u \approx u_h \in \prod_{K \in \mathcal{T}_h} W(K) =: W_h^{\mathrm{DG}}$$

satisfying the local compatibility condition (for more details, see [Castillo et al., 2000])

$$\nabla W(K) \subset \boldsymbol{V}(K), \qquad \forall K \in \mathcal{T}_h$$

and introduce the *numerical fluxes* $\gamma_0(u) \approx \hat{u}_h = \hat{u}_h(\boldsymbol{q}_h, u_h)$ and $\gamma_\nu(\boldsymbol{q}) \approx \widehat{\boldsymbol{q}\cdot\boldsymbol{\nu}}$ so that our discrete problem is the following.

Problem 5.3.4 (Locally discontinuous Galerkin method). *Find* $(\boldsymbol{q}_h, u_h) \in \boldsymbol{V}_h \times W_h$ *such that*

$$\int_{\mathcal{T}_h} \mathbb{K}^{-1}\boldsymbol{q}_h \cdot \boldsymbol{v}_h \,\mathrm{d}\boldsymbol{x} - \int_{\mathcal{T}_h} u_h(\nabla\cdot\boldsymbol{v}_h)\,\mathrm{d}\boldsymbol{x} + \int_{\partial\mathcal{T}_h} (\boldsymbol{v}_h\cdot\boldsymbol{\nu})\hat{u}(\boldsymbol{q}_h, u_h) = 0, \tag{5.19a}$$

$$-\int_{\mathcal{T}_h} \boldsymbol{q}\cdot\nabla w \,\mathrm{d}\boldsymbol{x} + \int_{\partial\mathcal{T}_h} \widehat{\boldsymbol{q}\cdot\boldsymbol{\nu}}(\boldsymbol{q}_h, u_h) w \,\mathrm{d}s = \int_{\mathcal{T}_h} fw \,\mathrm{d}\boldsymbol{x}. \tag{5.19b}$$

for all $(\boldsymbol{v}_h, w_h) \in \boldsymbol{V}_h \times W_h$.

The numerical fluxes are defined as

$$\hat{u}|_e = \{\!\{u_h\}\!\}_e + C_{12}h_e^{-1}[\![u_h]\!]_e - C_{22}[\![\boldsymbol{q}_h\cdot\boldsymbol{\nu}]\!]_e \tag{5.20}$$

$$\widehat{\boldsymbol{q}\cdot\boldsymbol{\nu}}|_e = \{\!\{\boldsymbol{q}_h\}\!\}_e - C_{11}h_e^{-1}[\![u_h]\!]_e - C_{12}[\![\boldsymbol{q}_h\cdot\boldsymbol{\nu}]\!]_e \tag{5.21}$$

for $e \in \mathcal{E}_0(\mathcal{T}_h)$ *with* $C_{22} = 0$, $C_{11} > 0$ *and* C_{12} *arbitrary.*

Remark. The term *locally* in LDG refers to the fact that, as before with the HM method, one can define a lifting $u \mapsto \boldsymbol{q}^u$ using Equation (5.19a) and then eliminate $\boldsymbol{q}_h$ from Equation (5.19b) and solve it only in terms of u. This is possible because $C_{22} = 0$, eliminating the dependency of $\hat{u}$ on $\boldsymbol{q}_h$.

5.3.4 The hybridizable discontinuous Galerkin (HDG) formulation

We arrive at the end of the road and are now ready to state the HDG method for Equations (5.7a–b). Starting from the LDG formulation, we mimic the HM formulation and introduce a multiplier $\hat{u}_h \in M_h$ and utilize it in place of the numerical flux $\hat{u}(\boldsymbol{q}_h, u_h)$. As with mixed formulations attempting to circumvent the inf-sup condition [Franca and Hughes, 1988], a stabilization term will be added to the formulation, in this case it goes into the definition of the new numerical flux

$$\widehat{\boldsymbol{q}_h\cdot\boldsymbol{\nu}}|_{\partial K} \coloneqq \boldsymbol{q}_h\cdot\boldsymbol{\nu}|_{\partial K} + \tau_K(u_h|_{\partial K} - \hat{u}_h|_{\partial K}), \tag{5.22}$$

where τ_K is a function that can vary on ∂K.

By utilizing Equation (5.22) in Equation (5.19b), we can integrate back by parts and obtain the following HDG formulation.

Problem 5.3.5 (Hybridizable discontinuous Galerkin method). *Find* $(\boldsymbol{q}_h, u_h, \hat{u}_h) \in \boldsymbol{V}_h \times W_h \times M_h$ *such that*

$$\int_{\mathcal{T}_h} \mathbb{K}^{-1}\boldsymbol{q}_h \cdot \boldsymbol{v}_h \,\mathrm{d}\boldsymbol{x} - \int_{\mathcal{T}_h} u_h(\nabla \cdot \boldsymbol{v}_h)\,\mathrm{d}\boldsymbol{x} + \int_{\partial\mathcal{T}_h} (\boldsymbol{v}_h \cdot \boldsymbol{\nu})\lambda_h \,\mathrm{d}s = 0, \quad \forall \boldsymbol{v}_h \in \boldsymbol{V}_h, \tag{5.23a}$$

$$\int_{\mathcal{T}_h} (\nabla \cdot \boldsymbol{q}_h) v \,\mathrm{d}\boldsymbol{x} + \int_{\partial\mathcal{T}_h} \tau(u - \hat{u}_h) w_h \,\mathrm{d}\boldsymbol{x} - \int_{\mathcal{T}_h} f w_h \,\mathrm{d}\boldsymbol{x} = 0, \quad \forall w_h \in W_h, \tag{5.23b}$$

$$\int_{\partial\mathcal{T}_h} (\boldsymbol{q}_h \cdot \boldsymbol{\nu} + \tau(u - \hat{u}_h))\mu_h \,\mathrm{d}s = 0, \quad \forall \mu_h \in M_h. \tag{5.23c}$$

for all $(\boldsymbol{v}_h, w_h, \mu_h) \in \boldsymbol{V}_h \times W_h \times M_h$.

Remark. We can interpret the equations of the HDG method as a series of *transmission problems* across each inter-element boundary. In the standard form for the diffusion equation, the transmission conditions are

- continuity of the potential $u_- = u_+$,
- continuity of the normal flux $\boldsymbol{q}_- \cdot \boldsymbol{\nu}_- + \boldsymbol{q}_+ \cdot \boldsymbol{\nu}_+ = 0$,

which are mimicked by the equations of the method by

- setting the numerical trace $\hat{u} \in M_h$, ensuring continuity by having it a single-valued,
- using Equation (5.23c) for a stabilized, weak enforcing of the normal flux continuity.

In terms of matrices, we have the system

$$\begin{pmatrix} \mathbb{M}_h & -\mathbb{C}_h^{\mathsf{t}} & \mathbb{F}_{\boldsymbol{\nu}}^{\mathsf{t}} \\ -\mathbb{C}_h & \mathbb{M}_{\partial,\tau} & \tau\mathbb{F}^{\mathsf{t}} \\ \mathbb{F}_{\boldsymbol{\nu}} & \tau\mathbb{F} & \tau\widetilde{\mathbb{F}} + \widetilde{\mathbb{M}} \end{pmatrix} \begin{pmatrix} [\boldsymbol{q}_h] \\ [u_h] \\ [\hat{u}_h] \end{pmatrix} = \begin{pmatrix} [0] \\ [f] \\ [g] \end{pmatrix}, \tag{5.24}$$

for which we have that $\mathbb{M}_h$, $\mathbb{C}_h$ and $\mathbb{M}_{\partial,\tau}$ are block-diagonal. Equation (5.24) consists of essentially two parts: the PDE at a *local* level, that is, on each $K \subset \mathcal{T}_h$ with boundary data $\hat{u}|\partial K$:

$$\mathbb{A}_{11}^K \begin{pmatrix} [\boldsymbol{q}_h]_K \\ [u_h]_K \end{pmatrix} = -\mathbb{A}_{12}^{\partial K}[\hat{u}_h]_{\partial K} + \begin{pmatrix} [0] \\ [f]_K \end{pmatrix} \tag{5.25}$$

and a flux function across inter-element boundaries

$$\Phi_h^{\partial K} =: \mathbb{A}_{21}^K \begin{pmatrix} [\boldsymbol{q}_h] \\ [u_h] \end{pmatrix} + \mathbb{A}_{22}^{\partial K}[\hat{u}_h]_{\partial K} \tag{5.26a}$$

satisfying

$$\sum_{K \in \mathcal{T}_h} \Phi_h^{\partial K} = [g] \tag{5.26b}$$

Remark. The summation over $K \in \mathcal{T}_h$ in Equation (5.26b) is to be understood as the assemblying process.

Using Equation (5.25), we can eliminate $[\boldsymbol{q}_h], [u_h]$ from Equation (5.26a) and write Equation (5.26b) as

$$\sum_{K\in\mathcal{T}_h} \mathbb{A}_{21}^K \left(-(\mathbb{A}_{11}^K)^{-1}\mathbb{A}_{12}^K[\hat{u}_h]_{\partial K} + (\mathbb{A}_{11}^K)^{-1} \begin{pmatrix} [0] \\ [f]_K \end{pmatrix} \right) + \mathbb{A}_{22}^{\partial K}[\hat{u}_h]_{\partial K} = [g], \tag{5.27}$$

or, in a more orderly manner,

$$\sum_{K\in\mathcal{T}_h} (-\mathbb{A}_{21}^K(\mathbb{A}_{11}^K)^{-1}\mathbb{A}_{12}^K + \mathbb{A}_{22}^{\partial K})[\hat{u}]_{\partial K} = [g] + \sum_{K\in\mathcal{T}_h} \mathbb{A}_f^K. \tag{5.28}$$

Remark. The HDG method can be thought of as a DG method with fluxes defined as Equations (5.20–21) with choices of C_{11}, C_{12}, C_{22} depending on τ_+, τ_-.

The HDG method possesses many of the advantages of the related methods presented in this section, namely

- it is suitable for static condensation,
- it has optimal convergence in both the flux and the potential (unlike the LDG method which is suboptimal for the flux),
- optimal convergence is achieved with simple DG spaces, namely $\boldsymbol{V}(K) = [\mathcal{P}_k]^d$, $W(K) = \mathcal{P}_k(K)$, $M(e) = \mathcal{P}(e)$,
- it has superconvergence of order $k+2$ for the projection of the error in the trace variable, which then enables the construction of parallelized postprocesses to achieve higher order approximations.

For a thorough description of the implementation in MATLAB of this method for a 3D convection-diffusion-reaction equation, we refer the reader to [Fu et al., 2015], as well as [Du and Sayas, 2019] for a more in-detail overview of the theoretical aspects.

Chapter 6

The Transfer Path Method (TPM)

6.1 Introduction

The origins of the Transfer Path Method (TPM) date back to 2007 in the PhD thesis of Deepa Gupta and the work of Cockburn et al. [2009], where a one-dimensional boundary value problem was solved by means of transferring the boundary data of the potential to a subdomain via integration of the approximate flux; the d-dimensional extension of this technique was later covered by Cockburn and Solano [2012] to solve curved boundary problems in polygonal subdomains. This technique, at the beginning unnamed, was later applied to HDG-BEM coupling [Cockburn et al., 2012] and a number of HDG methods for curved-boundary problems such as Stokes flow [Solano and Vargas, 2019], the Grad-Shafranov equation in magnetohydrodynamics [Sánchez-Vizuet et al., 2020], the Oseen equations [Solano and Vargas M., 2022] and non-linear elliptic problems [Sánchez et al., 2022] and it is then in the work of Sánchez et al. [2022] that the method is referred to as the *Transfer Path Method* for the first time. Other applications of the method thereafter include shape optimization [Henríquez and Solano, 2024], linear elasticity [Cárdenas and Solano, 2024] and optimal control [Henríquez and Solano, 2026]. Note that, while the genesis of the method occured within the HDG community, and consequently much of its application has taken place therein, the TPM is *not* exclusive to HDG methods and can be applied to high-order mixed methods in general as seen in the work of Oyarzúa et al. [2019, 2020].

The core idea of the TPM is to transfer the exact boundary data of the discrete potential u_h into the polyhedral domain by quantifying its difference with the subdomain border via a linear form depending on an approximation of its gradient ∇u_h via the flux $\boldsymbol{q}_h$, which in a mixed method is part of the field unknowns of the problem. The method is essen-

tially a boundary value correction [Bramble et al., 1972], and maybe more precisely, an approximate domain method, as the physical domain is approximated by a different, more computationally-friendly domain and then the physical boundary values are incorporated by means of a correction term using a polynomial extension [Cheung et al., 2020] outside of the approximating domain and enforced on the computational boundary. Other approximating domain approaches can be found in [Dupont, 1974, Burman et al., 2017, Main and Scovazzi, 2018], all based on a Taylor expansion to account for the geometrical mismatch. In particular, we highlight the *Shifted Boundary Method* (SBM) introduced in [Main and Scovazzi, 2018] and subsequently developed for high order methods in [Atallah et al., 2022]. We note that the TPM and the SBM are spiritually similar, as both utilize similar geometrical constructions and rely on a mapping between the physical and computational boundaries (usually denoted by ψ in the TPM and $\boldsymbol{M}$ in the SBM) as well as extensions based on Taylor polynomials for the error analysis. However, the core difference is that the SBM casts the correction term in *differential* form, whereas the TPM uses an *integral* form.

6.2 The TPM for boundary value problems

Consider the HDG method for the diffusion equation in Problem 5.3.5 with $\mathbb{K} \equiv \mathbb{I}$ for $\Omega_h = \Omega$:

$$(\boldsymbol{q}_h, \boldsymbol{v}_h)_{\mathcal{T}_h} - (u_h, \nabla \cdot \boldsymbol{v}_h)_{\mathcal{T}_h} + \langle \hat{u}_h, \boldsymbol{v}_h \cdot \boldsymbol{\nu} \rangle_{\partial \mathcal{T}_h} = 0 \tag{6.1a}$$

$$(\nabla \cdot \boldsymbol{q}_h, w_h)_{\mathcal{T}_h} + \langle \tau(u_h - \hat{u}_h), w_h \rangle_{\partial \mathcal{T}_h} = (f, w_h)_{\mathcal{T}_h} \tag{6.1b}$$

$$\langle \boldsymbol{q}_h \cdot \boldsymbol{\nu} + \tau(u_h - \hat{u}_h), \mu_h \rangle_{\partial \mathcal{T}_h \setminus \Gamma} = 0 \tag{6.1c}$$

$$\langle \hat{u}_h, \mu_h \rangle_{\Gamma} = \langle g, \mu_h \rangle_{\Gamma} \tag{6.1d}$$

Now, if we have that $\Omega_h \subsetneq \Omega$, then Equation (6.1d) cannot be meaningfully realized since some parts of the discrete boundary $\partial\Omega_h =: \Gamma_h \neq \Gamma$ will be left without boundary conditions. It would then be desirable to replace Equation (6.1d) with something of the form

$$\langle \hat{u}_h, \mu_h \rangle_{\Gamma_h} = \langle \tilde{g}, \mu_h \rangle_{\Gamma_h}, \tag{6.2}$$

where $\tilde{g}$ could be interpreted as the *transferred* boundary datum.

To construct this transferred datum, we note that that the exact solution u satisfies

$$u(\boldsymbol{x}_h) = u(\boldsymbol{x}) + \int_{\boldsymbol{x}}^{\boldsymbol{x}_h} \nabla u \cdot \boldsymbol{m}, \qquad \boldsymbol{x} \in \Omega, \boldsymbol{x}_h \in \Gamma_h$$

with $\boldsymbol{m}$ the tangential unit vector along the segment $[\boldsymbol{x}_h, \boldsymbol{x}]$; see Figure 6.1. We can then

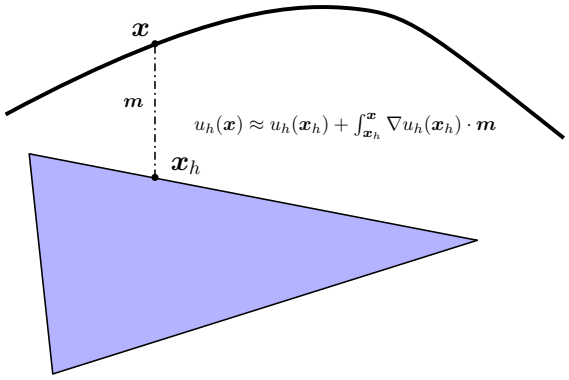

Figure 6.1: Illustration of a transfer path with unit vector $\boldsymbol{m}$

write

$$\hat{u}_h(\boldsymbol{x}_h) = \underbrace{g(\boldsymbol{x}) + \int_{\boldsymbol{x}_h}^{\boldsymbol{x}} \boldsymbol{E}(\boldsymbol{q}_h) \cdot \boldsymbol{m}}_{\tilde{g}}, \quad \boldsymbol{x} \in \Gamma, \boldsymbol{x} \in \Gamma_h \tag{6.3}$$

where $\boldsymbol{E}$ is the extension operator defined on [Cockburn and Solano, 2012]), which essentially sets

$$\boldsymbol{E}(\boldsymbol{v})(\boldsymbol{y}) = \boldsymbol{v}|_{K(\boldsymbol{y})}(\boldsymbol{y}), \qquad \forall \boldsymbol{v} \in \prod_{K \in \mathcal{T}_h} \mathcal{P}_k(K),$$

where $K(\boldsymbol{y})$ is, in simple words, an element that is sufficiently close to $\boldsymbol{y}$. Finally, in order to define a single-valued $\tilde{g}$ for each $\boldsymbol{x}_h \in \Gamma_h$, we fix a mapping $\psi : \Gamma_h \to \Gamma$ that assigns, for each point on the "discrete" point $\boldsymbol{x}_h \in \Gamma_h$, a unique "physical" point $\boldsymbol{x} \in \Gamma$.

Remark. Since $\boldsymbol{x}_h$ belongs to the mesh boundary, as long as it is not a mesh vertex, it will belong to a unique element K. Utilizing Gauss–Legendre quadrature rules which let us avoid vertices, we can set K to be $K(\boldsymbol{x}) = K(\psi(\boldsymbol{x}_h))$. Note that, as seen in [Cockburn and Solano, 2012], the "proper procedure" is to define, for each boundary face e, an extrapolation patch $K^e_{\text{ext}} \subset \overline{\Omega} \setminus \Omega_h$ such that their union forms a partition $\overline{\Omega} \setminus \Omega_h$. Then, for $\boldsymbol{y} \in K^e_{\text{ext}}$, we set $K(\boldsymbol{y}) = K$ where $\partial K \ni e$.

Remark. We will henceforth assume that ψ is bijective; however, in practical applications, the mapping does not have to be neither injective nor surjective (this is the case when the physical boundary has been sampled with a fixed number of measurements and then one assigns discrete points to the measured point which is closest in distance).

We can now rewrite Equation (6.2) as

$$\langle T_{\Gamma \to \Gamma_h}(\hat{u}_h, \boldsymbol{q}_h), \mu_h \rangle_{\Gamma_h} = \langle g \circ \psi, \mu_h \rangle_{\Gamma_h}$$

where

$$T_{\Gamma\to\Gamma_h}(\hat{u}_h, \boldsymbol{q}_h)(\boldsymbol{x}_h) \coloneqq T(\hat{u}_h, -\boldsymbol{q}_h)(\boldsymbol{x}_h; \psi(\boldsymbol{x}_h)), \qquad \forall \boldsymbol{x}_h \in \Gamma_h, \tag{6.4}$$

and

$$T(\mu, \boldsymbol{v})(\boldsymbol{x}_h; \boldsymbol{y}_h) \coloneqq \mu(\boldsymbol{x}_h) + \int_{\boldsymbol{x}_h}^{\boldsymbol{y}_h} \boldsymbol{E}(\boldsymbol{v}) \cdot \boldsymbol{m}, \qquad \boldsymbol{x}_h \in e \subset \Gamma_h,\ \boldsymbol{y}_h \in K^e_{\text{ext}}, \tag{6.5}$$

is the *transfer* along the *path* $[\boldsymbol{x}_h, \boldsymbol{y}_h]$.

Remark. Note that, if ψ is bijective, we can write

$$T_{\Gamma_h\to\Gamma}(\mu, \boldsymbol{v})(\boldsymbol{x}) \coloneqq T(\psi^{-1}(\boldsymbol{x}); \boldsymbol{x}), \qquad \forall \boldsymbol{x} \in \Gamma. \tag{6.6}$$

and the rewriting of Equation (6.2) would now be

$$\langle T_{\Gamma_h\to\Gamma}(\hat{u}_h, \boldsymbol{q}_h), \mu_h \circ \psi^{-1}\rangle_\Gamma = \langle g, \mu_h \circ \psi^{-1}\rangle_\Gamma.$$

With this, we mean to highlight that the procedure can be understood as either a transferring of the boundary datum *inwards* towards the discrete boundary, or of the discrete solution *outwards* towards the physical boundary, followed by a reparametrization back to the discrete boundary (in order to apply quadrature rules to approximate the integral forms). This second perspective becomes relevant when dealing with the the Stokes/Darcy problem.

In terms of matrices, the original system is

$$\begin{pmatrix} \mathbb{M}_h & -\mathbb{C}_h^{\mathsf{t}} & \mathbb{F}_{\boldsymbol{\nu}}^{\mathsf{t}} \\ -\mathbb{C}_h^{\mathsf{t}} & \mathbb{M}_{\partial,\tau} & \tau\mathbb{F}^{\mathsf{t}} \\ \mathbb{F}_{\boldsymbol{\nu}} & \tau\mathbb{F} & \tau\widetilde{\mathbb{F}} + \widetilde{\mathbb{M}} \end{pmatrix} \begin{pmatrix} [\boldsymbol{q}_h] \\ [u_h] \\ [\widehat{u}_h] \end{pmatrix} = \begin{pmatrix} 0 \\ [f] \\ [g] \end{pmatrix},$$

and the modified TPM system is

$$\begin{pmatrix} \mathbb{M}_h & -\mathbb{C}_h^{\mathsf{t}} & \mathbb{F}_{\boldsymbol{\nu}}^{\mathsf{t}} \\ -\mathbb{C}_h^{\mathsf{t}} & \mathbb{M}_{\partial,\tau} & \tau\mathbb{F}^{\mathsf{t}} \\ \mathbb{F}_{\boldsymbol{\nu}} + \mathbb{T}_{\boldsymbol{q}} & \tau\mathbb{F} & \tau\widetilde{\mathbb{F}} + \widetilde{\mathbb{M}} \end{pmatrix} \begin{pmatrix} [\boldsymbol{q}_h] \\ [u_h] \\ [\widehat{u}_h] \end{pmatrix} = \begin{pmatrix} 0 \\ [f] \\ [g] \end{pmatrix}$$

where the inclusion of the transfer term amounted to an additional bilinear form acting on $\boldsymbol{q}$ and the test functions localized on the boundary. An example solution can be found in Figure 6.2 for a Poisson problem with Dirichlet boundary conditions on the kidney-shaped domain given by the set $\{\phi < 0\}$, where

$$\phi(\boldsymbol{x}) = \left(\frac{3}{2}\left((x_1 + a)^2 + x_2^2\right) - x_1 - a\right)^2 - (x_1 + a)^2 - x_2^2 + b,$$

with $a = \frac{1}{2}$, $b = \frac{1}{10}$. The source term and boundary data are obtained from the manufactured solution $u = \sin(\pi x)\sin(\pi y)$.

Remark. If we fix the linear operators and the source term f, then we can think of the solution operator given Dirichlet boundary data as a left-inverse of the trace operator γ_0, and so applying the TPM is essentially asking that the diagram in Figure 6.3 commutes.

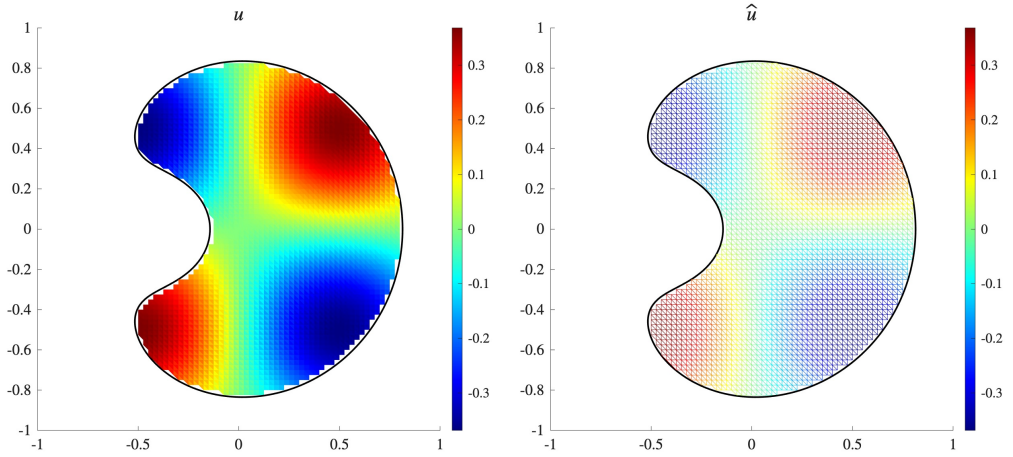

Figure 6.2: Plots of u_h and $\hat{u}_h$ using $\mathcal{P}_1$ elements. The mesh was obtained by using a structured background mesh and then selecting all the elements that were contained in the interior of the kidneys-shaped domain.

$$
\begin{array}{ccc}
\Gamma & \xleftarrow{\psi} & \Gamma_h \\
H^1(\Omega) & \xrightarrow{\gamma_0} & H^{1/2}(\Gamma) \\
\boldsymbol{R} \downarrow & & \uparrow \boldsymbol{T} \\
H^1(\Omega_h) & \xrightarrow{\gamma_0} & H^{1/2}(\Gamma_h)
\end{array}
$$

Figure 6.3: Diagram representing the procedure of solving a boundary-value problem via a surrogate domain $\Omega_h \subset \Omega$. Instead of directly going from exact boundary data $g \in H^{\frac{1}{2}}(\Gamma)$, one transfers to the surrogate boundary Γ_h, solves on the corresponding subdomain and then extends to the full domain. Here $\boldsymbol{R}$ is the restriction operator, acting as the left-inverse of the extension operator $\boldsymbol{E}$.

6.3 The TPM for interface and transmission problems

In this section, we present a brief overview of the interface problems for which the TPM has been applied thus far. In the first part, we deal with *piecewise-flat* interfaces, in which we approach two transmission problems with non-matching interfaces as well as a multiphysics problem in which coupling conditions are prescribed on a physical interface. In the second, we drop the piecewise-flat assumptions and allow the interface to be curved.

6.3.1 Piecewise-flat interfaces

The problems treated here were more exploratory in nature, as they were among the first works applying the TPM to interface problems. In line with the work of [Solano et al., 2022], we simplify the geometry and work with piecewise-flat discrete interfaces such that their normal exterior vectors are parallel to each other, and possibly to a third straight segment (playing the role of the exact interface); see Figure 6.4. Our aim is to study the transferring technique in the context of interface problems without having to take into account conformity of the normal exterior vectors, as they have been known to place more severe restrictions on the geometry as is the case of Neumann boundary conditions treated with TPM.

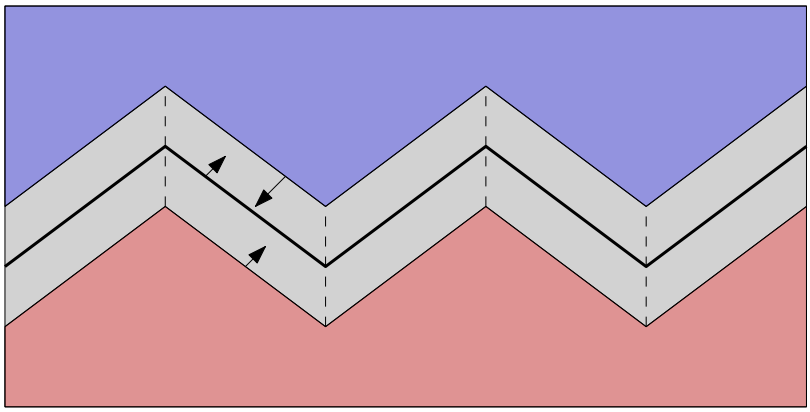

Figure 6.4: On each section delimited by the dashed lines, both the red and blue domains have parallel interfaces, and these are parallel to the black line in the middle (representing an eventual physical interface).

Two transmission problems at a distance

Let $\Omega \subset \mathbb{R}^n$ be a domain. We start with the diffusion problem on Ω with $\mathbb{K} = \mathbb{I}$ and $c_0 \equiv 0$; see Problem 5.3.1. This problem was treated in [Solano et al., 2022] and optimal convergence was shown to be attained when the distance between discrete interfaces was of order $\mathcal{O}(h^2)$.

We will consider two polygonal subdomains $\Omega_{\mathrm{L}}, \Omega_{\mathrm{R}} \subset \Omega$ with $\operatorname{dist}(\Omega_{\mathrm{L}}, \Omega_{\mathrm{R}}) > 0$ such that $\Sigma_{\mathrm{L}} := \partial\Omega \setminus \partial\Omega_{\mathrm{L}}$ and $\Sigma_{\mathrm{R}} := \partial\Omega \setminus \partial\Omega_{\mathrm{R}}$ are piecewise-flat curves parallel to each

other; see Figure 6.5. Since each subdomain is polygonal, we can easily construct fitted meshes $\mathcal{T}_{h,\mathrm{L}}$ and $\mathcal{T}_{h,\mathrm{R}}$.

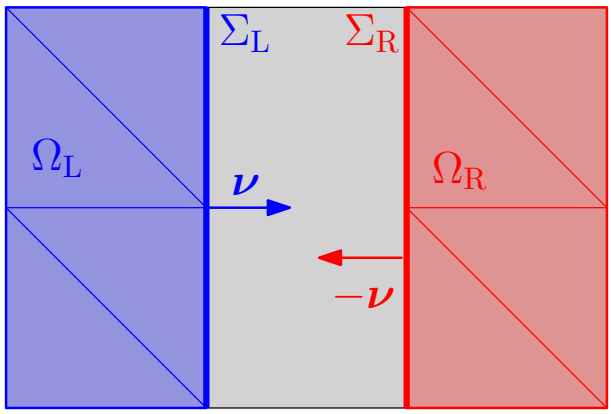

Figure 6.5: Domains with completely flat interfaces. The subdomains are separated by a gap of size $\delta > 0$.

For $\star \in \{\mathrm{L}, \mathrm{R}\}$, the diffusion equation holds and so we have Equations (5.23a–b) with $\mathcal{T}_h = \mathcal{T}_{h,\star}$. However, Equation (5.23c) only holds on $\partial\mathcal{T}_{h,\star} \setminus \Sigma_\star$. For the conditions on the discrete interface, say Σ_L, we note that this poses a transmission problem in the partition Ω_L, $\Omega \setminus \Omega_\mathrm{L}$. However, we do not have an approximation for the value on the side of Σ_L pointing to $\Omega \setminus \Omega_\mathrm{L}$. Therefore, we use the TPM to extend from the subdomain $\Omega_\mathrm{R} \subset \Omega \setminus \Omega_\mathrm{L}$ to Σ_L and solve the transmission problem. This procedure will also automatically give us boundary conditions for Ω_R, closing the system on that end as well. For symmetry, we enforce one transmission condition each (see the remark under Problem 5.3.5) on each discrete interface.

The resulting transmission conditions are

$$\begin{aligned}
\langle T_{\mathrm{L}\to\mathrm{R}}(\hat{u}_{\mathrm{L},h}, -\boldsymbol{q}_{\mathrm{L},h}) - \hat{u}_{\mathrm{R},h}, \mu_{\Sigma_{\mathrm{R},h}}\rangle_{\Sigma_{\mathrm{R},h}} &= 0, \\
\langle \widehat{\boldsymbol{q}_{\mathrm{L},h} \cdot \boldsymbol{\nu}} - T_{\mathrm{R}\to\mathrm{L}}(\boldsymbol{q}_{\mathrm{R},h} \cdot \boldsymbol{\nu}, u_{\mathrm{R},h}, \hat{u}_{\mathrm{R},h}), \mu_{\Sigma_{\mathrm{L}},h}\rangle_{\Sigma_{\mathrm{L}},h} &= 0,
\end{aligned}$$

where, given a bijective mapping between discrete interfaces so that each $\boldsymbol{x}_\mathrm{L} \in \Sigma_{\mathrm{L},h}$ is assigned a unique $\boldsymbol{x}_\mathrm{R} \in \Sigma_{\mathrm{R},h}$, we have

$$\begin{aligned}
T_{\mathrm{L}\to\mathrm{R}}(\mu, \boldsymbol{v})(\boldsymbol{x}_\mathrm{R}) &:= T(\mu, \boldsymbol{v})(\boldsymbol{x}_\mathrm{L}; \boldsymbol{x}_\mathrm{R}), \\
T_{\mathrm{R}\to\mathrm{L}}(\boldsymbol{v}\cdot\boldsymbol{\nu}, w, \mu)(\boldsymbol{x}_\mathrm{L}) &:= \boldsymbol{E}(\boldsymbol{v}\cdot\boldsymbol{\nu})(\boldsymbol{x}_\mathrm{L}) + \tau\left(T(w, \boldsymbol{v})(\boldsymbol{x}_\mathrm{R}; \boldsymbol{x}_\mathrm{L}) - T(\mu, \boldsymbol{v})(\boldsymbol{x}_\mathrm{R}; \boldsymbol{x}_\mathrm{L})\right), \\
&= \boldsymbol{E}(\boldsymbol{v}\cdot\boldsymbol{\nu})(\boldsymbol{x}_\mathrm{L}) + \tau(w(\boldsymbol{x}_\mathrm{R}) - \mu(\boldsymbol{x}_\mathrm{R})),
\end{aligned}$$

where T and $\boldsymbol{E}$ are defined as in Section 6.2.

We can also apply this method to a slightly more involved problem, the Stokes problem. This corresponds to the contents of Paper IV, where optimal convergence was shown for gaps of order $\mathcal{O}(h^2)$. We consider the same geometry as before and skip the equations of the HDG method for the sake of brevity.

For $\star \in \{\mathrm{R}, \mathrm{L}\}$, we search for approximations $\boldsymbol{u}_{\star,h} = \boldsymbol{u}|_{\Omega_\star}$, $\mathbb{L}_{\star,h} = \mathbb{L}|_{\Omega_\star}$ and $p_{\star,h} = p|_{\Omega_\star}$ of the continuous velocity $\boldsymbol{u}_\star$, velocity gradient $\mathbb{L}_\star$ and pressure $p_\star$ fields satisfying

$$\begin{aligned} \mathbb{L} - \nabla \boldsymbol{u} &= 0 \qquad && \text{on } \Omega, \\ -\nabla \cdot (\mu \mathbb{L} - p\mathbb{I}) &= \boldsymbol{f}, && \text{on } \Omega, \\ \int_\Omega p &= 0 \end{aligned}$$

together with source terms $\boldsymbol{f}$ and Dirichlet or Neumann boundary conditions prescribed on $\partial\Omega$.

The transmission problem associated to a co-dimension 1 hypersurface Σ with outwards unit normal $\boldsymbol{\nu}_\Sigma$,

$$\begin{aligned} \boldsymbol{u}_\mathrm{L} - \boldsymbol{u}_\mathrm{R} &= 0, && \text{on } \Sigma, \\ (-\mu\mathbb{L}_\mathrm{L} + p_\mathrm{L}\mathbb{I})\boldsymbol{\nu} - (-\mu\mathbb{L}_\mathrm{R} + p_\mathrm{R}\mathbb{I})\boldsymbol{\nu} &= 0, && \text{on } \Sigma, \end{aligned}$$

corresponding to the continuities of the velocity trace and the stress normal trace. The resulting transferred transmission conditions are

$$\begin{aligned} \langle T_{\mathrm{L}\to\mathrm{R}}(\hat{\boldsymbol{u}}_{\mathrm{L},h}, \mathbb{L}_{\mathrm{L},h}) - \hat{\boldsymbol{u}}_{\mathrm{R},h}, \mu_{\Sigma_\mathrm{R},h}\rangle_{\Sigma_{\mathrm{R},h}} &= 0 \\ \langle (-\mu\mathbb{L}_{\mathrm{L},h}\boldsymbol{\nu} + \tilde{p}_{\mathrm{L},h}\boldsymbol{\nu})_{\mathrm{L},h} + \tau(\boldsymbol{u}_{\mathrm{L},h} - \hat{\boldsymbol{u}}_{\mathrm{L},h}) - T_{\mathrm{R}\to\mathrm{L}}(\mathbb{L}_{\mathrm{R},h}, \tilde{p}_{\mathrm{R},h}, \hat{u}_{\mathrm{R},h}), \mu_{\Sigma_\mathrm{L},h}\rangle_{\Sigma_{\mathrm{L},h}} &= 0 \end{aligned}$$

where we have introduced approximations $\tilde{p}_{\star,h}$, $\star \in \{\mathrm{L}, \mathrm{R}\}$, of the *shifted* pressures $\tilde{p}_\star$ defined to sum to zero mean on the union of the computational subdomains. It differs with the exact pressures $p_\star$ (which sum to zero mean on the exact domain) by a constant which is later computed via a postprocessing.

The operators $T_{\mathrm{L}\to\mathrm{R}}$ and $T_{\mathrm{R}\to\mathrm{L}}$ are constructed in the same way as for the diffusion problem, with the modification that $\mathbb{L}_{\mathrm{L},h}\boldsymbol{m}$ takes the role of $-\boldsymbol{q}_{\mathrm{L},h} \cdot \boldsymbol{m}$ in $T_{\mathrm{L}\to\mathrm{R}}$ and $(-\mu\mathbb{L}_{\mathrm{R},h} + \tilde{p}_{\mathrm{R},h})\boldsymbol{\nu}$ takes the role of $\boldsymbol{q}_{\mathrm{R},h} \cdot \boldsymbol{\nu}$ in $T_{\mathrm{R}\to\mathrm{L}}$.

An interface problem: the Stokes/Darcy coupling

This corresponds to the contents of Paper V, where optimal convergence was shown for semi-aligned flat interfaces with gaps of order $\mathcal{O}(h^{1+\frac{3}{4}})$. We consider a domain Ω with separated subdomains as before, but they are now labelled Ω_S and Ω_D for clarity.

Since the interface separates the domain into two subdomains with different systems of governing PDEs, we cannot directly construct a transfer operator from one interface to the other. Instead, we apply the transmission conditions on the physical interface by transferring the traces, and then map back onto the discrete interfaces via the parametrization mapping; see Figure 6.6.

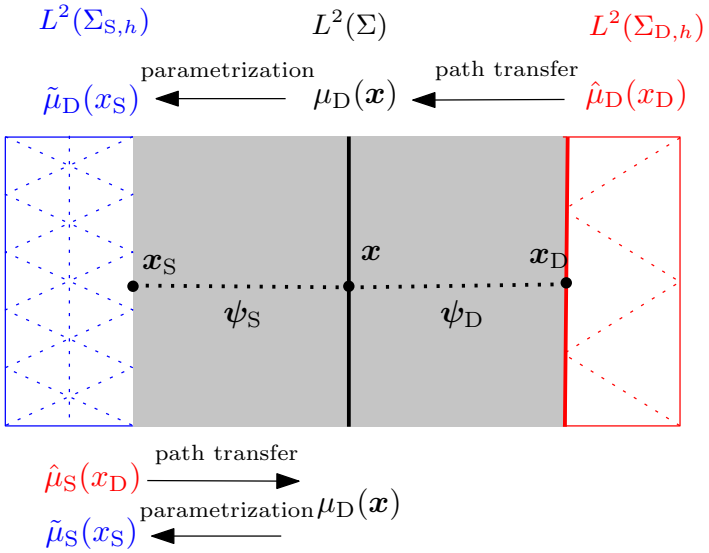

Figure 6.6: Each discrete interface $\Sigma_{\star,h}$ is mapped to the exact interface Σ via an invertible mapping $\boldsymbol{\psi}_\star : \Sigma \to \Sigma_{\star,h}$. Here, fields μ_{D} and μ_{S} are transferred to the physical interface Σ where a coupling condition is enforced, followed by a parametrization (in the case of the figure, to $\Sigma_{\mathrm{S},h}$) in order to implement the coupling on one of the meshes.

Defining the stress tensors

$$\mathbb{S}_{\mathrm{S}} \coloneqq -\nu_{\mathrm{S}}\mathbb{L}_{\mathrm{S}} + p_{\mathrm{S}}\mathbb{I}, \qquad \mathbb{S}_{\mathrm{D}} \coloneqq p_{\mathrm{D}}\mathbb{I},$$

the exact coupling conditions are

$$\begin{aligned} (\boldsymbol{u}_{\mathrm{S}} \cdot \boldsymbol{\nu} - \boldsymbol{u}_{\mathrm{D}}) \cdot \boldsymbol{\nu} &= 0 && \text{on } \Sigma, \\ \mathbb{S}_{\mathrm{S}}\boldsymbol{\nu} + \omega(\boldsymbol{u}_{\mathrm{S}}, \boldsymbol{\nu}) &= \mathbb{S}_{\mathrm{D}}\boldsymbol{\nu} && \text{on } \Sigma, \end{aligned}$$

where

$$\omega(\boldsymbol{v}, \boldsymbol{\xi}) \coloneqq \sum_{i=1}^{n-1} \omega_i (\boldsymbol{v} \cdot \boldsymbol{\xi}_i^{\perp}) \boldsymbol{\xi}_i^{\perp}$$

with $\omega_1, \dots, \omega_{n-1} > 0$ a set of frictional constants and $\boldsymbol{\xi}_1^{\perp}, \dots, \boldsymbol{\xi}_{n-1}^{\perp}$ is a set of tangential unit vectors to the hypersurface with unit normal $\boldsymbol{\nu}$. These conditions correspond to

the balance of mass and of forces across the interface, the latter taking into account frictional forces using the Beavers–Joseph–Saffman law; the corresponding discrete transferred conditions are

$$\begin{aligned}\langle \psi_{\mathrm{D}} \circ \left(\tilde{\boldsymbol{u}}_{\mathrm{S},h} \cdot \boldsymbol{\nu} - \widetilde{\boldsymbol{u}_{\mathrm{D},h} \cdot \boldsymbol{\nu}}\right), \mu_{\mathrm{D,h}} \rangle_{\Sigma_{\mathrm{D},h}} &= 0, \\ \langle \psi_{\mathrm{S}} \circ \left(\widetilde{\mathbb{S}_{\mathrm{S},h}\boldsymbol{\nu}} + \omega(\tilde{\boldsymbol{u}}_{\mathrm{S},h}, \boldsymbol{\nu}) - \widetilde{\mathbb{S}_{\mathrm{D},h}\boldsymbol{\nu}}\right), \mu_{\mathrm{S,h}} \rangle_{\Sigma_{\mathrm{S},h}} &= 0,\end{aligned}$$

where

$$\begin{aligned}\tilde{\boldsymbol{u}}_{\mathrm{S},h} &\coloneqq T^{\boldsymbol{u}}_{\mathrm{S}\to\Sigma}(\hat{\boldsymbol{u}}_{\mathrm{L},h}, \mathbb{L}_{\mathrm{S},h}) \\ \widetilde{\boldsymbol{u}_{\mathrm{D},h} \cdot \boldsymbol{\nu}} &\coloneqq T^{\boldsymbol{u}}_{\mathrm{D}\to\Sigma}(\boldsymbol{u}_{\mathrm{R},h} \cdot \boldsymbol{\nu}, p_{\mathrm{R},h}, \hat{p}_{\mathrm{R},h}) \\ \widetilde{\mathbb{S}_{\mathrm{S},h}\boldsymbol{\nu}} &\coloneqq T^{\mathbb{S}}_{\mathrm{S}\to\Sigma}(\mathbb{S}_{\mathrm{L},h}\boldsymbol{\nu}, \boldsymbol{u}_{\mathrm{S,h}}, \hat{\boldsymbol{u}}_{\mathrm{S,h}}) + \alpha_h \\ \widetilde{\mathbb{S}_{\mathrm{D},h}} &\coloneqq T^{\mathbb{S}}_{\mathrm{D}\to\Sigma}(\hat{p}_{\mathrm{R},h}, -\boldsymbol{u}_{\mathrm{R},h})\end{aligned}$$

and α_h is an approximation of the pressure outside the computational subdomain acting as an additional forcing term on the interface. This extrapolated pressure appears since we also perform a pressure shift on the Stokes subdomain, but in this case cannot be obtained in a postprocess due to its role in the momentum balance.

Let $\boldsymbol{x} = \psi_{\mathrm{S}}^{-1}(\boldsymbol{x}_{\mathrm{S}}) = \psi_{\mathrm{D}}^{-1}(\boldsymbol{x}_{\mathrm{D}})$. Then, the transfer operators are

$$\begin{aligned}T^{\boldsymbol{u}}_{\mathrm{S}\to\Sigma}(\mu, \mathbb{G})(\boldsymbol{x}) &\coloneqq T(\mu, \mathbb{G})(\boldsymbol{x}_{\mathrm{S}}; \boldsymbol{x}) \\ T^{\boldsymbol{u}}_{\mathrm{D}\to\Sigma}(\boldsymbol{v} \cdot \boldsymbol{\nu}, w, \mu) &\coloneqq \boldsymbol{E}(\boldsymbol{v} \cdot \boldsymbol{\nu})(\boldsymbol{x}) + \tau(w(\boldsymbol{x}_{\mathrm{D}}) - \mu(\boldsymbol{x}_{\mathrm{D}})) \\ T^{\mathbb{S}}_{\mathrm{S}\to\Sigma}(\mathbb{G}\boldsymbol{\nu}, \boldsymbol{w}, \mu) &\coloneqq \boldsymbol{E}(\mathbb{G}\boldsymbol{\nu})(\boldsymbol{x}) + \tau(\boldsymbol{w}(\boldsymbol{x}_{\mathrm{S}}) - \mu(\boldsymbol{x}_{\mathrm{S}})) \\ T^{\mathbb{S}}_{\mathrm{D}\to\Sigma}(\mu, \boldsymbol{v}) &\coloneqq T(\mu, \boldsymbol{v})(\boldsymbol{x}_{\mathrm{D}}; \boldsymbol{x})\end{aligned}$$

Numerical results can be seen in Figure 6.7 for $\Sigma = \{\boldsymbol{x}_2 = 0.5\}$, $\mathbb{K} = \mathbb{I}$, $\mu = \omega = 1$ and the manufactured solution

$$\begin{aligned}\boldsymbol{u}_{\mathrm{S}}(\boldsymbol{x}) &= \begin{pmatrix} \pi \sin(\pi x_1) \sin(\pi x_2) \\ \pi \cos(\pi x_1) \cos(\pi x_2) \end{pmatrix}, \\ p_0(\boldsymbol{x}) &= \exp((x_1 - 0.5)^2 + (x_2 - 0.5)^2), \\ p_{\mathrm{S}}(\boldsymbol{x}) &= p_0(\boldsymbol{x}) - 2 \int_0^1 \int_{0.5}^1 p_0(\boldsymbol{y}) \, \mathrm{d}y_1 \mathrm{d}y_2, \\ p_{\mathrm{D}}(\boldsymbol{x}) &= \sin(\pi((x_1 - 0.5)^2 + (x_2 - 0.5)^2)).\end{aligned}$$

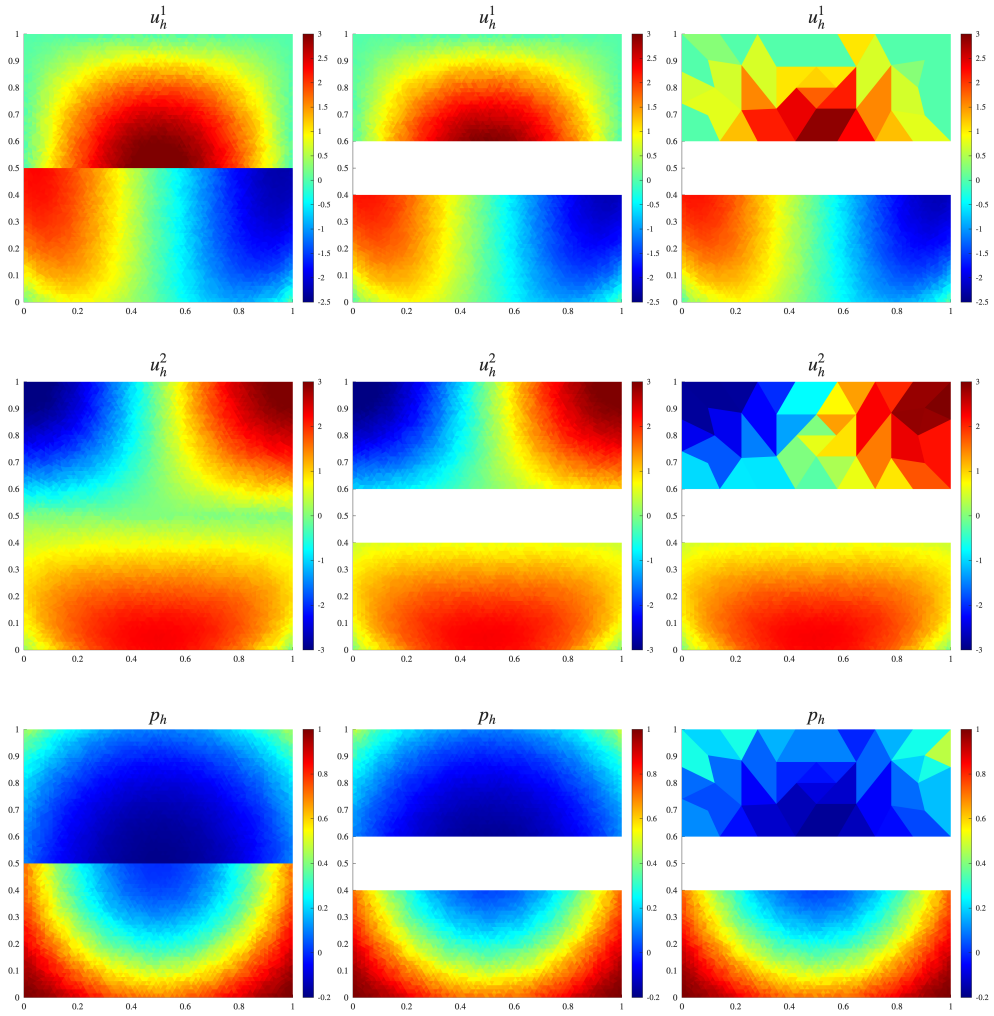

Figure 6.7: Plots of $\boldsymbol{u}_h$ and p_h with $\mathcal{P}_4$ elements and no gap (left), gap (middle) and gap with hanging nodes (right). The subdomains are $\Omega_S = [0,1] \times [0.5,1]$ and $\Omega_D = [0,1] \times [0,0.5]$.

6.3.2 Curved interfaces

The contents of this section correspond to ongoing work with Isaac Bermúdez and Manuel Solano.

We are interested in a linear model of fluid-structure interaction in which the fluid is modelled using Stokes flow and the structure is a linear ellastic solid. To achieve a symmetry between the formulations, we utilize a stress-velocity formulation for the Stokes flow instead of the velocity-pressure form used in Paper v. Furthermore, we will drop the assumption of

piecewise-flat interfaces and distinguish between the unit exterior vectors of the meshes $\boldsymbol{\nu}_\star^h$ and of the physical interface $\boldsymbol{\nu}_\Sigma$, the latter pointing from the domain of the fluid towards the domain of the solid.

The governing equations for both the fluid and structure are

$$\rho_{\mathrm{f}}\partial_t \boldsymbol{u}_{\mathrm{f}} - \nabla\cdot\mathbb{S}_{\mathrm{f}} = \boldsymbol{b}_{\mathrm{f}} \tag{6.9}$$
$$\rho_{\mathrm{s}}\partial_{tt} \boldsymbol{u}_{\mathrm{s}} - \nabla\cdot\mathbb{S}_{\mathrm{s}} = \boldsymbol{b}_{\mathrm{s}} \tag{6.10}$$

where $\rho_\star$, $\mathbb{S}_\star$ and $\boldsymbol{b}_\star$ are the density, stress tensor and body forces corresponding to the the fluid ($\star = \mathrm{f}$) and the solid ($\star = \mathrm{s}$). Note that $\boldsymbol{u}_{\mathrm{f}}$ is the *velocity* (with units of length over time) of the fluid, whereas $\boldsymbol{u}_{\mathrm{s}}$ is the *displacement* (with unit of length). The constitutive laws for each material are

$$\mathbb{S}_{\mathrm{f}} - \frac{1}{n}\operatorname{tr}(\mathbb{S}_{\mathrm{f}})\mathbb{I} = 2\mu_{\mathrm{f}}\mathbb{E}(\boldsymbol{u}_{\mathrm{f}}), \tag{6.11}$$
$$\mathbb{S}_{\mathrm{s}} = 2\mu_{\mathrm{s}}\mathbb{E}(\boldsymbol{u}_{\mathrm{s}}) + \lambda_{\mathrm{s}}\operatorname{tr}(\mathbb{E}(\boldsymbol{u}_{\mathrm{s}}))\mathbb{I}, \tag{6.12}$$

where μ_{f} is the dynamic viscosity of the fluid, and μ_{s}, λ_{s} are the Lamé parameters of the solid.

Using operators $\mathcal{A}_\star$, $\star \in \{\mathrm{f}, \mathrm{s}\}$ acting on the stress tensors and the fact that

$$\nabla\boldsymbol{u} = \mathbb{E}(\boldsymbol{u}) + \mathbb{G}(\boldsymbol{u}),$$

where $\mathbb{G}$ is the anti-symmetric part of the gradient (referred to as the *linear rotation tensor* in the case of displacement and the *vorticity tensor* in the case of motion), we can rewrite Equations (6.11) and (6.12)

$$\mathcal{A}_\star(\mathbb{S}_\star) = \nabla\boldsymbol{u}_{\mathrm{f}} - \mathbb{G}_\star,$$

where $\mathbb{G}_\star := \mathbb{G}(\boldsymbol{u}_\star)$ and

$$\mathcal{A}_{\mathrm{f}}(\mathbb{S}) := \frac{1}{2\mu_f}\left(\mathbb{S} - \frac{1}{n}\operatorname{tr}(\mathbb{S})\mathbb{I}\right),$$
$$\mathcal{A}_{\mathrm{s}}(\mathbb{S}) := \frac{1}{2\mu_2}\left(\mathbb{S} - \frac{\lambda_{\mathrm{s}}}{n\lambda_{\mathrm{s}} + 2\mu_{\mathrm{s}}}\operatorname{tr}(\mathbb{S})\mathbb{I}\right).$$

At the interface Σ, the coupling conditions at the interface are the no-slip condition

$$\boldsymbol{u}_{\mathrm{s}} - \partial_t \boldsymbol{u}_{\mathrm{s}} = 0, \tag{6.13}$$

and the balance of forces

$$\boldsymbol{\sigma}_{\mathrm{f}}\boldsymbol{\nu}_\Sigma - \boldsymbol{\sigma}_{\mathrm{s}}\boldsymbol{\nu}_\Sigma = 0. \tag{6.14}$$

Putting everything together, we have the time-dependent fluid-structure interaction equations:

$$\mathcal{A}_\star(\mathbb{S}_\star) - \nabla \boldsymbol{u}_\star + \mathbb{G}_\star = \boldsymbol{0} \quad \text{in} \quad \Omega_\star, \quad \star \in \{\mathrm{f}, \mathrm{s}\}, \tag{6.15a}$$

$$\rho_\mathrm{f} \partial_t \boldsymbol{u}_\mathrm{f} - \nabla \cdot \mathbb{S}_\mathrm{f} = \boldsymbol{b}_\mathrm{f} \quad \text{in} \quad \Omega_\mathrm{f}, \tag{6.15b}$$

$$\rho_\mathrm{s} \partial_{tt} \boldsymbol{u}_\mathrm{s} - \nabla \cdot \mathbb{S}_\mathrm{s} = \boldsymbol{b}_\mathrm{s} \quad \text{in} \quad \Omega_\mathrm{s}, \tag{6.15c}$$

$$\frac{\partial \boldsymbol{u}_\mathrm{s}}{\partial t} - \boldsymbol{u}_\mathrm{f} = \boldsymbol{0} \quad \text{on} \quad \Sigma, \tag{6.15d}$$

$$\mathbb{S}_\mathrm{s} \boldsymbol{\nu}_\mathrm{s} + \mathbb{S}_\mathrm{f} \boldsymbol{\nu}_\mathrm{f} = \boldsymbol{0} \quad \text{on} \quad \Sigma. \tag{6.15e}$$

where, for $i \in \{\mathrm{f}, \mathrm{s}\}$, we have introduced the corresponding density ρ_i and body force $\boldsymbol{b}_i$. For simplicity, we close the system with null Dirichlet boundary conditions on both domains.

Time discretization

Equations involving first-order time derivatives, such as the fluid governing equation and the no-slip condition, can be cast in the form

$$\frac{\partial \boldsymbol{u}}{\partial t} = \boldsymbol{F}(t, \boldsymbol{u}).$$

and discretized by the backward Euler method

$$\frac{\boldsymbol{u}^{n+1} - \boldsymbol{u}^n}{\Delta t} = \boldsymbol{F}(t^{n+1}, \boldsymbol{u}^{n+1}), \tag{6.16}$$

where the superscripts n and $n+1$ represent approximations of the continuous fields at times t^n and $t^{n+1} := t^n + \Delta t$. For the governing equation of the solid, we have an equation involving second-order time derivatives of the form

$$\frac{\partial^2 \boldsymbol{u}}{\partial t^2} = \boldsymbol{G}(\boldsymbol{u}).$$

and a discretization can be obtained using the Newmark method [Quarteroni et al., 2019, Newmark, 1959] with $\gamma = \frac{1}{2}$, $\beta = \frac{1}{4}$,

$$\frac{4\boldsymbol{u}^{n+1} - 4\boldsymbol{u}^n}{\Delta t^2} - \left(\frac{4\boldsymbol{v}^n}{\Delta t} + \boldsymbol{a}^n \right) = \boldsymbol{G}(t^{n+1}, \boldsymbol{u}^{n+1}) \tag{6.17a}$$

$$\frac{1}{2} \left(\boldsymbol{v}^{n+1} + \boldsymbol{v}^n \right) = \frac{\boldsymbol{u}^{n+1} - \boldsymbol{u}^n}{\Delta t} \tag{6.17b}$$

$$\frac{1}{4} \left(\boldsymbol{a}^{n+1} + \boldsymbol{a}^n \right) = \frac{\boldsymbol{u}^{n+1} - \boldsymbol{u}^n}{\Delta t} - \frac{\boldsymbol{v}^n}{\Delta t} \tag{6.17c}$$

where, in the context of structural dynamics, $\boldsymbol{v}^n$ and $\boldsymbol{a}^n$ are approximations of the velocity and acceleration of the solid, respectively. Note that $\boldsymbol{G}$ does not depend on neither $\boldsymbol{v}^{n+1}$ nor $\boldsymbol{a}^{n+1}$, and so (6.17a) can be solved independently and then the values of $\boldsymbol{v}^{n+1}$ and $\boldsymbol{a}^{n+1}$ can be obtained from $\boldsymbol{u}^{n+1}$.

Utilizing time discretizations (6.16) and (6.17) on (6.15), replacing the susbcript n with 0 and removing the subscript $n+1$ altogether, we obtain, for $\star \in \{\mathrm{f}, \mathrm{s}\}$,

$$\mathcal{A}_\star(\mathbb{S}_\star) - (\nabla \boldsymbol{u}_\star - \mathbb{G}_\star) = \boldsymbol{0} \quad \text{in} \quad \Omega_\star, \tag{6.18a}$$

$$-\nabla \cdot \mathbb{S}_\star + \beta_\star \boldsymbol{u}_\star = \boldsymbol{f}_\star \quad \text{in} \quad \Omega_\star, \tag{6.18b}$$

$$\alpha_\mathrm{s} \boldsymbol{u}_\mathrm{s} - \alpha_\mathrm{f} \boldsymbol{u}_\mathrm{f} = \boldsymbol{g}_\Sigma \quad \text{on} \quad \Sigma, \tag{6.18c}$$

$$\mathbb{S}_\mathrm{s} \boldsymbol{\nu}_\mathrm{s} + \mathbb{S}_\mathrm{f} \boldsymbol{\nu}_\mathrm{f} = \boldsymbol{0} \quad \text{on} \quad \Sigma. \tag{6.18d}$$

where

$$\beta_\mathrm{f} = \frac{\rho_\mathrm{f}}{\Delta t}, \qquad \boldsymbol{f}_\mathrm{f} = \boldsymbol{b}_\mathrm{f} + \frac{\rho_\mathrm{f}}{\Delta t} \boldsymbol{u}_\mathrm{f}^0, \tag{6.19}$$

$$\beta_\mathrm{s} = \frac{4\rho_\mathrm{s}}{\Delta t^2}, \qquad \boldsymbol{f}_\mathrm{s} = \boldsymbol{b}_\mathrm{s} + \rho_\mathrm{s} \left(\frac{4\boldsymbol{u}_\mathrm{s}^0 + \Delta t (4\boldsymbol{v}_\mathrm{s}^0 + \boldsymbol{a}_\mathrm{s}^0)}{\Delta t^2} \right), \tag{6.20}$$

$$\alpha_\mathrm{s} = \frac{1}{\Delta t}, \qquad \alpha_\mathrm{f} = 1, \qquad \boldsymbol{g}_\Sigma = \frac{1}{\Delta t} \boldsymbol{u}_\mathrm{s}^0. \tag{6.21}$$

We note that these are not the only choices of time discretizations that lead to equations of the form (6.18). As this work is mainly concerned with the space discretization, we make no further comment on time integration, but as a general estimation by dimensional analysis, given a time step size Δt, we can find time-stepping schemes such that we need to solve a system of the form (6.18) with

$$\beta_\mathrm{f} \sim \frac{1}{\Delta t}, \qquad \beta_\mathrm{s} \sim \frac{1}{\Delta t^2}, \qquad \frac{\alpha_\mathrm{f}}{\alpha_\mathrm{s}} \sim \Delta t.$$

The HDG method

For $\star \in \{\mathrm{f}, \mathrm{s}\}$, consider a simplicial mesh $\mathcal{T}_\star^h$ of $\Omega_\star$ with $\Gamma_\star^h := (\partial\Omega_\star \setminus \Sigma) \cap \partial\Omega_\star^h$ and $\Sigma_\star^h := \partial\Omega_\star^h \setminus \Gamma_h^h$. We define the *global* finite element spaces

$$\mathbb{V}_\star^h := \prod_{K \in \mathcal{T}_\star^h} \mathbb{V}_\star^h(K) \qquad \boldsymbol{W}_\star^h := \prod_{K \in \mathcal{T}_\star^h} \boldsymbol{W}_\star^h(K)$$

$$\mathbb{A}_\star^h := \prod_{K \in \mathcal{T}_\star^h} \mathbb{A}_\star^h(K) \qquad \boldsymbol{M}_\star^h := \prod_{e \in \mathcal{E}_\star^h} \boldsymbol{M}_\star^h(e)$$

via the *local* finite element spaces

$$\begin{aligned}
\mathbb{V}^h(K) &:= [\mathcal{P}_k(K)]^{d\times d} \oplus \left(\nabla \times \left(\left(\nabla \times \tilde{\mathbb{A}}(K)\right) b_K\right)\right)\\
\boldsymbol{W}^h(K) &:= [\mathcal{P}_k(K)]^d\\
\mathbb{A}^h(K) &:= \begin{pmatrix} 0 & 1\\ -1 & 0\end{pmatrix} \mathcal{P}_k(K)\\
\boldsymbol{M}^h(e) &:= \mathcal{P}_k(e),
\end{aligned}$$

where $\tilde{\mathbb{A}}(K) := \{\mathbb{G} \in \mathbb{A}(K) : \mathbb{G}_{ij} \in \widetilde{\mathcal{P}}_k(K), i \neq j\}$ and b_K is the bubble function corresponding to the element K; see [Cockburn et al., 2013].

We can now state our HDG formulation as: find $(\mathbb{S}^h_\star, \boldsymbol{u}^h_\star, \mathbb{G}^h_\star, \hat{\boldsymbol{u}}^h_\star) \in \mathbb{V}^h_\star \times \boldsymbol{W}^h_\star \times \mathbb{A}^h_\star \times \boldsymbol{M}^h_\star$ such that

$$\left(\mathcal{A}_\star(\mathbb{S}^h_\star), \overline{\mathbb{S}}_\star\right)_{\mathcal{T}^h_\star} + \left(\boldsymbol{u}^h_\star, \nabla\cdot\overline{\mathbb{S}}_\star\right)_{\mathcal{T}^h_\star} + \left(\mathbb{G}^h_\star, \overline{\mathbb{S}}_\star\right)_{\mathcal{T}^h_\star} - \left\langle \hat{\boldsymbol{u}}^h_\star, \mathbb{S}_\star\boldsymbol{\nu}^h_\star\right\rangle_{\partial\mathcal{T}^h_\star} = 0 \quad (6.22a)$$

$$(\nabla\cdot\mathbb{S}_\star, \overline{\boldsymbol{u}}_\star)_{\mathcal{T}^h_\star} - \left\langle \tau^h_\star\left(\boldsymbol{u}^h_\star - \hat{\boldsymbol{u}}^h_\star\right), \overline{\boldsymbol{u}}_\star\right\rangle_{\partial\mathcal{T}^h_\star} - \left(\beta_\star\boldsymbol{u}^h_\star, \overline{\boldsymbol{u}}_\star\right)_{\mathcal{T}^h_\star} + (\boldsymbol{f}_\star, \overline{\boldsymbol{u}}_\star)_{\mathcal{T}^h_\star} = 0, \quad (6.22b)$$

$$\left(\mathbb{S}^h_\star, \overline{\mathbb{G}}^h_\star\right)_{\mathcal{T}^h_\star} = 0, \quad (6.22c)$$

$$\left\langle \mathbb{S}^h_\star\boldsymbol{\nu}_\star - \tau^h_\star\left(\boldsymbol{u}^h_\star - \hat{\boldsymbol{u}}^h_\star\right), \mu_\star\right\rangle_{\partial\mathcal{T}^h_\star\setminus(\Gamma^h_\star\cup\Sigma^h_\star)} = 0 \quad (6.22d)$$

$$\left\langle \hat{\boldsymbol{u}}^h_\star, \mu_\star\right\rangle_{\Gamma^h_\star} = 0 \quad (6.22e)$$

for all $(\overline{\mathbb{S}}_\star, \overline{\boldsymbol{u}}_\star, \overline{\mathbb{G}}_\star, \mu_\star) \in \mathbb{V}^h_\star \times \boldsymbol{W}^h_\star \times \mathbb{A}^h_\star \times \boldsymbol{M}^h_\star$, together with transmission conditions

$$\left\langle (\alpha_{\mathrm{s}}\tilde{\boldsymbol{u}}^h_{\mathrm{s}} + \alpha_{\mathrm{f}}\tilde{\boldsymbol{u}}^h_{\mathrm{f}})\circ\psi_{\mathrm{s}}, \mu_{\mathrm{s}}\right\rangle_{\Sigma^h_{\mathrm{s}}} = \langle \boldsymbol{g}_\Sigma\circ\psi_{\mathrm{s}}, \mu_{\mathrm{s}}\rangle_{\Sigma^h_{\mathrm{s}}} \qquad \forall\mu_{\mathrm{s}} \in \boldsymbol{M}^h_{\mathrm{s}}, \quad (6.22f)$$

$$\left\langle (\tilde{\mathbb{S}}^h_{\mathrm{s}}\boldsymbol{\nu}_{\mathrm{s}} + \tilde{\mathbb{S}}^h_{\mathrm{f}}\boldsymbol{\nu}_{\mathrm{f}})\circ\psi_{\mathrm{f}}, \mu_{\mathrm{f}}\right\rangle_{\Sigma^h_{\mathrm{f}}} = 0 \qquad \forall\mu_{\mathrm{f}} \in \boldsymbol{M}^h_{\mathrm{f}}, \quad (6.22g)$$

and the zero-mean-pressure uniqueness condition

$$\left(\mathrm{tr}(\mathbb{S}^h_{\mathrm{f}}), 1\right)_{\mathcal{T}^h_{\mathrm{f}}} = 0. \quad (6.22h)$$

The transferred fields are defined as follows:

$$\begin{aligned}
\tilde{\boldsymbol{u}}^h_\star &:= \hat{\boldsymbol{u}}^h_\star + \int_{\boldsymbol{x}_h}^{\boldsymbol{x}} (\mathcal{A}(\mathbb{S}^h_\star) + \mathbb{G}^h_\star)\boldsymbol{m}, \qquad \star \in \{\mathrm{f}, \mathrm{s}\},\\
\tilde{\mathbb{S}}^h_{\mathrm{s}}\boldsymbol{\nu}_{\mathrm{s}} &:= E(\mathbb{S}^h_{\mathrm{s}})\boldsymbol{\nu}_{\mathrm{s}} - \tau^h_{\mathrm{s}}(\boldsymbol{u}^h_{\mathrm{s}} - \hat{\boldsymbol{u}}^h_{\mathrm{s}})\circ\psi_{\mathrm{s}}\\
\tilde{\mathbb{S}}^h_{\mathrm{f}}\boldsymbol{\nu}_{\mathrm{f}} &:= E(\mathbb{S}^h_{\mathrm{f}} - p^h_0\mathbb{I})\boldsymbol{\nu}_{\mathrm{f}} - \tau^h_{\mathrm{f}}(\boldsymbol{u}^h_{\mathrm{f}} - \hat{\boldsymbol{u}}^h_{\mathrm{f}})\circ\psi_{\mathrm{f}}
\end{aligned}$$

where $\boldsymbol{m}$ is the tangent unit vector to the corresponding transfer paths, E is the extrapolation operator, $\psi_\star$ is the mapping between the exact interface and its discrete counterpart and the term

$$p_0^h := \frac{-1}{2|\Omega_{\mathrm{f}}^h|}(E(\mathrm{tr}(\mathbb{S}_{\mathrm{f}}^h), 1))_{\Omega_{\mathrm{f}}\setminus\Omega_{\mathrm{f}}^h}$$

accounts for the pressure mean difference between Ω_{f} and $\Omega_{\mathrm{f,h}}$.

A difference in this work compared to Papers IV and V is that the transfer of the dual variables is not of the normal trace with respect to the normal vector to the discrete interface, but the normal vector to the exact one. This is in line with what had been done in the work of Qiu et al. [2016] for elliptic interface problems with TPM. This allows the treatment of curved interfaces at the cost of requiring more information on the exact geometry.

Numerical results

We solve steady-state problems on $\Omega = [0,1]^2$ partitioned into Ω_{f} and Ω_{s} according to two different curved interfaces. The rest of the parameters for both experiments are $\Delta t = \rho_{\mathrm{f}} = \rho_{\mathrm{s}} = 1.0 = \mu_{\mathrm{f}} = 1$, $\lambda_{\mathrm{s}} = \frac{3}{4}$ and $\mu_{\mathrm{s}} = \frac{3}{8}$. The manufactured solution is

$$\begin{aligned}
\boldsymbol{u}_{\mathrm{f}}(\boldsymbol{x}) &= \begin{pmatrix} -\pi\sin(\pi x)\cos(\pi y) \\ -\pi\cos(\pi x)\sin(\pi y) \end{pmatrix}, \\
\frac{1}{3}\mathrm{tr}(\mathbb{S}_{\mathrm{f}}(\boldsymbol{x})) &= \exp(-((\boldsymbol{x}_1 - 0.5)^2 + (\boldsymbol{x} - 0.5)^2)), \\
\boldsymbol{u}_{\mathrm{s}}(\boldsymbol{x}) &= \begin{pmatrix} \cos(\pi x) \\ \sin(\pi y). \end{pmatrix}
\end{aligned}$$

In the first case, we consider the parametrized interface

$$\Sigma := \{(t, 0.5 + 0.05\sin(2\pi t)) : 0 \leq t \leq 1\}$$

and take Ω_{f} as the domain above the interface. We show the results in Figure 6.8 and Figure 6.9 for meshes obtained by shifting a linear interpolation of the interface, obtaining optimal convergence in all variables for both gaps of order $\mathcal{O}(h^2)$ and $\mathcal{O}(h)$. However, the superconvergence in the trace variable is lost in the latter.

In the second case, we consider the closed circular interface given by

$$\Sigma = \{\boldsymbol{x} : |\boldsymbol{x} - (0.5, 0.5)^{\mathrm{t}}| = 0.4\}$$

and take Ω_{f} as the domain outside the circle. We show the results in Figure 6.10 and Table 6.1 for meshes obtained by utilizing a structured background mesh. Since the deviation between the exterior normal vector of the meshes and the exact interface do not vanish

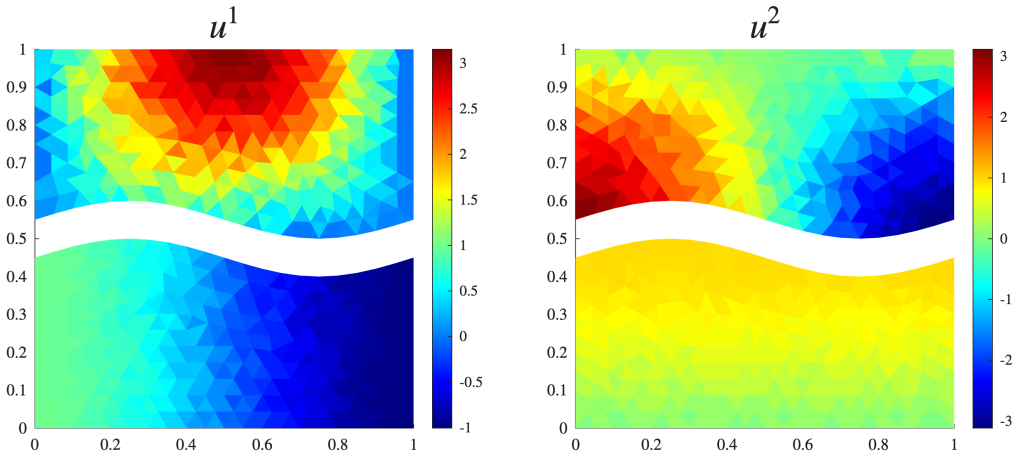

Figure 6.8: Fluid velocity (top) and displacement (bottom) using $\mathcal{P}_1$ elements on meshes with 416 elements each and a gap of $\delta = 0.05$ with respect to Σ.

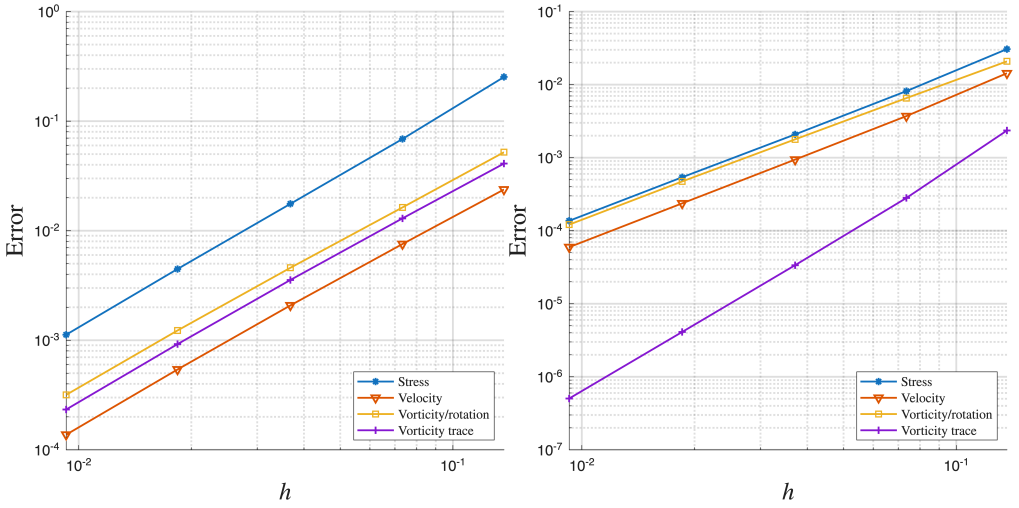

Figure 6.9: Convergence with gaps of order h (left) and h^2 (right) for the curved interface case with $\mathcal{P}_1$ elements. We see that, while both cases are convergent, the gap of order h loses the superconvergence of the trace error.

when refining the discretization (as we have used a background mesh instead of linear interpolation), the method does not converge.

Finally, we take the 2D hemodynamics linear FSI problem found in [Meddahi, 2025] and solve it using the TPM. The results can be found in Figure 6.11. The exact domains are

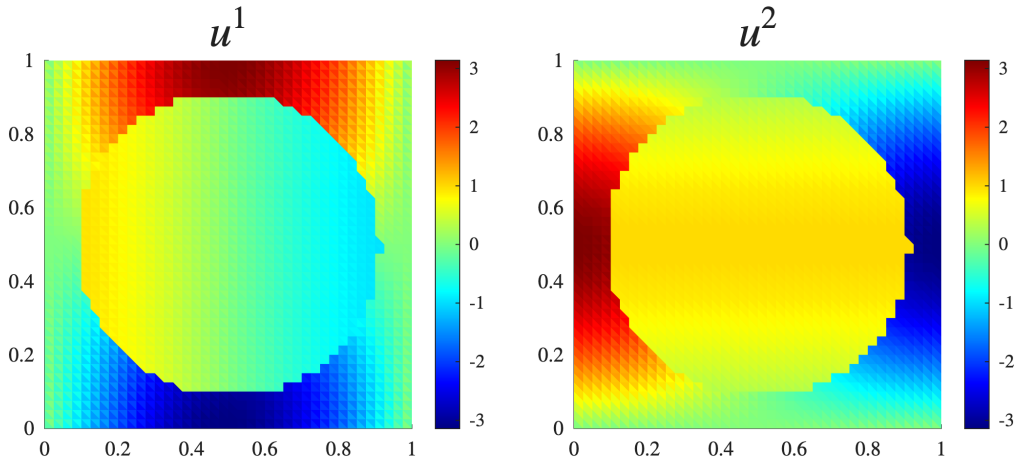

Figure 6.10: Fluid velocity (outside) and displacement (inside) using $\mathcal{P}_3$ elements using a background mesh with 2200 elements.

Table 6.1: Convergence history for the circular interface with structured background meshes with $N = 200, 800, 3200, 12800$ elements.

k	#d.o.f.	σ	e.o.c.	$\boldsymbol{u}$	e.o.c.	γ	e.o.c.	$\hat{\boldsymbol{u}}$	e.o.c.
1	1315	4e-01	*	1e-02	*	3e-01	*	3e-02	*
	5227	1e-01	1.7	4e-03	2.0	5e-02	2.3	6e-03	2.5
	20829	5e-02	1.1	1e-03	1.4	1e-02	1.7	2e-03	1.0
	83215	6e-03	3.1	2e-04	2.6	2e-03	2.6	1e-04	3.8
2	1931	3e-02	*	1e-03	*	1e-02	*	2e-03	*
	7661	1e-02	0.8	3e-04	1.7	6e-03	1.3	9e-04	1.6
	30491	3e-03	2.4	4e-05	3.1	1e-03	2.7	9e-05	3.3
	121737	5e-03	-0.8	1e-04	-1.5	2e-03	-1.0	2e-04	-1.4
3	2547	9e-02	*	1e-03	*	2e-02	*	6e-03	*
	10095	2e-03	5.6	5e-05	4.8	3e-04	6.1	1e-04	5.7
	40153	3e-03	-0.8	5e-05	-0.1	1e-03	-1.8	1e-04	-0.2
	160259	1e-01	-5.0	9e-04	-4.0	4e-02	-4.9	2e-03	-3.9

$\Omega_f = [0, 6] \times [0, 0.5]$ and $\Omega_s = [0, 6] \times [0.5, 0.5]$. The discrete domains are $\Omega_f^h = [0, 6] \times [0, 0.45]$ and $\Omega_s^h = [0, 6] \times [0.55, 0.6]$.

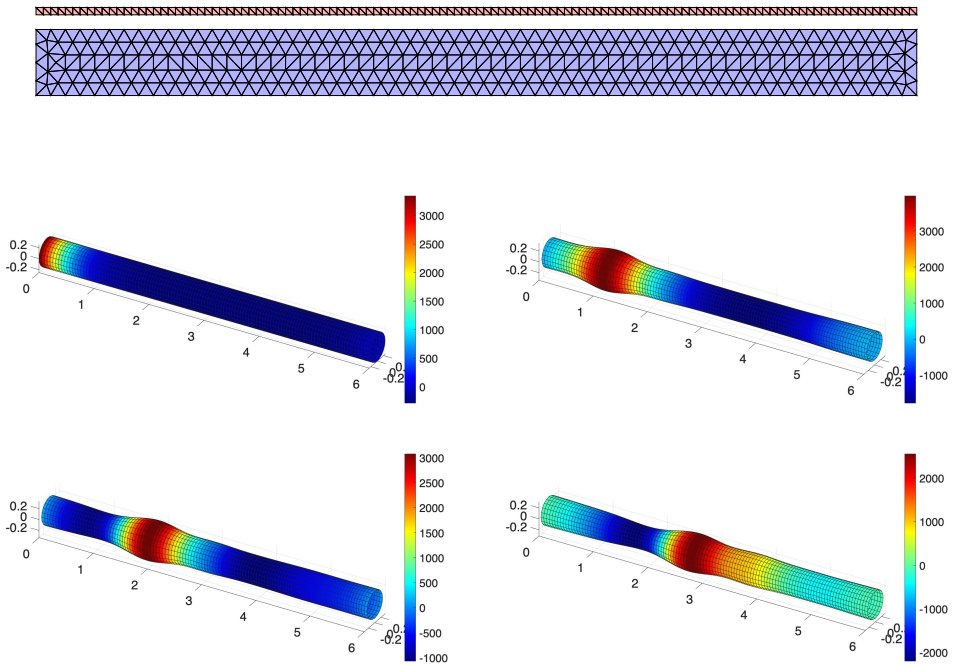

Figure 6.11: Top: 2D meshes utilized for the hemodynamics simulation. The meshes are separated by a gap of length $\delta = 0.05$. **Bottom:** 3D representation of the 2D hemodynamics problem solved at (from left to right and top to bottom) $t = 1 \times 10^{-4}$, $t = 1 \times 10^{-3}$, $t = \times 1.5 \times 10^{-3}$ and $t = 2 \times 10^{-3}$. The coloring represents the fluid pressure at the midpoint of the blood vessel and the mesh is deformed (exaggerated) according to the vertical displacement at the interface.
The cylindrical plot is obtained by measuring a point $x \in [0, 6]$ and assigning the radius according to the value of the vertical displacement of the solid at that point.

Conclusions

Summary of results

In this section, we give a small summary of the contributions of each paper of the thesis, indexed by their corresponding roman numeral.

IV. The TPM is utilized for the domain decomposition of the Stokes flow equation, with an extra treatment of the pressure. This answers partially Research question (iv). For Research question (vi), convergence is proven for gaps of order h^2, but numerical experiments show optimal convergence with gaps of order h for flat interfaces. This suggests that theoretical bounds can be improved.

V. The TPM is extended to a Stokes/Darcy coupling in which the physical interface has source terms, providing an answer to Research questions (iv) and (v). Convergence is proven for gaps of order $h^{1+\gamma}$ with $\gamma > 3/4$ and semi-aligned interfaces, which is an improvement from the h^2 case.

Outlook

1. **Moving domains**
   A natural extension of the linear fluid-structure interaction problem is to consider a moving interface. This leads to the question on how to estimate the future position of a domain in order to set the transfer paths.

2. **Non-monolithic coupling**
   Thus far, only monolithic coupling has been studied using transfer paths. It is, however, possible to weakly couple interface conditions in an iterative way, as it is done in the wave relaxation method. Since the TPM presents a systematic way of defining extensions from subdomains, it should be possible to apply it to this context.

3. **Completely unfitted meshes**
   When considering sequences of meshes where the unit exterior normal vectors $\boldsymbol{\nu}_\star^h$ do not align in the limit with the unit exterior normal of the physical interface $\boldsymbol{\nu}_\Sigma$, the method as it is now does not convergence. We believe that one can modify the geometry locally in order to account for this, obtaining a convergent method.

Bibliography

[1] D. Acosta-Soba, F. Guillén-González, and J. R. Rodríguez-Galván. An upwind DG scheme preserving the maximum principle for the convective Cahn-Hilliard model. *Numerical Algorithms*, 92(3):1589–1619, Mar. 2023.

[2] N. M. Atallah, C. Canuto, and G. Scovazzi. The high-order shifted boundary method and its analysis. *Comput. Methods Appl. Mech. Eng.*, 394:114885, May 2022.

[3] M. N. Baker. *The Quest for Pure Water; the History of Water Purification from the Earliest Records to the Twentieth Century*. New York, 1949.

[4] J. W. Barrett, J. F. Blowey, and H. Garcke. Finite element approximation of the Cahn–Hilliard equation with degenerate mobility. *SIAM J. Numer. Anal.*, 37(1):286–318, Jan. 1999.

[5] G. Beer. An isoparametric joint/interface element for finite element analysis. *Int. J. Numer. Methods Eng.*, 21(4):585–600, Apr. 1985.

[6] G. Beer and S. Bordas, editors. *Isogeometric Methods for Numerical Simulation*, volume 561 of *CISM International Centre for Mechanical Sciences*. Vienna, 2015.

[7] F. B. Belgacem. The mortar finite element method with lagrange multipliers. *Numer. Math.*, 84(2):173–197, Dec. 1999.

[8] V. Benci, S. Nardulli, and P. Piccione. Multiple solutions for the van der waals–allen–Cahn– Hilliard equation with a volume constraint. *Calc. Var. Partial Differ. Equations*, 59(2):64–93, Apr. 2020.

[9] C. Bernardi. A new nonconforming approach to domain decomposition: The mortar element method. *Nonliner Partial Differ. Equ. Their Appl.*, 1994.

[10] F. Bertrand and D. Boffi. On the necessity of the inf-sup condition for a mixed finite element formulation. *IMA J. Numer. Anal.*, 45(1):1–35, Feb. 2025.

[11] D. Boffi, F. Brezzi, and M. Fortin. *Mixed Finite Element Methods and Applications*, volume 44 of *Springer Series in Computational Mathematics*. Berlin, Heidelberg, 2013.

[12] J. H. Bramble, T. Dupont, and V. Thomee. Projection methods for dirichlet's problem in approximating polygonal domains with boundary-value corrections. *Math. Comput.*, 26(120):869–880, Oct. 1972.

[13] S. C. Brenner and L. R. Scott. *The Mathematical Theory of Finite Element Methods*, volume 15 of *Texts in Applied Mathematics*. New York, NY, 2008.

[14] R. Bürger, W. Wendland, and F. Concha. Model equations for gravitational sedimentation-consolidation processes. *ZAMM Z. Angew. Math. Mech.*, 80(2):79–92, Feb. 2000.

[15] R. Bürger, S. Diehl, and I. Nopens. A consistent modelling methodology for secondary settling tanks in wastewater treatment. *Water Res.*, 45(6):2247–2260, Mar. 2011.

[16] R. Bürger, J. Careaga, and S. Diehl. A simulation model for settling tanks with varying cross-sectional area. *Chem. Eng. Commun.*, 204(11):1270–1281, Nov. 2017.

[17] E. Burman, P. Hansbo, and M. G. Larson. A cut finite element method with boundary value correction. *Math. Comput.*, 87(310):633–657, Oct. 2017.

[18] E. Burman, P. Hansbo, M. G. Larson, and S. Zahedi. Cut finite element methods. *Acta Numer.*, 34:1–121, July 2025.

[19] J. W. Cahn. Free energy of a nonuniform system. II. Thermodynamic basis. *J. Chem. Phys.*, 30(5):1121–1124, May 1959.

[20] J. W. Cahn and J. E. Hilliard. Free energy of a nonuniform system. I. Interfacial free energy. *J. Chem. Phys.*, 28(2):258–267, Feb. 1958.

[21] J. W. Cahn and J. E. Hilliard. Free energy of a nonuniform system. III. Nucleation in a two-component incompressible fluid. *J. Chem. Phys.*, 31(3):688–699, Sept. 1959.

[22] L. C. Campos, S. R. Smith, and N. J. D. Graham. Deterministic-based model of slow sand filtration. I: Model development. *J. Environ. Eng.*, 132(8):872–886, Aug. 2006.

[23] J. M. Cárdenas and M. Solano. A high order unfitted hybridizable discontinuous galerkin method for linear elasticity. *IMA J. Numer. Anal.*, 44(2):945–979, Apr. 2024.

[24] P. Castillo, B. Cockburn, I. Perugia, and D. Schötzau. An a priori error analysis of the local discontinuous galerkin method for elliptic problems. *SIAM J. Numer. Anal.*, 38(5):1676–1706, Jan. 2000.

[25] A. Cesmelioglu, J. J. Lee, and S. Rhebergen. Hybridizable discontinuous galerkin methods for the coupled Stokes–Biot problem. *Comput. Math. Appl.*, 144:12–33, Aug. 2023.

[26] C. Chatelain, T. Balois, P. Ciarletta, and M. Ben Amar. Emergence of microstructural patterns in skin cancer: A phase separation analysis in a binary mixture. *New J. Phys.*, 13(11):115013, Nov. 2011.

[27] J. Cheung, M. Gunzburger, P. Bochev, and M. Perego. An optimally convergent higher-order finite element coupling method for interface and domain decomposition problems. *Results Appl. Math.*, 6:100094, May 2020.

[28] P. G. Ciarlet. Orders of convergence in finite element methods. In *The Mathematics of Finite Elements and Applications*, pages 113–129. 1973.

[29] P. G. Ciarlet. *The Finite Element Method for Elliptic Problems*. Number 40 in Classics in Applied Mathematics. Philadelphia, Pa, 2002.

[30] P. G. Ciarlet and P.-A. Raviart. The combined effect of curved boundaries and numerical integration in isoparametric finite element methods. In *The Mathematical Foundations of the Finite Element Method with Applications to Partial Differential Equations*, pages 409–474. 1972.

[31] B. Cockburn. Hybridizable discontinuous galerkin methods for second-order elliptic problems: Overview, a new result and open problems. *Jpn. J. Ind. Appl. Math.*, 40 (3):1637–1676, Sept. 2023.

[32] B. Cockburn and J. Gopalakrishnan. A characterization of hybridized mixed methods for second order elliptic problems. *SIAM J. Numer. Anal.*, 42(1):283–301, 2005.

[33] B. Cockburn and C.-W. Shu. The local discontinuous galerkin method for time-dependent convection-diffusion systems. *SIAM J. Numer. Anal.*, 35(6):2440–2463, Dec. 1998.

[34] B. Cockburn and M. Solano. Solving dirichlet boundary-value problems on curved domains by extensions from subdomains. *SIAM J. Sci. Comput.*, 34(1):A497–A519, Jan. 2012.

[35] B. Cockburn, B. Dong, and J. Guzmán. A superconvergent LDG-hybridizable galerkin method for second-order elliptic problems. *Math. Comput.*, 77(264):1887–1916, May 2008.

[36] B. Cockburn, J. Gopalakrishnan, and R. Lazarov. Unified hybridization of discontinuous galerkin, mixed, and continuous galerkin methods for second order elliptic problems. *SIAM J. Numer. Anal.*, 47(2):1319–1365, Jan. 2009.

[37] B. Cockburn, F.-J. Sayas, and M. Solano. Coupling at a distance HDG and BEM. *SIAM J. Sci. Comput.*, 34(1):A28–A47, Jan. 2012.

[38] B. Cockburn, W. Qiu, and M. Solano. A priori error analysis for HDG methods using extensions from subdomains to achieve boundary conformity. *Math. Comput.*, 83(286):665–699, July 2013.

[39] B. Cockburn, O. Dubois, J. Gopalakrishnan, and S. Tan. Multigrid for an HDG method. *IMA J. Numer. Anal.*, 34(4):1386–1425, Oct. 2014.

[40] N. G. Cogan. The role of the biofilm matrix in structural development. *Math. Med. Biol.*, 21(2):147–166, June 2004.

[41] D. S. Cohen and J. D. Murray. A generalized diffusion model for growth and dispersal in a population. *J. Math. Biol.*, 12(2):237–249, June 1981.

[42] F. H. De Souza, B. S. Pizzolatti, J. M. Schöntag, and M. L. Sens. Study of slow sand filtration with backwash and the influence of the filter media on the filter recovery and cleaning. *Environ. Technol.*, 37(14):1802–1810, July 2016.

[43] S. Diehl. On scalar conservation laws with point source and discontinuous flux function. *SIAM J. Math. Anal.*, 26(6):1425–1451, Nov. 1995.

[44] D. A. Drew and S. L. Passman. *Theory of Multicomponent Fluids*, volume 135 of *Applied Mathematical Sciences*. New York, NY, 1999.

[45] S. Du and F.-J. Sayas. *An Invitation to the Theory of the Hybridizable Discontinuous Galerkin Method: Projections, Estimates, Tools*. SpringerBriefs in Mathematics. Cham, 2019.

[46] T. Dupont. L2 error estimates for projection methods for parabolic equations in approximating domains. In *Mathematical Aspects of Finite Elements in Partial Differential Equations*, pages 313–352. 1974.

[47] M. Duprez and A. Lozinski. ϕ-FEM: A finite element method on domains defined by level-sets. *SIAM J. Numer. Anal.*, 58(2):1008–1028, Jan. 2020.

[48] M. Dziwnik. The role of degenerate mobilities in Cahn-Hilliard models. *Pamm*, 19 (1):e201900396, Nov. 2019.

[49] M. Ebenbeck and H. Garcke. Analysis of a Cahn–Hilliard–brinkman model for tumour growth with chemotaxis. *J. Differ. Equations*, 266(9):5998–6036, Apr. 2019.

[50] C. M. Elliott and H. Garcke. On the Cahn–Hilliard equation with degenerate mobility. *SIAM J. Math. Anal.*, 27(2):404–423, Mar. 1996.

[51] E. Engström and E. Hansen. Convergence analysis of the nonoverlapping robin–robin method for nonlinear elliptic equations. *SIAM J. Numer. Anal.*, 60(2):585–605, Apr. 2022.

[52] A. Ern and J.-L. Guermond. *Theory and Practice of Finite Elements*, volume 159 of *Applied Mathematical Sciences*. New York, NY, 2004.

[53] A. Ern and J.-L. Guermond. *Finite Elements I: Approximation and Interpolation*, volume 72 of *Texts in Applied Mathematics*. Cham, 2021.

[54] D. J. Eyre. *An Unconditionally Stable One-Step Scheme for Gradient Systems*. 1998.

[55] B. Flemisch, J. Melenk, and B. Wohlmuth. Mortar methods with curved interfaces. *Appl. Numer. Math.*, 54(3-4):339–361, Aug. 2005.

[56] P. J. Flory. *Principles of Polymer Chemistry*. 1953.

[57] B. Fraeijs de Veubeke. Displacement and equilibrium models in the finite element method. *Modèles déplacement et équilibre dans la méthode des éléments finis*, 1965.

[58] L. P. Franca and T. J. Hughes. Two classes of mixed finite element methods. *Comput. Methods Appl. Mech. Eng.*, 69(1):89–129, July 1988.

[59] Z. Fu, L. F. Gatica, and F.-j. Sayas. Algorithm 949: MATLAB tools for HDG in three dimensions. *ACM Trans. Math. Software*, 41(3):1–21, June 2015.

[60] C. A. Fux, S. Wilson, and P. Stoodley. Detachment characteristics and oxacillin resistance of *Staphyloccocus aureus* biofilm emboli in an In vitro catheter infection model. *J. Bacteriol.*, 186(14):4486–4491, July 2004.

[61] H. Garcke, P. Knopf, J. Wittmann, and Faculty For Mathematics, University Of Regensburg, Universitätsstr. 31, 93053 Regensburg, Germany. The anisotropic Cahn–Hilliard equation: Regularity theory and strict separation properties. *Discrete Contin. Dyn. Syst. - S*, 16(12):3622–3660, 2023.

[62] G. N. Gatica. *A Simple Introduction to the Mixed Finite Element Method: Theory and Applications*. SpringerBriefs in Mathematics. Cham, 2014.

[63] R. Glowinski, T.-W. Pan, and J. Periaux. A fictitious domain method for dirichlet problem and applications. *Comput. Methods Appl. Mech. Eng.*, 111(3-4):283–303, Jan. 1994.

[64] R. Glowinski, T.-W. Pan, and J. Periaux. A lagrange multiplier/fictitious domain method for the dirichlet problem — generalization to some flow problems. *Jpn. J. Ind. Appl. Math.*, 12(1):87–108, Feb. 1995.

[65] O. Gonzalez and A. M. Stuart. *A First Course in Continuum Mechanics*. Cambridge Texts in Applied Mathematics. Cambridge, 2008.

[66] P. Gosselet and C. Rey. Non-overlapping domain decomposition methods in structural mechanics. *Arch. Comput. Methods Eng.*, 13(4):515–572, Dec. 2006.

[67] M. Grasselli, L. Melzi, and A. Signori. On a non-local phase-field model for tumour growth with single-well lennard-jones potential. *Nonlinear Anal. Real World Appl.*, 88:104466, Apr. 2026.

[68] E. Guchi. Review on slow sand filtration in removing microbial contamination and particles from drinking water. *Am. J. Food Nutr.*, 3(2):47–55, Aug. 2017.

[69] F. Guillén-González and G. Tierra. Structure preserving finite element schemes for the Navier-Stokes-Cahn-Hilliard system with degenerate mobility. *Comput. Math. Appl.*, 172:181–201, Oct. 2024.

[70] J. K. Gunnarsson and R. Klöfkorn. Comparison of structure preserving schemes for the Cahn-Hilliard-Navier-Stokes equations with degenerate mobility and adaptive mesh refinement, 2026.

[71] R. J. Guyan. Reduction of stiffness and mass matrices. *AIAA J.*, 3(2):380–380, Feb. 1965.

[72] P. Hansbo. Nitsche's method for interface problems in computational mechanics. *GAMM-Mitt.*, 28(2):183–206, Nov. 2005.

[73] C. Helmer and A. Jüngel. Existence analysis for a reaction-diffusion Cahn– Hilliard-type system with degenerate mobility and singular potential modeling biofilm growth. *Discrete Contin. Dyn. Syst.*, 43(10):3839–3861, 2023.

[74] E. Henríquez and M. Solano. An unfitted HDG method for a distributed optimal control problem. *J. Comput. Appl. Math.*, 441:115703, May 2024.

[75] E. Henríquez and M. Solano. An unfitted HDG method for a distributed optimal convection-diffusion control problem, Mar. 2026.

[76] T. Hughes, J. Cottrell, and Y. Bazilevs. Isogeometric analysis: CAD, finite elements, NURBS, exact geometry and mesh refinement. *Comput. Methods Appl. Mech. Eng.*, 194(39-41):4135–4195, Oct. 2005.

[77] L. Huisman and W. E. Wood. *Slow Sand Filtration*. 1974.

[78] T. Iwasaki. Some notes on sand filtration. *J. AWWA*, 29(10):1591–1597, Oct. 1937.

[79] H. S. Jabur, J. Mårtensson, and G. Öllös. Some notes on hydraulics and a mathematical description of slow sand filtration. *Vatten*, 61(3), 1994.

[80] C. Jackisch and E. Kröner. Darcy's law. In *Encyclopedia of Soils in the Environment*, pages 240–246. 2023.

[81] J. Kim, S. Lee, Y. Choi, S.-M. Lee, and D. Jeong. Basic principles and practical applications of the Cahn– Hilliard equation. *Math. Probl. Eng.*, 2016(1):1–11, 2016.

[82] K. L. A. Kirk, T. L. Horvath, A. Cesmelioglu, and S. Rhebergen. Analysis of a space-time hybridizable discontinuous galerkin method for the advection-diffusion problem on time-dependent domains. *SIAM J. Numer. Anal.*, 57(4):1677–1696, Jan. 2019.

[83] I. Klapper and J. Dockery. Role of cohesion in the material description of biofilms. *Phys. Rev. E*, 74(3):031902, Sept. 2006.

[84] I. Klapper and J. Dockery. Mathematical description of microbial biofilms. *SIAM Rev.*, 52(2):221–265, Jan. 2010.

[85] G. J. Kynch. A theory of sedimentation. *Trans. Faraday Soc.*, 48:166–176, 1952.

[86] K. Langenbach, P. Kuschk, H. Horn, and M. Kästner. Modeling of slow sand filtration for disinfection of secondary clarifier effluent. *Water Res.*, 44(1):159–166, Jan. 2010.

[87] C. Lehrenfeld and J. Schöberl. High order exactly divergence-free hybrid discontinuous galerkin methods for unsteady incompressible flows. *Comput. Methods Appl. Mech. Eng.*, 307:339–361, Aug. 2016.

[88] R. J. LeVeque. *Finite Volume Methods for Hyperbolic Problems*. Aug. 2002.

[89] R. J. LeVeque. *Finite Difference Methods for Ordinary and Partial Differential Equations: Steady-State and Time-Dependent Problems*. Philadelphia, PA, 2007.

[90] A. Main and G. Scovazzi. The shifted boundary method for embedded domain computations. Part I: Poisson and Stokes problems. *J. Comput. Phys.*, 372:972–995, Nov. 2018.

[91] J. K. Maiyo, S. Dasika, and C. T. Jafvert. Slow sand filters for the 21st century: A review. *Int. J. Environ. Res. Public Health*, 20(2):1019, Jan. 2023.

[92] R. S. Mansell and H. M. Selim. Mathematical models for predicting reactions of phosphorus applied to soils. *Model. Wastewater Renov.: Land Treat.*, pages 600–646, 1981.

[93] S. Meddahi. An hp error analysis of HDG for linear fluid–structure interaction. *J. Sci. Comput.*, 102(2):44–77, Feb. 2025.

[94] L. Melo. Biofilm physical structure, internal diffusivity and tortuosity. *Water Sci. Technol.*, 52(7):77–84, Oct. 2005.

[95] A. Miranville. *The Cahn–Hilliard Equation: Recent Advances and Applications*. Philadelphia, PA, Jan. 2019.

[96] N. M. Newmark. A method of computation for structural dynamics. *J. Eng. Mech. Div.*, 85(3):67–94, July 1959.

[97] J. Nitsche. Lineare spline-funktionen und die methoden von ritz für elliptische randwertprobleme. *Arch. Ration. Mech. Anal.*, 36(5):348–355, Jan. 1970.

[98] C. S. P. Ojha and N. J. D. Graham. Computer-aided simulation of slow sand filter performance. *Water Research*, 28(5):1025–1030, May 1994.

[99] R. Oyarzúa, M. Solano, and P. Zúñiga. A high order mixed-FEM for diffusion problems on curved domains. *J. Sci. Comput.*, 79(1):49–78, Apr. 2019.

[100] R. Oyarzúa, M. Solano, and P. Zúñiga. A priori and a posteriori error analyses of a high order unfitted mixed-FEM for Stokes flow. *Comput. Methods Appl. Mech. Eng.*, 360:112780, Mar. 2020.

[101] W. Qiu, M. Solano, and P. Vega. A high order HDG method for curved-interface problems via approximations from straight triangulations. *J. Sci. Comput.*, 69(3): 1384–1407, Dec. 2016.

[102] K. Quan, J. Hou, Z. Zhang, Y. Ren, B. W. Peterson, H.-C. Flemming, C. Mayer, H. J. Busscher, and H. C. Van Der Mei. Water in bacterial biofilms: Pores and channels, storage and transport functions. *Crit. Rev. Microbiol.*, 48(3):283–302, May 2022.

[103] A. Quarteroni, L. Dede', A. Manzoni, and C. Vergara. *Mathematical Modelling of the Human Cardiovascular System: Data , Numerical Approximation, Clinical Applications*. Cambridge Monographs on Applied and Computational Mathematics. Cambridge, 2019.

[104] F. Regazzoni. An optimally convergent fictitious domain method for interface problems. *Comput. Methods Appl. Mech. Eng.*, 431:117327, Nov. 2024.

[105] P. Reichert. AQUASIM 2.0 - user manual, computer program for the identification and simulation of aquatic systems. pages 1–219, Sept. 1998.

[106] S. Rhebergen and G. N. Wells. A hybridizable discontinuous galerkin method for the Navier –Stokes equations with pointwise divergence-free velocity field. *J. Sci. Comput.*, 76(3):1484–1501, Sept. 2018.

[107] T. Rosenqvist, J. Hilding, C. Suarez, and C. J. Paul. Microbial communities in slow sand filters for drinking water treatment adapt to organic matter altered by ozonation. *Water Res.*, 270:122843, Feb. 2025.

[108] Samuel Rideal. *Water and Its Purification: A Handbook for the Use of Local Authorities, Sanitary Officers, and Others Interested in Water Supply*. 1902.

[109] N. Sánchez, T. Sánchez-Vizuet, and M. Solano. Error analysis of an unfitted HDG method for a class of non-linear elliptic problems. *J. Sci. Comput.*, 90(3):92–119, Mar. 2022.

[110] N. Sánchez, T. Sánchez-Vizuet, and M. E. Solano. Afternote to "coupling at a distance": Convergence analysis and a priori error estimates. *Comput. Methods Appl. Math.*, 22(4):945–970, Oct. 2022.

[111] T. Sánchez-Vizuet, M. E. Solano, and A. J. Cerfon. Adaptive hybridizable discontinuous galerkin discretization of the grad–shafranov equation by extension from polygonal subdomains. *Comput. Phys. Commun.*, 255:107239, Oct. 2020.

[112] J. F. Schijven, H. H. Van Den Berg, M. Colin, Y. Dullemont, W. A. Hijnen, A. Magic-Knezev, W. A. Oorthuizen, and G. Wubbels. A mathematical model for removal of human pathogenic viruses and bacteria by slow sand filtration under variable operational conditions. *Water Res.*, 47(7):2592–2602, May 2013.

[113] H. M. Selim, R. Schulin, and H. Flühler. Transport and ion exchange of calcium and magnesium in an aggregated soil. *Soil Sci. Soc. Am. J.*, 51(4):876–884, July 1987.

[114] S. Shi, Y. Zhang, Q. Tang, and J. Mo. Modeling of biofilm growth and the related changes in hydraulic properties of porous media. *Membr. Water Treat.*, 12(5):217–225, Sept. 2021.

[115] J. Šimůnek, H. Saito, M. Sakai, and M. Van Genuchten. *The HYDRUS-1D Software Package for Simulating the One-Dimensional Movement of Water, Heat, and Multiple Solutes in Variably-Saturated Media*. Jan. 2008.

[116] M. Solano and F. Vargas. A high order HDG method for Stokes flow in curved domains. *J. Sci. Comput.*, 79(3):1505–1533, June 2019.

[117] M. Solano and F. Vargas M. An unfitted HDG method for oseen equations. *J. Comput. Appl. Math.*, 399:113721, Jan. 2022.

[118] M. Solano, S. Terrana, N.-C. Nguyen, and J. Peraire. An HDG method for dissimilar meshes. *IMA J. Numer. Anal.*, 42(2):1665–1699, Apr. 2022.

[119] G. Strang. Variational crimes in the finite element method. In *The Mathematical Foundations of the Finite Element Method with Applications to Partial Differential Equations*, pages 689–710. 1972.

[120] G. Strang and A. E. Berger. The change in solution due to change in domain. In D. Spencer, editor, *Proceedings of Symposia in Pure Mathematics*, volume 23, pages 199–205. Providence, Rhode Island, 1973.

[121] E. Torfs, S. Balemans, F. Locatelli, S. Diehl, R. Bürger, J. Laurent, P. François, and I. Nopens. On constitutive functions for hindered settling velocity in 1- D settler models: Selection of appropriate model structure. *Water Res.*, 110:38–47, Mar. 2017.

[122] M. T. Van Genuchten and R. J. Wagenet. Two-site/two-region models for pesticide transport and degradation: Theoretical development and analytical solutions. *Soil Sci. Soc. Am. J.*, 53(5):1303–1310, Sept. 1989.

[123] Q. Wang and T. Zhang. Review of mathematical models for biofilms. *Solid State Commun.*, 150(21-22):1009–1022, June 2010.

[124] Q. Wang and T. Zhang. Kinetic theories for biofilms. *Discrete Contin. Dyn. Syst. - B*, 17(3):1027–1059, 2012.

[125] Z. Wang and T. Hillen. Classical solutions and pattern formation for a volume filling chemotaxis model. *Chaos: Interdiscip. J. Nonlinear Sci.*, 17(3):037108, Sept. 2007.

[126] A. M. White and M. C. Kavanaugh. Discussion of "theory of sand filtration". *J. Sanit. Eng. Div.*, 96(2):620–622, Apr. 1970.

[127] C. Woodward and C. Ta. Developments in modelling slow sand filtration. *Slow Sand Filtr.: Recent Dev. Water Treat. Technol., John Wiley Sons N. Y. N. Y., 1988, P 349-366. 11 Fig 3 Tab 11 Ref.*, 1988.

[128] T. Zhang, N. G. Cogan, and Q. Wang. Phase field models for biofilms. I. Theory and one-dimensional simulations. *SIAM J. Appl. Math.*, 69(3):641–669, Jan. 2008.

Appendices

Appendix A

MPC-SSF: multi-phase continuum simulation of slow sand filters

A repository for this software can be found in:

`https://github.com/jaimemanriquezr/MPC-SSF`.

Contents

A.1 Introduction

We give a very brief description of the software used for the simulations presented in this thesis. We encourage the reader to read the GitHub page to read an up-to-date version of the code.

A.1.1 Scope

The aim of this program is to provide the user with a simple interface to simulate slow sand filtration using the multi-phase continuum mathematical-ecological model of slow sand filtration.

A.1.2 Installation

To install, you can download the code from MathWorks File Exchange or clone the repository from GitHub. You can then run the script `initpath.m` or activate the project file `.prj` to add all the necessary subdirectories.

A.1.3 A simple example

A typical code would be:

```
% Define geometry
ssf = SandFilter();
ssf.Temperature = 20; % [C]
ssf = ssf.addGridPoints(200);
% Define model
model = SSFModel(preset='Rosenqvist');
model.Detachment = @(v) 1.0 * sqrt(v / 10.0);
% Set initial state; clear sand by default
clean_ssf = State(ssf, model);
% Run simulation
options.TimeStep = 1E-06;
options.SimulationTime = 1.0;
results = simulate(clean_ssf, options);
```

A.2 Basic usage

A.2.1 Setting the geometry

To set the geometry, one has to create a `SandFilter` object and assign it a grid of approximation points.

```
% Define geometry
filter = SandFilter();
filter = filter.addGridPoints(200);
```

A `SandFilter` object has the following modifiable properties: `Height`, `Depth`, `SandPorosity`, `SandRoughness`, `InflowVelocity` and `Temperature`. For the light irradiation, we have

- `LightIrradiation` — $I = I(t)$,
- `LightAttenuatuationCoeffWater` — ν_{water},
- `LightAttenuationCoeffSand` — ν_{sand}.

A.2.2 Setting a model

You can either use a preset model

```
% Use the submodel introduced in Paper I
model = Model(preset='Rosenqvist')
```

or by define all your components and reactions individually.

```
% Define components
P = Particle(Name="Microorganism");
P.AttachmentMatrix = 10.0;
P.AttachmentSand = 1.0;
P.Density = 1.1;

P0 = P; % Use the same values as Microorganism
P0.Name = "POM";
P0.AttachmentSand = 0.0; % Or change them

L = Liquid(Name="Nutrient");
L.Density = 1.0;
```

```
% Define reactions
P_death = Reaction(Name="Inactivation", Order = dictionary(P, 1), ...
          StoichiometricCoefficients=dictionary(P, -1.0, P0, 1.0));
P_growth = Reaction(Name="Growth", Order = dictionary(P, 1), ...
           HalfSaturationConstants = dictionary(L, 1e-03), ...
           StoichiometricCoefficients=dictionary(P, 1.0, L, -1.0));
Hydrolysis = Reaction(Name="Hydrolysis", Order = dictionary(P, 1), ...
             HalfSaturationConstants=dictionary("Microorganism/POM", 2e-05), ...
             StoichiometricCoefficients=dictionary(P0, -1.0, L, 1.0));

% Create model
model = Model([P, P0, L], [P_death, P_growth, Hydrolysis]);

% Modify properties directly
model.WaterDensity = 1.0
```

It is also possible to use a preset and modify it.

```
model = Model(preset='Rosenqvist')
% Add a new component
PX = Particle(Name="PAT-X");
model.Components = [model.Components, PX];
```

By using the `plot` function, we can get a graph representing the ecological reactions of the model; see Figure A.1.

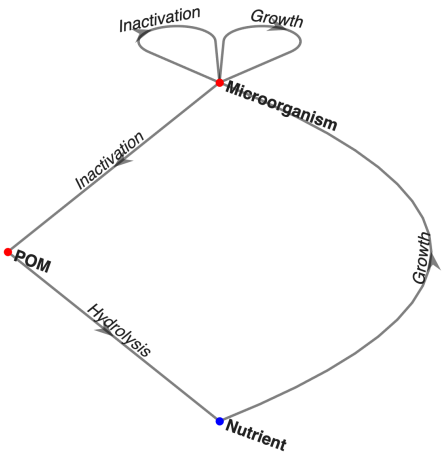

Figure A.1: Plot of a simplified model

Objects of the class `Model` have the following properties that can be modified: `Components`, `Reactions`, `WaterDensity`, `BiofilmPorosity`, `OsmosisRate`, `DetachmentFunction`

and `CohesionSubModel`. The latter sets parameters related to the biofilm cohesion part of the model. In our case, this corresponds to the Cahn–Hilliard-type model with parameters κ, ζ_0 and ζ_1.

A.2.3 Running a simulation

To run a simulation, you need a geometry (`SandFilter` object) and a set of equations (`Model` object). With these, you can define a `State` object and use the `simulate` method to start a simulation.

```
state = State(SandFilter(), Model());
```

It is possible to create a structure with specified settings and pass it using the `options` argument to pass it to the function.

```
options.TimeStep = "adaptive";
options.CloggingFraction = 0.8;
output = simulate(state, options);
```

Results can be then plotted using the `plot` function with an additional input specifying the desired type of plot, or using specific methods such as `plotBiofilm` and `plotConcentrations`; see Figure A.2.

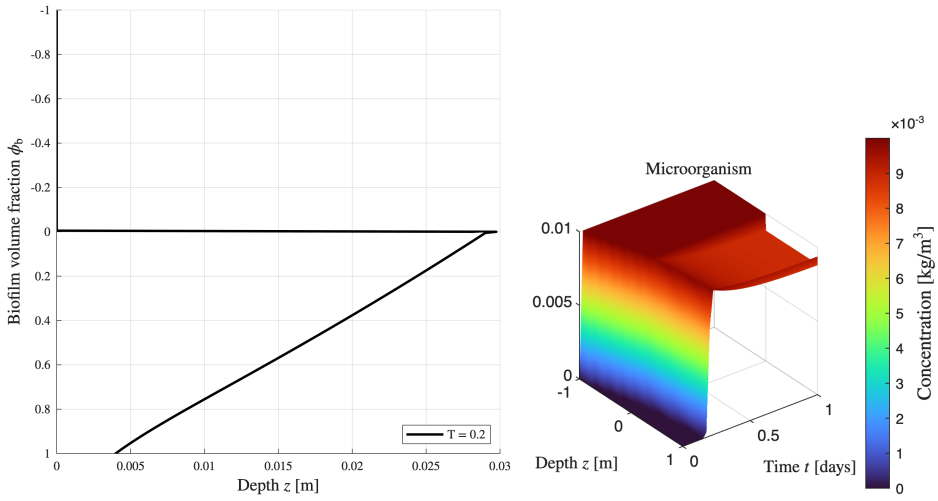

Figure A.2: Plots of ϕ_b (left) and global concentrations of Microorganism in the flowing suspension (right).

Appendix B

TPM-HDG: a MATLAB library for HDG using TPM

A repository for this software can be found in:

`https://github.com/jaimemanriquezr/TPM-HDG`.

In the `main` branch, scripts can be found for the Stokes/Darcy coupling and the FSI problem in the `examples` directory.

In the `ufl` branch, the HDG method was implemented with syntax similar to the Unified Form Language (UFL), and an example script is given below.

```
h = 1e-1; % mesh size
T_h = UnitSquareMesh(h);

k = 4; % polynomial degree
Pk = DubinerBasis(k);
VPk = Pk.to_vector();
Mk = LegendreBasis(k);
space = [VPk, Pk, Mk];

[q, u, u_hat] = get_trial_functions(space);
[r, v, v_hat] = get_test_functions(space);

dx = VolumeMeasure(T_h);
dS = FacetMeasure(T_h);
problem.equations = (q'*r)*dx + u*div(r)*dx + u_hat*(r'*n)*dS;
problem.flux = (-q + tau*(u - u_hat))*v_hat*dS;
[q, u, u_hat] = solve(problem);
```

Scientific publications

Author contributions

Co-authors are abbreviated as follows:
Isaac Bermúdez (IB), Julio Careaga (JC), Sandy Chan (SC), Stefan Diehl (SD),
Ngoc Cuong Nguyen (NCN), Catherine J. Paul (CJP), Tage Rosenqvist (TR),
and Manuel Solano (MS).

Paper I: A convection-diffusion-reaction system with discontinuous flux modelling biofilm growth in slow sand filters

SD came up with a first version of the model and I modified it accordingly to scientific input from CJP and TR. SD and I wrote the manuscript with feedback from CJP and TR. I did the analysis in the manuscript, took further references and wrote the library for the numerical simulations.

Paper II: Simulating biofilm growth and pathogen removal in slow sand filters under variable environmental conditions using a multi-phase continuum model

I made improvements upon the previous version of the model with input from SD and included a pathogen in the submodel. I wrote the manuscript with feedback from SD, CJP, TR and SC. I performed the numerical simulations.

Paper III: An invariant-region-preserving scheme for a convection-reaction-Cahn–Hilliard multiphase model of biofilm growth in slow sand filters

JC and I performed the numerical analysis and wrote the manuscript with feedback from SD. I performed the numerical experiments.

Paper IV: A dissimilar non-matching HDG discretization for Stokes flows

MS proposed the idea and I did the theoretical analysis of the method and performed the numerical simulations. I wrote the manuscript with input from MS and NCN.

Paper V: A hybridizable discontinuous Galerkin method for Stokes/Darcy coupling on dissimilar meshes

MS and IB performed the theoretical analysis and I performed the numerical experiments.